3D ELECTRON DENSITY ESTIMATION IN THE IONOSPHERE BY USING IRI-PLAS MODEL AND GPS MEASUREMENTS

A DISSERTATION SUBMITTED TO

THE GRADUATE SCHOOL OF ENGINEERING AND SCIENCE

OF BILKENT UNIVERSITY

IN PARTIAL FULFILLMENT OF THE REQUIREMENTS FOR

THE DEGREE OF

DOCTOR OF PHILOSOPHY

IN

ELECTRICAL AND ELECTRONICS ENGINEERING

By

HAKAN TUNA

May, 2016

3D ELECTRON DENSITY ESTIMATION IN THE IONOSPHERE BY USING IRI-PLAS MODEL AND GPS MEASUREMENTS

By HAKAN TUNA

May, 2016

We certify that we have read this dissertation and that in our opinion it is fully adequate, in scope and in quality, as a dissertation for the degree of Doctor of Philosophy.

Orhan Arıkan(Advisor)

Feza Arıkan

Sinan Gezici

Ayhan Altıntaş

Cenk Toker

Approved for the Graduate School of Engineering and Science:

Levent Onural
Director of the Graduate School

ABSTRACT

3D ELECTRON DENSITY ESTIMATION IN THE IONOSPHERE BY USING IRI-PLAS MODEL AND GPS MEASUREMENTS

HAKAN TUNA

Ph.D. in Electrical and Electronics Engineering

Advisor: Orhan Arıkan

May, 2016

Three dimensional imaging of the electron density distribution in the ionosphere is a crucial task for investigating the ionospheric effects. Dual-frequency Global Positioning System (GPS) satellite signals can be used to estimate the Slant Total Electron Content (STEC) along the propagation path between a GPS satellite and ground based receiver station. However, the estimated GPS-STEC are very sparse and highly non-uniformly distributed for obtaining reliable 3D electron density distributions derived from the measurements alone. Standard tomographic reconstruction techniques are not accurate or reliable enough to represent the full complexity of variable ionosphere. On the other hand, model based electron density distributions are produced according to the general trends of the ionosphere, and these distributions do not agree with measurements, especially for geomagnetically active hours. In this thesis, a novel regional 3D electron density distribution reconstruction technique, namely IONOLAB-CIT, is proposed to assimilate GPS-STEC into physical ionospheric models. The IONOLAB-CIT is based on an iterative optimization framework that tracks the deviations from the ionospheric model in terms of F2 layer critical frequency and maximum ionization height resulting from the comparison of International Reference Ionosphere extended to Plasmasphere (IRI-Plas) model generated STEC and GPS-STEC. The IONOLAB-CIT is applied successfully for the reconstruction of electron density distributions over Turkey, during calm and disturbed hours of ionosphere using Turkish National Permanent GPS Network (TNPGN-Active). Reconstructions are also validated by predicting the STEC measurements that are left out in the reconstruction phase. The IONOLAB-CIT is compared with the real ionosonde measurements over Greece, and it is shown that the IONOLAB-CIT results are in good compliance with the ionosonde measurements. The results of the IONOLAB-CIT technique are also tracked and smoothed in time by using Kalman filtering methods for increasing the robustness of the results.

Keywords: Ionospheric tomography, GPS-STEC measurements, IRI-Plas model.

ÖZET

IRI-PLAS MODELİ VE YKS ÖLÇÜMLERİ KULLANARAK İYONKÜREDE 3 BOYUTLU ELEKTRON YOĞUNLUĞU KESTİRİMİ

HAKAN TUNA
Elektrik - Elektronik Mühendisliği, Doktora
Tez Danışmanı: Orhan Arıkan
Mayıs, 2016

İyonküredeki elektron yoğunluğu dağılımını 3 boyutlu görüntüleyebilmek iyonkürenin etkilerinin araştırılması için kritik öneme sahiptir. Yerküresel Konumlama Sistemi (YKS) uydularından iki farklı frekans bandında yayınlanan sinyaller, YKS uyduları ve yer konumlu alıcılar arasında Eğik Toplam Elektron İçeriği (ETEİ) tahmini yapmak için kullanılabilir. Ancak, elde edilen YKS-ETEİ değerleri, sadece bu ölçümler kullanılarak güvenilir bir 3 boyutlu elektron yoğunluğu dağılımı elde etmek için oldukça seyrek ve düzensizdir. İyonkürenin tomografisini çekmek için önerilen standart yöntemler iyonkürenin karmaşık ve değişken yapısını modellemekte yetersiz kalmaktadır. Diğer yandan, model tabanlı elektron yoğunluğu dağılımları, iyonküredeki genel yönsemelere göre sonuçlar üretmekte ve üretilen bu sonuçlar genellikle gerçek ölçümlerle, özelikle iyonkürenin fırtınalı olduğu günlerde, uyumlu sonuçlar vermemektedir. Bu tezde, IONOLAB-CIT adını verdiğimiz, bölgesel 3 boyutlu elektron yoğunluğu dağılımı elde etmek amacıyla YKS-ETEİ ölçümlerini ve fiziksel iyonküre modellerini kullanan bir tomografi tekniği önerilmektedir. IONOLAB-CIT, iteratif algoritmalar vasıtasıyla, IRI-Plas iyonküre modelinden hesaplanan sentetik ETEİ ölçümlerini ve gerçek YKS-ETEİ ölçümlerini karşılaştırarak, iyonküredeki F2 katmanının kritik frekansında ve maksimum elektron yoğunluğunun erişildiği yükseklik değerinde IRI-Plas iyonküre modeline göre oluşan sapmaları izlemeye çalışmaktadır. IONOLAB-CIT, Türkiye Ulusal Sabit GPS Ağı (TUSAGA-Aktif) verileri kullanılarak Türkiye üzerinde iyonkürenin sakin ve fırtınalı olduğu günlerde 3 boyutlu elektron yoğunluğu dağılımları elde etmek için başarılı bir şekilde kullanılmıştır. Elde edilen 3 boyutlu elektron yoğunluğu dağılımları kullanılarak yönteme girdi olarak verilmeyen YKS-ETEİ ölçümleri yakın hassasiyette tahmin edilebilmiştir. IONOLAB-CIT sonuçları Yunanistan üzerinde alınan gerçek iyonosonda sonuçları ile karşılaştırılmış, ve oldukça uyumlu sonuçlar

elde edildiği gösterilmiştir. Daha gürbüz sonuçlar elde edebilmek için IONOLAB-CIT sonuçları Kalman filtre yöntemleri kullanılarak zamanda takip edilip düzeltilmektedir.

Anahtar sözcükler: İyonküre tomografisi, YKS-ETEİ ölçümleri, IRI-Plas modeli.

Acknowledgement

I would like to express my gratitude to Prof. Dr. Orhan Arıkan for his supervision, suggestions and encouragement throughout the development of this thesis.

I am grateful to Prof. Dr. Feza Arıkan and Assoc. Prof. Dr. Sinan Gezici for their valuable contributions throughout my Ph.D. studies.

I am also grateful to Prof. Dr. Ayhan Altıntaş and Prof. Dr. Cenk Toker for reviewing this thesis and agreeing to be in my Ph.D. defense committee.

I would like to thank Assoc. Prof. Dr. Umut Sezen for providing very useful software tools in the development of this thesis.

I would like to thank IONOLAB research group at Hacettepe University and IGS, for providing valuable data, without which this study will not be possible.

Finally, I would like to express my deepest gratitude to my family, who brought me to this stage with their endless love and support.

The studies in this thesis are supported by TUBITAK grants 109E055, 112E568, 114E092.

Contents

List of Figures

List of Tables

Chapter 1

Introduction

1.1 Motivation

Variability in ionospheric electron density (N_e) directly effects the reliability and accuracy of both ground and space based instrumentation. With increased demands in satellite based communication and positioning systems, the number of assets that are directly under risk by the variability of space weather and its primary component N_e, are also on the rise. Computerized Ionospheric Tomography (CIT) is an effective tool to reconstruct ionospheric electron density values based on satellite measurements. Obtaining a robust and accurate 3D model of the electron density distribution in the ionosphere is a very important task for understanding ionospheric effects. A robust 3D model of the ionospheric electron density distribution also enables us to model and predict performance of the radio communication through the ionosphere reliably.

1.2 Related Work

Since the advent of satellite based instrumentation, various CIT techniques using Total Electron Content (TEC) measurements have been developed in the literature. Very first methods used TEC measurements obtained from Low Earth Orbit (LEO) satellites for 2D imaging of the ionosphere along the track of the satellites and the receiver array. Due to the fact that LEO satellites move very fast, ionosphere is considered to be quasi-static during each satellite pass. Using this assumption, a method which uses Algebraic Reconstruction Technique (ART) for obtaining a 2D image of the ionosphere by using TEC data measured between ground receivers and Naval Navigational Satellite System (NNSS) satellites, orbiting the Earth at 1,100 km altitude, has been introduced in [1]. Since then, iterative reconstruction algorithms became a widely used method in 2D computerized tomography problems discussed in various studies including but not limited to [2], [3], [4], [5]. However, these methods produce a 2D vertical slice of the electron density distribution whose location depends on the orbit of the satellites and the receiver locations.

After the advent of GPS, TEC measurements obtained from GPS receivers provided very useful information about the ionosphere. However, using GPS measurements for CIT techniques required different approaches than using LEO satellite measurements. Unlike LEO satellites, GPS satellites orbit the Earth at 20,200 km altitude, and therefore, they move very slowly with respect to the ionosphere. This property limits the angle of measurements between a GPS satellite and a receiver station within a time interval in which ionosphere can be considered as quasi-static. On the other hand, GPS system is designed to track at least four satellites at a given time and ground based receivers can continuously provide TEC measurements from a number of GPS satellites with varying slant paths.

GPS based TEC measurements for CIT reconstruction was first introduced in [6]. Since then, alternative ionospheric tomography techniques employing GPS based TEC measurements have been developed making use of increasing number of local and global GPS receiver networks. However, due to the complicated geometry of data acquisition, most of the developed tomographic reconstruction techniques have to be custom tailored to the application or to the network.

The main problem in the GPS measurements based CIT is the sparsity of the data. The problem becomes even more challenging when the goal is reconstruction of 3D electron density. The increased number of unknowns in 3D geometry complicate the solution significantly and this would render the reconstruction problem next to impossible to solve, if no prior information on the electron density distribution is introduced. Therefore, to overcome the issues of insufficient data, many methods use some kind of regularization together with a background ionosphere model such as those discussed in [7], [8]. Some CIT methods utilize basis functions for constraining the solution in a predetermined problem space as given in [9], [10]. Examples of model-free iterative approaches can be found in [11], [12]. CIT using neural networks is also proposed in the literature as given in [13]. Comprehensive reviews of general ionospheric tomography methods are provided in [14] and [15].

Since TEC measurements available for 3D ionospheric reconstruction are not dense enough, reconstruction techniques based on only TEC measurements demand new regularization techniques or declaration of some cost functions for minimization. Yet, in this case, the solution set may include physically unreliable or inaccurate results. Because of the sparsity of the measurements, the prior information about the problem has a great significance. The reconstruction methods which do not depend on any ionospheric models or take into account any physical properties of the ionosphere, produce same results for given measurement set, regardless of the location of the measurements, or time. Thus, it is of utmost importance to utilize a physically acceptable model in solution of ill-determined ionospheric tomography problems. This thesis employs IRI-Plas model which can represent the structure of both ionosphere and plasmasphere up to GPS orbital radius as a source of regularization, together with real GPS measurements.

1.3 Contributions of the Thesis

The contributions of this thesis can be grouped in three areas.

- First, a method is introduced for calculating slant TEC (STEC) values for any given receiver and satellite coordinates from IRI-Plas model, which is one of the most commonly used ionospheric models covering the plasmasphere together with the ionosphere. The results of the proposed synthetic STEC calculation method, namely IRI-Plas-STEC, are compared with real measurements obtained from GPS receivers and it is observed that IRI-Plas-STEC provides accurate estimations for calm days of the ionosphere. The developed technique is implemented as a new publicly available space weather service at `www.ionolab.org`. The studies on the IRI-Plas-STEC are published in journal papers [16] and [17].

- Second, a novel method, namely IONOLAB-CIT, is presented for obtaining robust, high resolution regional 3D electron density distribution in the ionosphere by assimilating available GPS-STEC measurements into the IRI-Plas model. IONOLAB-CIT does not use any regularization method or basis functions, but instead, it adapts the physical ionosphere parameters used in the IRI-Plas model to provide physically adaptive reconstructions that provide better agreement with the available GPS-STEC measurements. IONOLAB-CIT is applied to reconstruct regional 3D ionosphere over Turkey, using the GPS-STEC measurements obtained from Turkish National Permanent GPS Network (TNPGN-Active) for both geomagnetically calm and stormy days of the ionosphere. It is observed that the IONOLAB-CIT provides highly reliable and accurate reconstructions of 3D ionospheric electron density profiles where IRI-Plas-STEC and GPS-STEC are in good agreement even in the geomagnetic storm hours. The IONOLAB-CIT technique is published in journal paper [18].

- Third, results of the IONOLAB-CIT technique are investigated in the time domain, and a high temporal correlation in the results are observed. Based on this observation, a Kalman filtering approach is proposed for both tracking and smoothing the ionospheric disturbances in time. Tracking the IONOLAB-CIT results in time both increases the robustness of the results and decreases the computational cost of the proposed approach. The studies on the 4D IONOLAB-CIT are in preparation for publication.

1.4 Organization of the Thesis

In Chapter 2, basic background information about the ionosphere and its properties, GPS-STEC measurements and IRI-Plas model are briefly explained. In Chapter 3, a method for calculation of model-based STEC values, namely IRI-Plas-STEC, is explained, and the space weather service using the IRI-Plas-STEC method is presented. In Chapter 4, the proposed novel, regional computerized ionospheric tomography algorithm, namely IONOLAB-CIT is introduced. The performance of the IONOLAB-CIT is investigated by using synthetic and the real world examples of reconstructions for calm and stormy days of the ionosphere. In Chapter 5, the results obtained by the IONOLAB-CIT technique are investigated temporally, and a Kalman filtering based approach is proposed for obtaining more robust solutions by tracking and smoothing the results in the time domain. Chapter 6 consists of the remarks and conclusions.

Chapter 2

Remote Sensing and Modelling of the Ionosphere

2.1 The Ionosphere

The ionosphere is a layer in the atmosphere, ranging from about 60 km to 1,300 km in height from the Earth surface. It is a layer mostly ionized by solar radiation, and that is what makes it so interesting and distinguished from other layers of the atmosphere. It has a crucial importance in radio wave propagation because of its electromagnetic properties.

The most important parameter for modelling the ionosphere is the electron density profile. Ionosphere has significant effects on the radio wave propagation, depending on the electron density profile along the transmission path which creates varying refractive indices in the ionosphere. Ionosphere reflects radio waves at frequencies roughly below 30 MHz, behaving like a mirror, sending radio waves back to Earth and making global scale radio communication possible. For higher frequencies, ionosphere introduces delays on the radio waves. Ionosphere is the main error source for global navigation satellite systems like GPS. If the ionospheric effects are not compensated properly, GPS receivers can not obtain precise location information. During strong periods of solar activity, performance of GPS receivers can degrade significantly.

Ionosphere owes its existence to solar radiation. Therefore it is mainly affected by solar zenith angle and solar activity. In the daytime, ionization in the ionosphere is at its highest level, and the ionospheric effects are stronger. In the night, ionization decreases, and the effects of ionosphere get weaker. Ionization patterns in the ionosphere generally follow this 24 hour cycle, however, they also follow the Sun's rotational period which takes 27 days, and solar activity period which takes roughly 11 years. The main exceptions for these periodic patterns are the solar active days, where ionization patterns in the ionosphere can be very chaotic and reach extreme values.

In order to understand the physical structure of the ionosphere, one has to first understand the physical phenomena behind it. When a photon strikes a molecule in the air, and if the emergent energy is high enough, it can dislodge an electron from it. This process creates negatively charged free electrons and positively charged ions, and is called as ionization. If a positively charged molecule captures a free electron, it is called as recombination. Ionization process creates equal amounts of positively charged ions and negatively charged electrons, however since the mobility of electrons are much higher than the mobility of ions, density of free electrons are generally used for modelling the ionosphere. At the lower parts of the ionosphere, the atmosphere is very dense, molecules are very close to each other, and any ionization is followed by a recombination process. At higher altitudes, atmosphere gets thinner and electrons can roam free in the atmosphere longer before a recombination takes place. Therefore, electron density in the atmosphere increases as the altitude increases. However, as the altitude gets higher, atmosphere gets too thin, and the density of the molecules decrease to very low levels. Therefore, electron density starts decreasing beyond a certain altitude. The electron density profile in the ionosphere can be briefly explained by these two processes, however, in reality, electron density profile is a very complex phenomenon. It depends on large set of parameters such as the density of atmospheric gases and their interaction with different wavelengths of the sunlight. Together with the geomagnetic field effects and other secondary effects, these

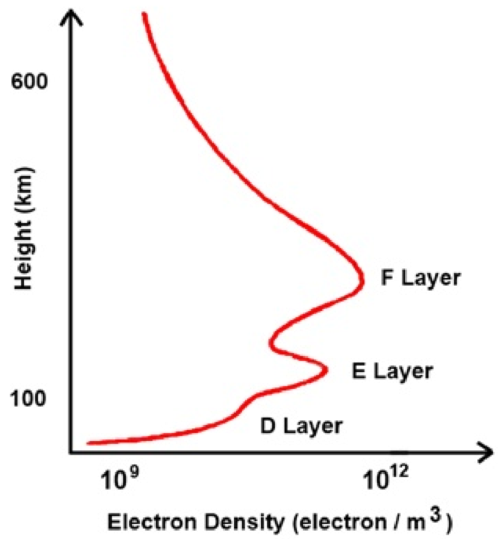

Figure 2.1: Demostration of a typical electron density profile in the ionosphere and main ionosphere layers.

properties constitute an electron density profile as shown in Figure 2.1.

Vertical electron density profile has a layered structure with smooth boundaries that are called as D, E and F layers. There are no strict ranges defined for each layer, but the general values can be given. D layer is the lowest layer of the ionosphere which extends from about 60 km to 85 km, and is present only at daytime. E layer extends from about 85 km to 140 km, and is always present during the day and the night. Finally, F layer is the outermost and the most important layer in the ionosphere, extending from about 140 km to more than 500 km. In the daytime, this layer is divided into two sub layers as F1 and F2. F2 layer is the densest electron layer in the ionosphere, i.e., ionosphere reaches its maximum electron density in this layer. The maximum value of the electron density and the height where the electron density reaches its maximum are the most important parameters for modelling the electron density profile in the ionosphere. Detailed information about the ionosphere and its effects on the radio wave propagation can be found at [19], [20], [21].

2.2 GPS-STEC Measurements

In situ measurements of electron density distribution in the ionosphere is not practical to provide enough spatial coverage even for regional 3D ionospheric imaging. Therefore, remote sensing techniques are generally used to obtain information about the electron density distribution over the region of interest. The most commonly used ionospheric measurement obtained from remote sensing techniques is Total Electron Content (TEC). TEC is the total number of free electrons in a cylinder with 1 m^2 cross section area, along a given ray path between two points. It is expressed in terms of TECU which corresponds to 10^{16} electrons/m^2. There are various techniques used for estimating TEC in the ionosphere, such as those explained in [22], [23], [24]. When TEC is calculated on a vertical path in the local zenith direction, it is called Vertical TEC (VTEC). Slant TEC (STEC) is usually used to designate the TEC on a ray path other than the local zenith direction.

Global Positioning System (GPS) is the most widely used tool for TEC estimation in the ionosphere. It is a satellite based positioning and navigation system, constructed for providing precise location information to GPS receivers anywhere on Earth [25]. GPS is comprised of multiple satellites (initially designed for 24, currently 31 operational), which are continuously monitored from the ground. Like other Global Navigational Satellite Systems (GNSS), GPS based positioning systems basically work by calculation of transmission path delays between the receiver and the satellites. For this reason, all satellites have very stable atomic clocks, which are periodically synchronized with each other. GPS satellites continuously broadcast their current position and time to Earth. Any GPS receiver with an unobstructed line-of-sight to 4 or more satellites can calculate its location and time. However, signals transmitted from GPS satellites are unavoidably disturbed by the ionosphere. Due to its highly variable structure, electron density distribution in the ionosphere causes unpredictable time delays on the GPS signals. The disturbance introduced by the spatially and temporally varying nature of ionosphere may cause significant positioning errors in satellite based positioning systems [26], [27], [28]. Without calculating the ionospheric effects, GPS receivers can not obtain precise location information. The methods used in GPS for calculating the ionospheric effects turn them into valuable tools for ionospheric monitoring.

The ionospheric time delay caused by the TEC along the transmission path for a signal at frequency f can be estimated by using the following formula:

$$\Delta t = \frac{\kappa}{cf^2} TEC \tag{2.1}$$

where κ is 40.308193 $m^{-3}s^{-2}$ and c is the speed of light. In order to compensate this error, GPS satellites transmit signals at two different carrier frequency bands at 1575.42 MHz (L1) and 1227.60 MHz (L2). GPS signals at each frequency band are delayed with different amounts based on the frequency of the transmitted signals and the TEC on the transmission path. This delay difference can be calculated in GPS receivers and by using this value, overall delay can be estimated. Since this delay is directly related with the TEC in the transmission path, TEC between the satellite and the receiver can also be estimated [29], [30]. The calculation of TEC by using dual frequency receiver data can be derived from (2.1) and is given by the following formula:

$$TEC = \frac{c}{\kappa} \frac{f_1^2 f_2^2}{f_2^2 - f_1^2} (\Delta t_1 - \Delta t_2) \tag{2.2}$$

where Δt_1 and Δt_2 are time delay measurements belonging to signals at frequencies f_1 and f_2, respectively.

GPS provides a cost-effective means for computation of GPS-STEC using dual-frequency ground based receivers [31], [32], [33], [34]. GPS-STEC is used both in correction of positioning errors due to ionospheric delays and also in ionospheric physics to capture the underlying structure of ionosphere using Computerized Ionospheric Tomography such as in [10], [35], [36], [37]. The GPS-STEC measurement model includes instrumental biases that need to be determined to increase the positioning resolution and reduce non-ionospheric components from STEC.

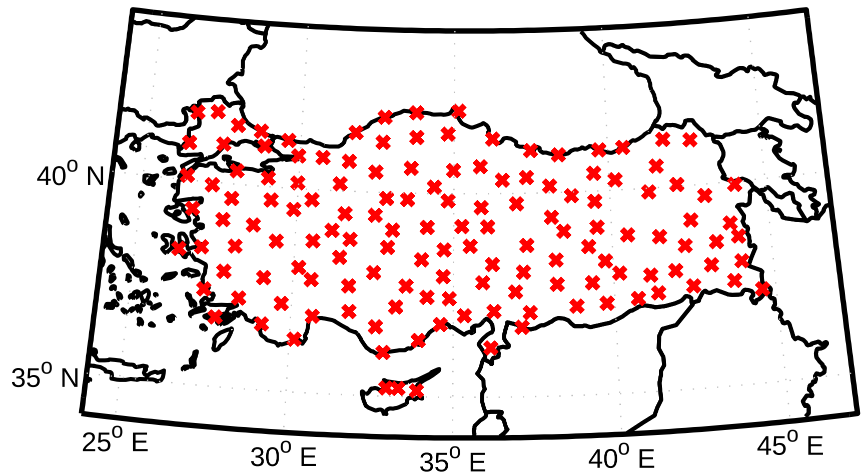

Figure 2.2: TNPGN-Active Receiver Stations.

Unfortunately, due to ambiguities and uncertainties, GPS-STEC can never be obtained in such a way to represent ionospheric and plasmaspheric part alone [31], [32], [38].

Turkish National Permanent GPS Network (TNPGN-Active) contains 146 settled GPS receiver stations spread all over Turkey and North Cyprus. These stations form a dense network, with the maximum distance between two neighbouring stations closer than 100 km. Figure 2.2 shows the geographic locations of TNPGN-Active stations. TNPGN-Active stations are continuously collecting ionospheric data and this data is processed by the IONOLAB research group at Hacettepe University for ionosphere studies.

TNPGN-Active data contains pseudo range (P) and phase delay (L) data for each frequency band (L1 and L2) and for each satellite and receiver pair. By using this data, GPS-STEC values for each receiver and satellite pair can be estimated by using IONOLAB-STEC method including differential receiver bias as IONOLAB-BIAS as discussed in detail in various publications including [34], [38], [39]. The computation of IONOLAB-TEC is also provided as a space weather service at [40] and the details are provided in [41].

The continuous measurements obtained from TNPGN-Active receivers give us a very good opportunity to investigate the electron content in the ionosphere.

However, obtaining a 3D model of the electron density in the ionosphere from GPS-STEC measurements is not straightforward. The measurement data is not uniform and the number of measurements is not sufficient for commonly used tomographic reconstruction techniques. To provide reliable reconstructions over the sparse data available, a physical/empirical model of the electron distribution has to be utilized. Moreover, to decrease the effect of measurement errors caused by individual receiver and satellite pairs, GPS-STEC measurements have to be handled together considering both the temporal and spatial correlation properties of the ionosphere. For this purpose, IRI-Plas model that will be introduced next is used in this thesis.

2.3 IRI-Plas Model

International Reference Ionosphere (IRI) is a physical and empirical model of the ionosphere, constructed by using the physical properties of the ionosphere and a vast of data acquired during multiple measurement campaigns [42]. It is sponsored by the Committee on Space Research (COSPAR) and the International Union of Radio Science (URSI). The development of the IRI model is started at late sixties, and it has been continuously developed for nearly 50 years. IRI model is updated every year by IRI Working Group during special IRI Workshops. For any given location and time, IRI model can give the monthly medians of vertical electron density profile, electron temperature, ion temperature, and ion composition estimates in the ionosphere, for an altitude range of about 60 km to about 2,000 km.

International Reference Ionosphere extended to Plasmasphere (IRI-Plas) is an extended version of the IRI that enables assimilation of TEC, sun spot number, F2 layer critical frequency and maximum ionization height in computation of electron density up to the GPS orbital height of 20,000 km [43], [44]. It has an updated scale parameter set for scaling electron density profile in the topside ionosphere and the plasmasphere [45]. Since the GPS satellites are orbiting the Earth at about 20,200 km altitude, TEC calculations obtained by using the IRI-Plas model

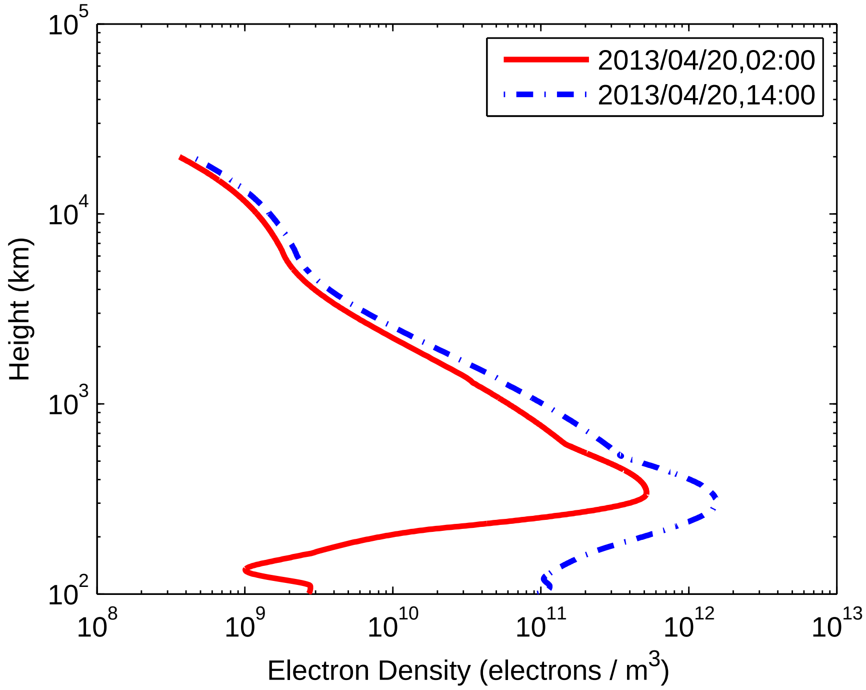

Figure 2.3: Electron density profiles obtained from IRI-Plas model for 40°N, 30°E, on 20 April 2013, at 02:00 and 14:00 GMT.

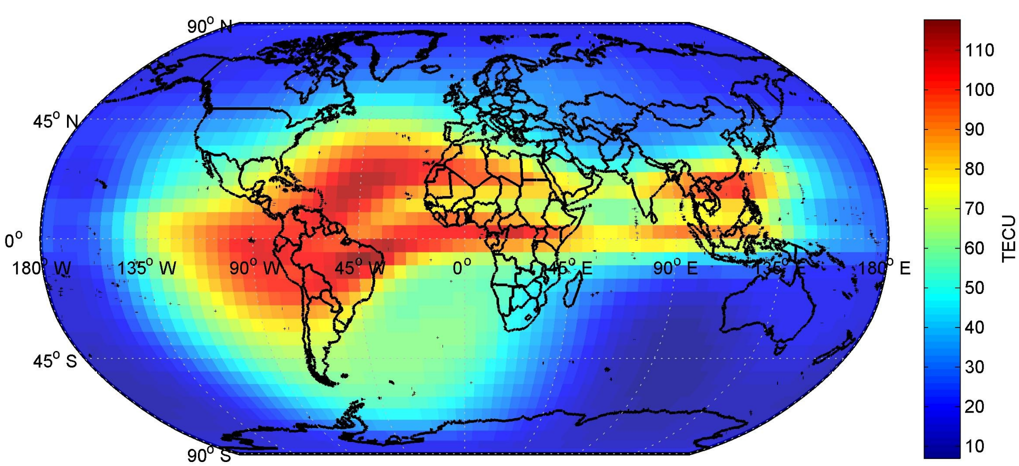

Figure 2.4: VTEC map obtained by utilizing IRI-Plas model for discrete locations in the world for 20 April 2013, 16:30 GMT.

generate closer results to the TEC measurements obtained from GPS stations [46], [47]. IRI-Plas is distributed as FORTRAN routines, model coefficients and indices files. IRI-Plas is recently designated as the international standard model for the ionosphere and the plasmasphere [43]. Figure 2.3 shows a set of sample vertical electron density profiles obtained from IRI-Plas model for 40° N, 30° E, on 20 April 2013, at 02:00 and 14:00 GMT. Figure 2.4 shows a sample global TEC map obtained by using IRI-Plas model for 20 April 2013, 16:30 GMT.

Chapter 3

Slant Total Electron Content Computation from IRI-Plas: IRI-Plas-STEC

3.1 Introduction

GPS-STEC is a widely used measurement in space weather studies for investigation of ionospheric variability. Accuracy of an ionosphere model can be investigated by comparing available GPS-STEC measurements with the numerically computed line-integrals over the model based ionosphere. In this chapter, a very accurate STEC computation technique over a model ionosphere will be introduced. As will be detailed in Chapter 4, this technique also enables us to provide robust model based reconstructions of the ionosphere.

There are approaches proposed in the literature for the calculation of STEC over an ionosphere model. Generally, thin shell approximation is adopted and STEC values are related to the VTEC values with an obliquity factor [48], [49], [50]. Although they are numerically easy to compute, thin shell approximations do not provide accurate results. In order to take into account the variation of electron density along the ray path, line integration methods are generally used such as in [51], [52]. In [51], the electron density profile along the slant path is obtained from International Reference Ionosphere (IRI) and Chapman models with 20 km segments, and integrated electron density values are computed in between 50 km to 2,000 km. In [52], a method for fast computation of STEC values is introduced where the electron density values are obtained from the NeQuick2 model, which is an updated version of the NeQuick ionosphere model [53]. The numerical STEC computation based on the NeQuick2 is provided as an online tool available at `http://t-ict4d.ictp.it/nequick2/nequick-2-web-model`. The major drawback of the IRI and the NeQuick electron density profiles is the modelling of the topside ionosphere and the plasmasphere [54].

In this thesis, a new online user-friendly STEC calculation tool by using the IRI-Plas model, namely the IRI-Plas-STEC, is introduced. This unique service utilizes the IRI-Plas model and line integration method for the STEC calculation, and presents a web based service with comprehensive features. Since the IRI-Plas is developed by modifying the IRI model in order to overcome the modelling difficulties of electron density in the plasmasphere, it is expected to produce closer results to real GPS measurements. In the proposed approach, the ionosphere and the plasmasphere are divided into vertical layers by using preset altitude step sizes. Smaller altitude step sizes are used for higher electron density regions, and larger altitude step sizes are used for lower electron density regions. The altitude values extend from 100 km to 20,000 km, which covers both the plasmasphere and the ionosphere. For a given slant path, the spherical coordinates of the points where the slant path reaches the mean altitude of these layers and the length of the slant path within the corresponding layers are calculated. The electron density values at the calculated locations on the propagation path are obtained from the IRI-Plas model for the default climatic ionospheric parameters, which would provide us the climatic component of the STEC. Electron content contribution at each layer can be closely approximated by multiplying the electron density values and the length of the propagation path within the corresponding layer. Finally, the STEC values are calculated as the total of these individual electron content contributions. By changing the input parameters and repeating the same procedure, variation of the STEC with respect to the time, the satellite elevation angle and the satellite azimuth angle can be generated.

In IRI-Plas-STEC web service, the electron density values along the chosen ray path can be obtained for a desired location, date, hour, elevation and azimuth angle. The computed STEC value is provided in TECU. The electron density profile values along the ray path are also given in a text file displayed on the screen. The variation of STEC with respect to the time of the day, the satellite elevation angle and the satellite azimuth angle can also be observed for a desired location and date. Since these options require multiple STEC calculations, the computation time increases. Therefore, when the computation is complete, computed results are sent to the user via an email as an attachment containing both the computed STEC values and its graphical representation. In order to facilitate the comparison of model based IRI-Plas-STEC with measurement based GPS-STEC values, the desired location can be chosen from International GNSS Service (IGS) stations [55] or EUREF Permanent Network stations [56] by entering the 4-digit GPS station codes or by selecting from the provided IGS station map. Also to define the upper end of the STEC ray path, any desired GPS satellite can be chosen online through the PRN identification numbers. For the chosen GPS satellite, either an STEC value for the given hour is computed or the value of STEC on the satellite path is computed for the given day and provided in a plot. These unique computational capabilities enable users from various disciplines to observe model based variability of the STEC in time, elevation, and azimuth.

This thesis also provides comparison of results obtained by proposed IRI-Plas-STEC technique with IONOLAB-STEC data. It is observed that IRI-Plas-STEC is in very good agreement with IONOLAB-STEC data obtained from TNPGN-Active stations for the calm days of ionosphere. For the stormy days, the difference between IRI-Plas-STEC and IONOLAB-STEC increases significantly. Also, on stormy days, measurement-based STEC values suffer from discontinuities and disruptions [57], [58]. The performance of the IRI-Plas-STEC for days with ionospheric disturbance is investigated in [17].

The outline of this chapter is as follows. In Section 3.2, Single Layer Ionosphere Model (SLIM) is described. In Section 3.3, the IRI-Plas-STEC method is explained in detail. In Section 3.4, comparisons of the STEC values generated by using the SLIM method and the IRI-Plas-STEC are presented. In Section 3.5, the online web service utilizing the IRI-Plas-STEC is presented. Finally, in Section 3.6, a summary of conclusions are given.

3.2 Single Layer Ionosphere Model

Single Layer Ionosphere Model (SLIM), also known as the thin shell model, assumes that the electron density profile with respect to height is concentrated in a thin shell layer which is located at a known height. The point where a given slant path s intersects this thin shell layer is called as Ionospheric Pierce Point (IPP). In the thin shell model [48], the STEC is calculated as:

$$T_s = V_s F_s, \tag{3.1}$$

where T_s is the predicted STEC along the slant path s, V_s is the VTEC at the ionospheric pierce point for slant path s, and F_s is the mapping function between the VTEC and the STEC values, given as:

$$F_s = \left[1 - \left(\frac{Rcos(\alpha^s)}{(R+h)}\right)^2\right]^{(-1/2)}, \tag{3.2}$$

where α^s is the elevation angle of the slant path s at receiver location, R is the radius of the Earth, and h is the height of the ionospheric pierce point. Here h is a variable that can change for different ionospheric conditions and regions. Validity of the estimated STEC depends on the accurate choice of h. In the literature, h is selected in a wide range which is between 300 km [31] and 450 km [49]. Use of adaptive shell heights are also discussed in the literature [31], [50].

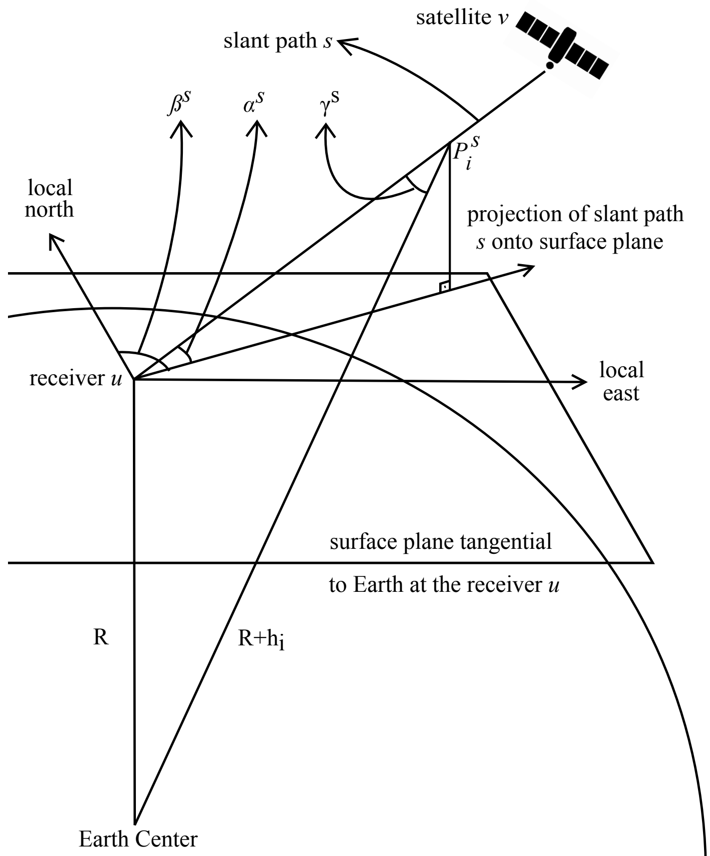

Figure 3.1: Slant path geometry and STEC calculation parameters.

The SLIM does not require a model for the 3D electron density distribution in the ionosphere. A 2D VTEC map of the region of interest is sufficient to calculate any STEC value by using (3.1) and (3.2). However, in addition to the sensitive dependency on h, the SLIM ignores the anisotropic nature of the ionosphere.

3.3 STEC calculation by using IRI-Plas Model

In this section, the mathematical details of the STEC computation by using the IRI-Plas model are provided. The geometry of the STEC computation is shown in Figure 3.1. IRI-Plas model can be used to generate electron density profile along the slant path s for the STEC computation.

A slant path s can be uniquely defined for a given receiver u and satellite v position. To approximate the required integration in the STEC computation between u and v, a Riemann sum approximation on the electron density samples along the slant path s can be computed. In the following calculations, the height of the samples along s are represented as h_i, and coordinates as P_i^s. The Earth is considered as a sphere with a radius of 6,378 km, which will be denoted as R. All angles used in trigonometric calculations, and spherical latitude and longitude values are expressed in degrees.

For the required STEC computation, let the spherical latitude of receiver u be $\phi(u)$, the spherical longitude of receiver u be $\lambda(u)$, the height of receiver u above the surface of the Earth be $h(u)$, the satellite elevation angle be α^s, and the satellite azimuth angle be β^s. Alternatively, if the Earth Centered Earth Fixed (ECEF) coordinates of receiver u and satellite v are given, these values can be transformed to the spherical coordinates and satellite angles by using the following equations:

$$\alpha^s = \sin^{-1}\left(\frac{\vec{v}-\vec{u}}{\|\vec{v}-\vec{u}\|}\cdot\frac{\vec{u}}{\|\vec{u}\|}\right), \tag{3.3}$$

$$\phi(u) = \tan^{-1}\left(\frac{u_z}{\sqrt{u_x^2+u_y^2}}\right), \tag{3.4}$$

$$\lambda(u) = \tan^{-1}\left(\frac{u_y}{u_x}\right), \tag{3.5}$$

$$h(u) = \sqrt{u_x^2+u_y^2+u_z^2} - R, \tag{3.6}$$

$$\beta^s = \tan^{-1}\left(\frac{v_e}{v_n}\right). \tag{3.7}$$

u_x, u_y and u_z represent the x, y, z coordinates of the receiver u in ECEF coordinate system. $\vec{u}$ and $\vec{v}$ are the vectors obtained by using the ECEF coordinates of receiver u and satellite v, respectively. v_e, v_n and v_u are the coordinates of satellite v in local East, North, Up (ENU) coordinate system, and can be calculated as follows:

$$\begin{bmatrix} v_e \\ v_n \\ v_u \end{bmatrix} = \begin{bmatrix} -\sin(\lambda(u)) & \cos(\lambda(u)) & 0 \\ -\sin(\phi(u))\cos(\lambda(u)) & -\sin(\phi(u))\sin(\lambda(u)) & \cos(\phi(u)) \\ \cos(\phi(u))\cos(\lambda(u)) & \cos(\phi(u))\sin(\lambda(u)) & \sin(\phi(u)) \end{bmatrix} (\vec{v} - \vec{u}), \tag{3.8}$$

In Figure 3.1, γ_i^s, the angle between the slant path s and the local zenith vector at point P_i^s, and D_i^s, the distance between the receiver u and the point P_i^s, can be calculated as follows:

$$\gamma_i^s = \sin^{-1}\left(\frac{R}{R+h_i}\sin(90+\alpha^s)\right), \tag{3.9}$$

$$D_i^s = \sqrt{R^2 + (R+h_i)^2 - 2R(R+h_i)\cos(90-\alpha^s-\gamma_i^s)}. \tag{3.10}$$

Then, the local ENU coordinates of the point P_i^s can be calculated as:

$$\begin{bmatrix} P_{i,e}^s \\ P_{i,n}^s \\ P_{i,u}^s \end{bmatrix} = \begin{bmatrix} D_i^s\cos(\alpha^s)\cos(90-\beta^s) \\ D_i^s\cos(\alpha^s)\sin(90-\beta^s) \\ D_i^s\sin(\alpha^s) \end{bmatrix}, \tag{3.11}$$

where $P_{i,e}^s$, $P_{i,n}^s$ and $P_{i,u}^s$ represent the local ENU coordinates of point P_i^s, respectively. These ENU coordinates are transformed to ECEF coordinates as:

$$\mathbf{T}^u = \begin{bmatrix} -\sin(\lambda(u)) & \sin(\phi(u))\cos(\lambda(u)) & \cos(\phi(u))\cos(\lambda(u)) \\ -\cos(\lambda(u)) & \sin(\phi(u))\sin(\lambda(u)) & \cos(\phi(u))\sin(\lambda(u)) \\ 0 & \cos(\phi(u)) & \sin(\phi(u)) \end{bmatrix}, \tag{3.12}$$

$$\begin{bmatrix} u_x \\ u_y \\ u_z \end{bmatrix} = \begin{bmatrix} R\cos(\phi(u))\cos(\lambda(u)) \\ R\cos(\phi(u))\sin(\lambda(u)) \\ R\sin(\phi(u)) \end{bmatrix}, \tag{3.13}$$

$$\begin{bmatrix} P^s_{i,x} \\ P^s_{i,y} \\ P^s_{i,z} \end{bmatrix} = \mathbf{T}^u \begin{bmatrix} P^s_{i,e} \\ P^s_{i,n} \\ P^s_{i,u} \end{bmatrix} + \begin{bmatrix} u_x \\ u_y \\ u_z \end{bmatrix}. \tag{3.14}$$

In equations (3.12), (3.13) and (3.14), $\mathbf{T}^u$ represents the transformation matrix; $P^s_{i,x}$, $P^s_{i,y}$ and $P^s_{i,z}$ represent the x, y, z coordinates of the point P^s_i, respectively, in the ECEF coordinate system.

After the ECEF coordinates of P^s_i are obtained, the spherical latitude of P^s_i, denoted as $\phi(P^s_i)$, and the spherical longitude of P^s_i, denoted as $\lambda(P^s_i)$, which will be used as inputs to the IRI-Plas, are calculated as follows:

$$\phi(P^s_i) = \tan^{-1}\left(\frac{P^s_{i,z}}{\sqrt{(P^s_{i,x})^2 + (P^s_{i,y})^2}}\right), \tag{3.15}$$

$$\lambda(P^s_i) = \tan^{-1}\left(\frac{P^s_{i,y}}{P^s_{i,x}}\right). \tag{3.16}$$

Note that, for unambiguous determination of $\phi(P^s_i)$ and $\lambda(P^s_i)$, the inverse tangent functions shall be used together with the quadrant information.

In order to find the electron density contribution at a sequence of heights, the length of the slant path s within the height step Δh_i, which will be denoted as ΔH^s_i, should be calculated. For this purpose, the following trigonometric relation can be used:

$$\Delta H^s_i = \frac{\Delta h_i}{\cos(\gamma^s_i)}. \tag{3.17}$$

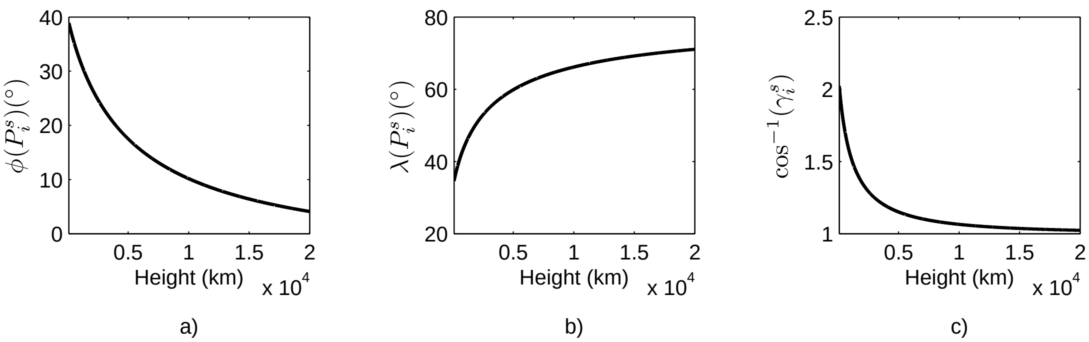

Figure 3.2: Variation of STEC calculation parameters with respect to elevation. a) $\phi(P_i^s)$, b) $\lambda(P_i^s)$, and c) $\cos^{-1}(\gamma_i^s)$ with respect to elevation, for input parameters $\phi(u) = 39.92^\circ$, $\lambda(u) = 32.85^\circ$, $\alpha^s = 28^\circ$ and $\beta^s = 126^\circ$.

Finally, IRI-Plas model based STEC value along the slant path s can be approximated by integrating the electron density contributions from each height along the slant path s as non-uniform Riemann sum:

$$T_s = \sum_{i=1}^{I} Ne(\phi(P_i^s), \lambda(P_i^s), h_i)\Delta H_i^s, \tag{3.18}$$

where $Ne(\phi(P_i^s), \lambda(P_i^s), h_i)$ represents the electron density value obtained from IRI-Plas model for given latitude $\phi(P_i^s)$, longitude $\lambda(P_i^s)$ and height h_i, and I is the length of $\mathbf{h}$, the vector of heights h_i. For illustrative purposes, Figure 3.2 shows the $\phi(P_i^s)$, $\lambda(P_i^s)$ and $\cos^{-1}(\gamma_i^s)$ dependence to the height, respectively, for a sample STEC calculation for the set of input parameters $\phi(u) = 39.92^\circ$, $\lambda(u) = 32.85^\circ$, $\alpha^s = 28^\circ$ and $\beta^s = 126^\circ$.

In choosing the samples in $\mathbf{h}$, the trade off between the accuracy and efficiency of the computation is considered. A longer vector $\mathbf{h}$ with denser height levels will yield more precise results while increasing the computational time. A non-uniform separation of layers with denser height levels at higher electron density regions, and sparse height levels at lower electron density regions provides better approximations for the desired line integral.

In order to investigate the proper selection of **h**, 1000 different vertical electron density distribution functions are generated by using IRI-Plas, at randomly selected positions on Earth and for randomly selected dates between 1 January 2003 and 1 January 2013, and for random hours of the day. Figure 3.3a shows the mean value of the obtained electron density distributions, and Figure 3.3b shows the mean value of the absolute values of the first order derivatives of the obtained electron density distributions, with respect to height. The regions with higher first order derivative require denser allocation of the layers. The maximum value of the first order derivative is reached at the height of 234 km. At a height of 600 km, this value drops well below 10 percent of the maximum value. At 1,300 km height and above, IRI-Plas model employs plasmasphere equations, and the first order derivative drops well below 1 percent of the its maximum value. Consequently, use of 1 km height step sizes between 100 and 600 km, 10 km step sizes between 600 and 1,300 km, and 50 km step sizes between 1,300 and 20,000 km, has been found to provide acceptable computational results.

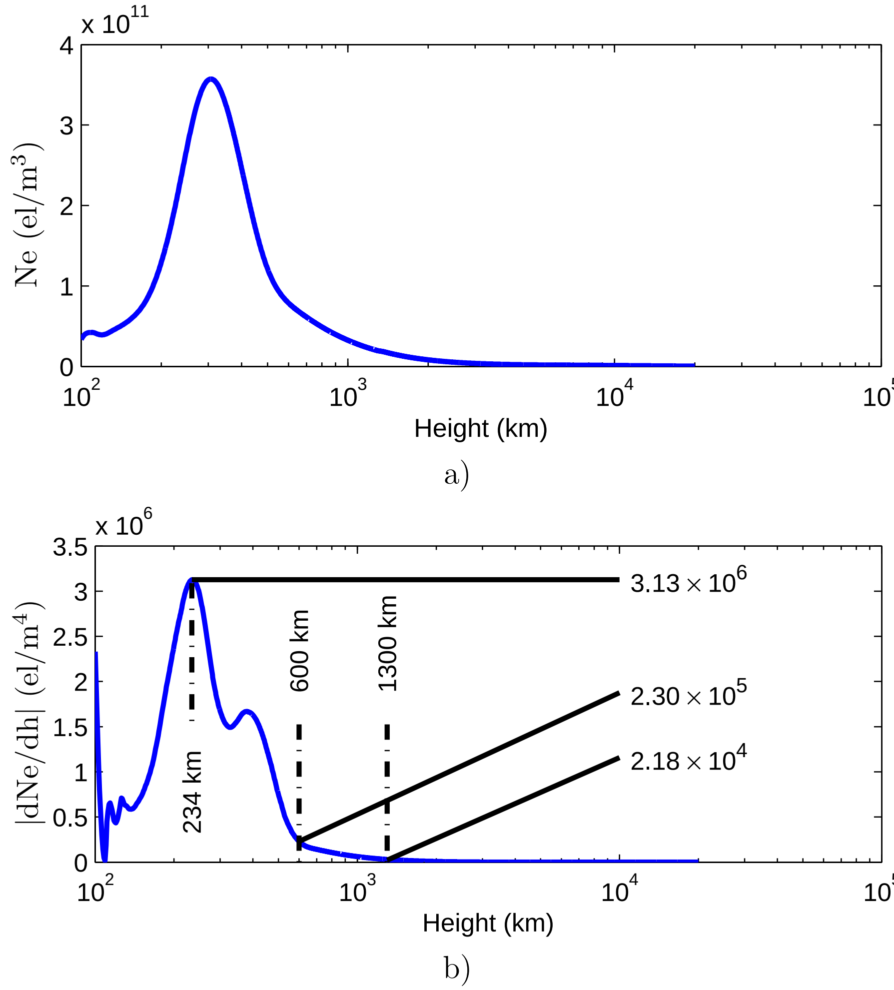

Figure 3.3: a) Mean value of 1,000 randomly generated vertical electron density profiles from IRI-Plas, for randomly selected positions on Earth, for randomly selected dates between 1 January 2003 and 1 January 2013, and for random hours. b) Mean value of the absolute values of the first order derivatives of 1,000 randomly generated vertical electron density profiles used in a), with respect to height.

3.3.1 STEC with Respect to the Hour of the Day

By using the proposed methodology, real STEC measurements obtained from GPS systems can be directly compared with the IRI-Plas model based STEC estimates. For this purpose, IONOLAB-STEC data is used as experimental GPS measurement [39]. Figures 3.4, 3.5 and 3.6 show comparison of IRI-Plas-STEC and IONOLAB-STEC with respect to hour. Two different days are selected for calculations: 12 March 2010, which is a calm day, and 13 April 2012, which is a geomagnetically disturbed day. IONOLAB-STEC and IRI-Plas-STEC values are computed for three different GPS receiver stations located at equatorial, mid and high latitude regions. The equatorial station *ntus* [1.3° N, 103.6° E] is located in Singapore, Republic of Singapore, the mid latitude station *ankr* [39.7° N, 32.7° E] is located in Ankara, Turkey, and the high latitude station *kir0* [67.7° N, 21.0° E] is located in Kiruna, Sweden. Satellite ephemerides data is extracted from the IONOLAB-STEC data obtained for three stations on selected days. For each station, a satellite that passes close to the local zenith angle is chosen. These satellites are identified as PRN 16 for *ntus*, PRN 7 for *ankr* and PRN 20 for *kir0*. Figures 3.4, 3.5 and 3.6 indicate that the computations of STEC from IRI-Plas and IONOLAB-STEC are in agreement with each other for a calm day, yet they may differ significantly on a geomagnetically disturbed day. This is mainly due to the fact that IRI-Plas Ne profiles are based on the CCIR monthly median coefficients.

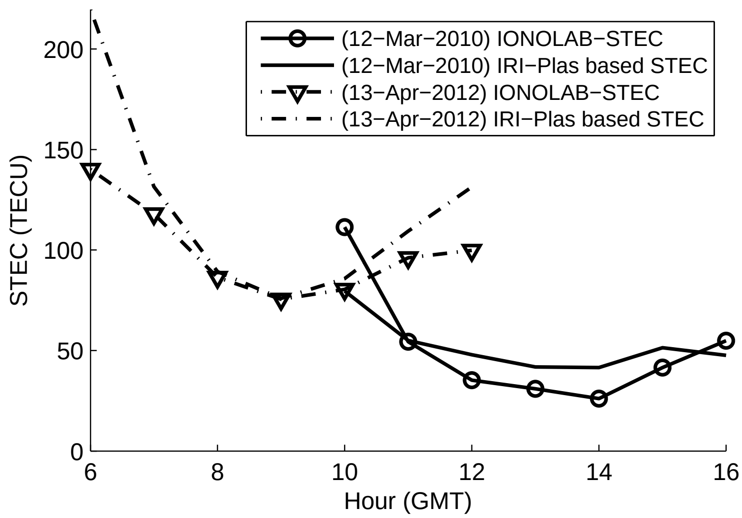

a)

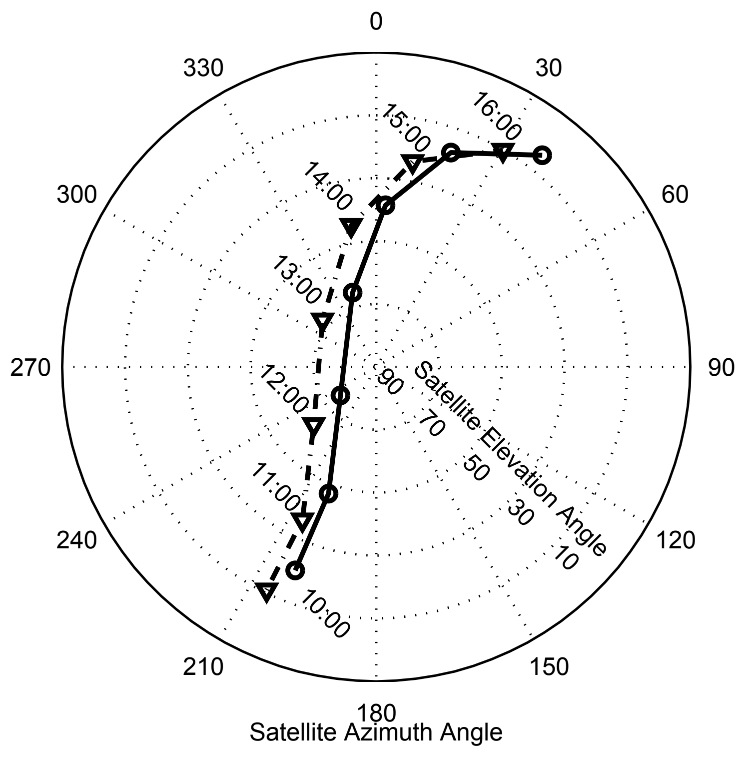

b)

Figure 3.4: a) Comparison of IRI-Plas-STEC and IONOLAB-STEC values with respect to hour for 12 March 2010 (calm day) and 13 April 2012 (disturbed day) between the GPS receiver station *ntus* and the GPS satellite with PRN identifier 16. b) Satellite tracks in local polar coordinate system for the GPS receiver station *ntus* and the GPS satellite with PRN identifier 16.

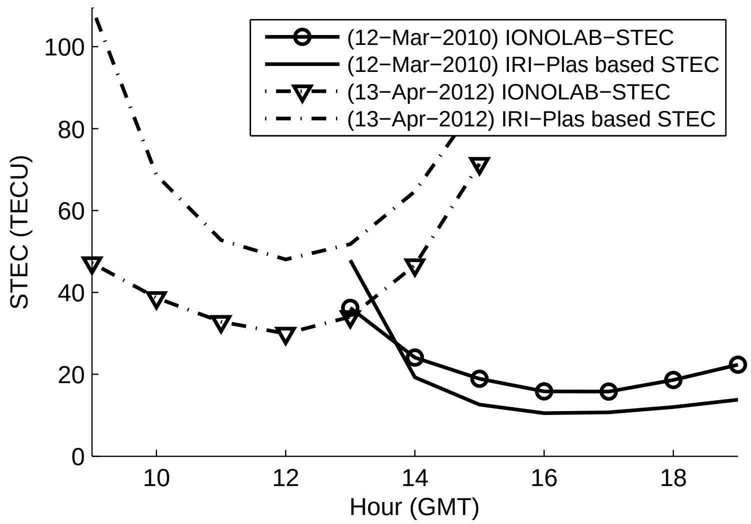

a)

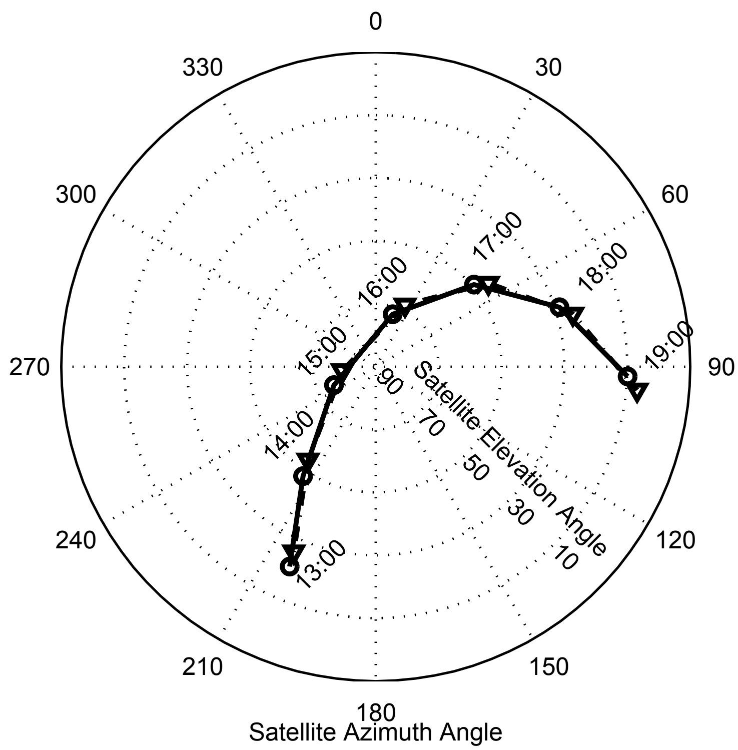

b)

Figure 3.5: a) Comparison of IRI-Plas-STEC and IONOLAB-STEC values with respect to hour for 12 March 2010 (calm day) and 13 April 2012 (disturbed day) between the GPS receiver station *anrk* and the GPS satellite with PRN identifier 7. b) Satellite tracks in local polar coordinate system for the GPS receiver station *anrk* and the GPS satellite with PRN identifier 7.

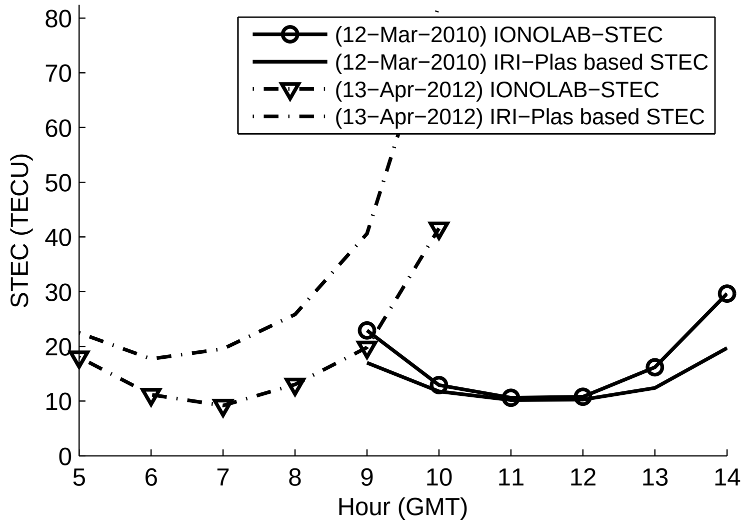

a)

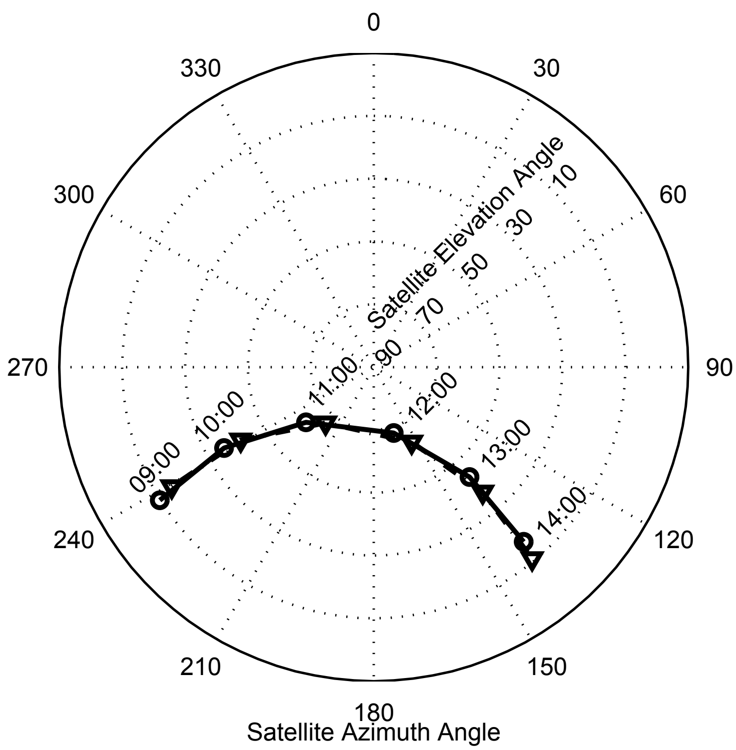

b)

Figure 3.6: a) Comparison of IRI-Plas-STEC and IONOLAB-STEC values with respect to hour for 12 March 2010 (calm day) and 13 April 2012 (disturbed day) between the GPS receiver station *kir0* and the GPS satellite with PRN identifier 20. b) Satellite tracks in local polar coordinate system for the GPS receiver station *kir0* and the GPS satellite with PRN identifier 20.

3.3.2 Effect of the Satellite Elevation Angle on STEC

In order to see the effect of satellite elevation angle in the STEC estimation, STEC values are calculated for synthetic satellite positions which have constant satellite azimuth angles and a range of satellite elevation angles in the interval [10° 90°] with a step size of 10°. Figure 3.7 shows the STEC values obtained on 22 April 2009, at 12:00 GMT, for a receiver station located at coordinates [39° N, 35° E]. Four different satellite azimuth angles are used in the calculations, 0° (North), 90° (East), 180° (South) and 270° (West). Note that, the computed STEC values converge to the same vertical TEC value as the satellite elevation angle increases. As the satellite elevation decrease, STEC estimates show variation based on the electron density distribution at the corresponding azimuth directions. Figure 3.7 indicates higher electron density values in the South, and lower electron density values in the North. Typically, in GPS measurements, ionosphere is considered to be uniform and homogeneus for satellite elevation angles greater than 60°. Calculating STEC values by sweeping a range of satellite elevation angles provides a means to investigate the validity of this commonly used assumption.

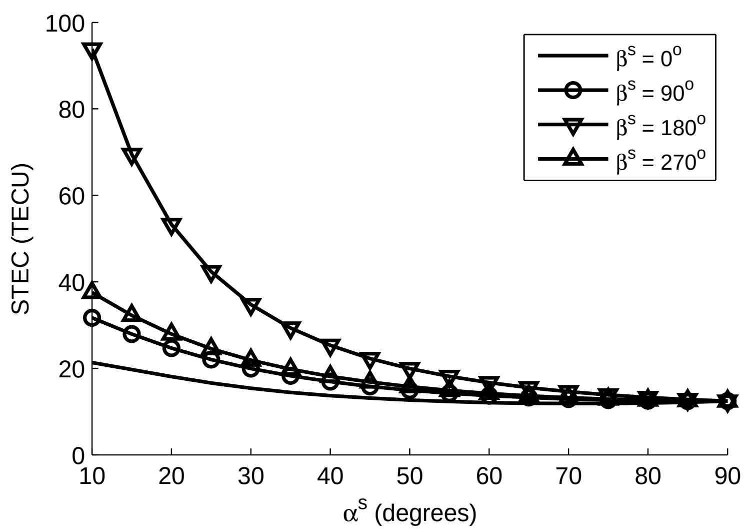

Figure 3.7: IRI-Plas-STEC calculations with respect to satellite elevation angle, on 22 April 2009, at 12:00 GMT, for a receiver station located at coordinates [39° N, 35° E], and for a GPS satellite position located at North, East, South and West of the receiver station.

3.3.3 Effect of the Satellite Azimuth Angle on STEC

Investigation of STEC with respect to the satellite azimuth angle provide characteristics of anisotropy in the ionosphere. For this purpose, STEC values can be calculated for synthetic satellite positions which have constant satellite elevation angles and a range of satellite azimuth angles in the interval [0° 350°] with a step size of 10°. Figure 3.8 shows the computed STEC values obtained on 22 April 2009, at 12:00 GMT, for a receiver station located at coordinates [39° N, 35° E]. Three different satellite elevation angles are used in calculations, 40°, 60° and 80°. The calculated STEC is minimum for the azimuth angle of 10°, and maximum for the azimuth angle of -170°, which indicates an increase in the electron density towards the South. Figure 3.8 also indicates the effect of the satellite elevation angle on the STEC measurements. As the satellite elevation angle decreases, the effect of the satellite azimuth angle on the STEC measurements gets stronger. This functionality also demonstrates the validity of the azimuthal homogeneity assumptions with respect to the satellite elevation angles.

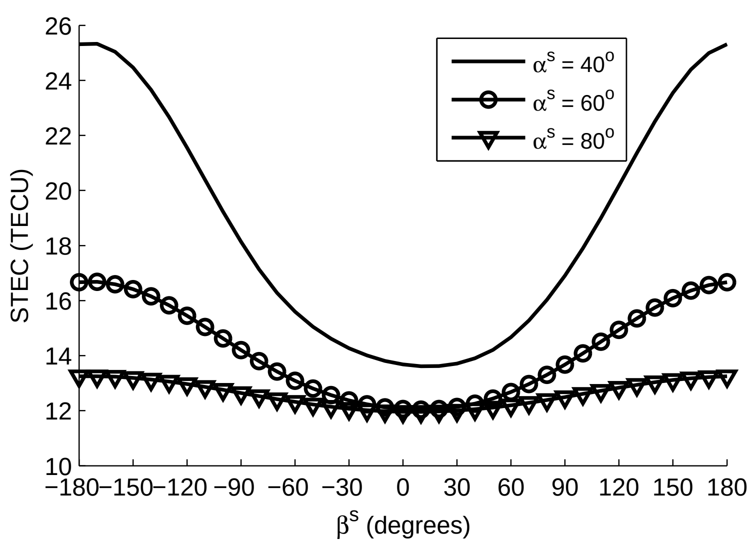

Figure 3.8: IRI-Plas-STEC calculations with respect to satellite azimuth angle, on 22 April 2009, at 12:00 GMT, for a receiver station located at coordinates [39° N, 35° E], and for satellite elevation angles of 40°, 60° and 80°.

3.4 Comparison with the SLIM

The comparison of the IRI-Plas-STEC with the SLIM STEC calculation method is done in two parts. In the first part, the height of the thin shell is selected as 428.8 km which is used in [32] and recommended as the best fit to Chapman profile in the least squares sense. In the second part, the thin shell height is selected adaptively. The general approach for selecting an adaptive shell height is to find the height where the ionospheric electron density reaches its maximum. Before calculating the corresponding STEC, the height of the electron density peak is calculated at the receiver location, and the thin shell layer is assumed to lay on the calculated height. IRI-Plas model is used as the ionosphere model for both methods. Figure 3.9a shows comparison of IRI-Plas-STEC with the STEC values computed by the SLIM method on 15 February 2012, for the receiver station located at [45° N, 15° E], for 46° satellite elevation angle, and 210° satellite azimuth angle. Results show that the maximum difference between the IRI-Plas-STEC and the STEC value computed by the SLIM method may reach 1.5 TECU depending on the hour of the day. Figure 3.9b shows comparison of the IRI-Plas-STEC with the STEC values computed by the SLIM method on 15 August 2012, for the receiver station located at [40° N, 35° E], for 32° satellite elevation angle, and 15° satellite azimuth angle. Results show that the maximum difference between the IRI-Plas-STEC and the STEC value computed by the SLIM method may reach 5 TECU depending on the hour of the day. As expected, the difference between the IRI-Plas-STEC and the STEC values computed by the SLIM method increases significantly when the satellite elevation angle is lower. Figure 3.10 shows the effective STEC / VTEC ratio for two methods. While this ratio is a constant value in the SLIM method, it changes as the altitude rises in the IRI-Plas-STEC method.

SLIM assumes that the two measurements with the same ionospheric pierce points and the same satellite elevation angles, no matter how the receiver and the satellite are located, will give exactly the same results. In order to examine the validity of this assumption, another experiment is done for four different receiver locations, for the same satellite elevation angles of 30°, and for different satellite azimuth angles, such that all the slant paths intercept at the same ionospheric pierce point located at the height of 428.8 km. The coordinates of the receivers and the satellite angles are chosen as:

- [29.66° N, 40.83° E], $\alpha^s = 30$, $\beta^s = 0°$
- [41.19° N, 40.83° E], $\alpha^s = 30$, $\beta^s = 180°$
- [35.63° N, 33.75° E], $\alpha^s = 30$, $\beta^s = 90°$
- [35.63° N, 47.91° E], $\alpha^s = 30$, $\beta^s = 270°$

The ionospheric pierce points for all the slant paths are calculated as [35.42° N, 40.83° E]. Figure 3.11 shows calculated STEC values for the slant paths on 30 June 2012 by using the IRI-Plas-STEC method. There is nearly 3 TECU difference between the respective STEC values when the electron content in the ionosphere reaches its maximum. Results indicate that the SLIM method ignores the anisotropic nature of the ionosphere and does not produce accurate results. On the other hand, IRI-Plas-STEC produces more accurate results by integrating the electron density values along the receiver-satellite path.

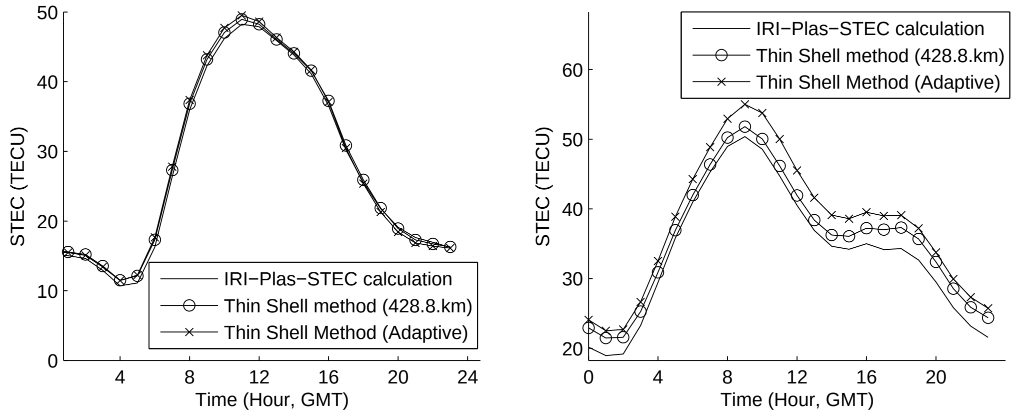

a) b)

Figure 3.9: STEC values calculated by the IRI-Plas-STEC and SLIM method for thin shell height value of 428.8 km and adaptively chosen thin shell height value, for a) the receiver located at [45° N, 15° E], on 15 February 2012, α^s = 46°, β^s = 210°, b) the receiver located at [40° N, 35° E], on 15 August 2012, α^s = 32°, β^s = 15°.

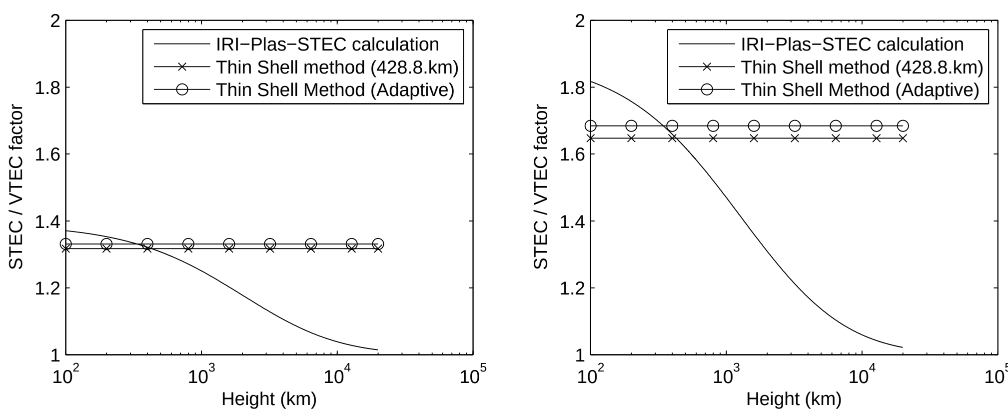

a) b)

Figure 3.10: Effective STEC / VTEC ratios calculated by the IRI-Plas-STEC and SLIM method for thin shell height value of 428.8 km and adaptively chosen thin shell height value, with respect to height, for a) the receiver located at [45° N, 15° E], on 15 February 2012, α^s = 46°, β^s = 210°, b) the receiver located at [40° N, 35° E], on 15 August 2012, α^s = 32°, β^s = 15°.

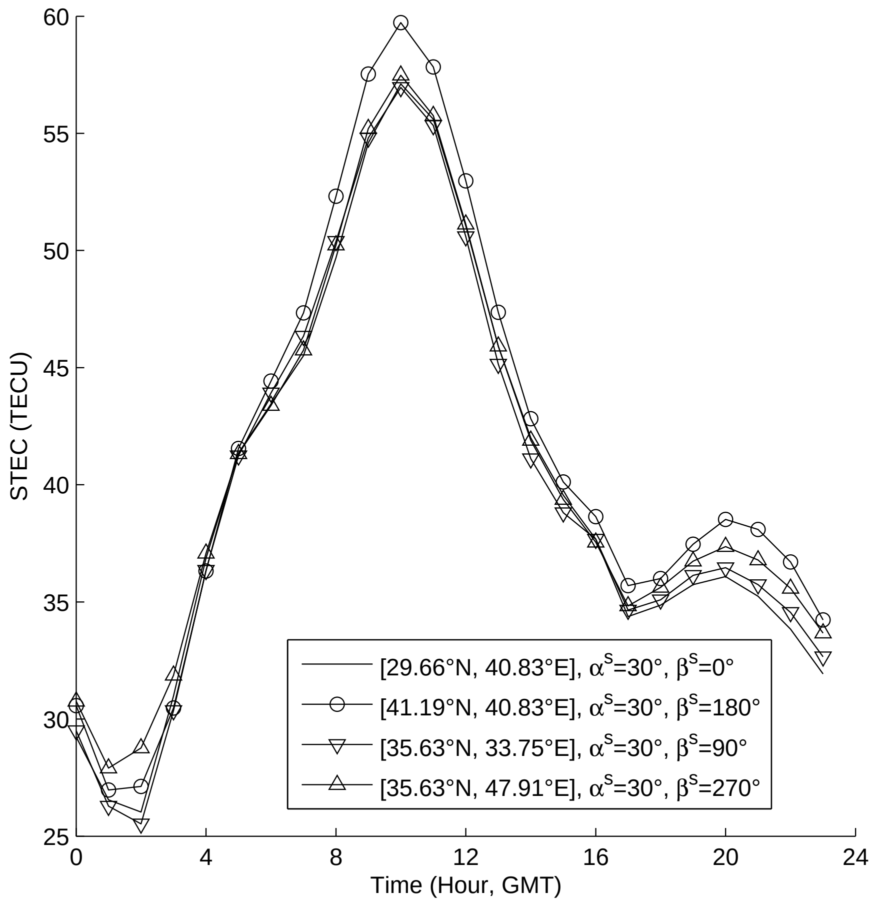

Figure 3.11: IRI-Plas-STEC values for four different receiver and satellite coordinates, all with the same ionospheric pierce point location for thin shell height of 428.8 km, and all with same satellite elevation angle. Date is selected as 30 June 2012.

3.5 Online STEC Calculation Service

In order to provide an online, easy-to-use STEC calculation service to the ionospheric research community, the IRI-Plas-STEC computation technique is implemented as a public web based service at `www.ionolab.org`. Users have to register to the web site before using the IRI-Plas-STEC service. Users do not need to download any program or program code. All the calculations are performed online by the IONOLAB service. For a time of choice, satellite and receiver identifiers, corresponding STEC are calculated and presented to the user online or via e-mail. For receiver parameters, the user can input receiver coordinates or 4-character IGS or EUREF station codes. For satellite identifiers, the user can input the satellite's elevation and azimuth angles or just the corresponding GPS satellite PRN identification number. IRI-Plas-STEC service is a unique application which accepts the IGS or the EUREF station codes and the GPS satellite PRN identification numbers as the slant path input parameters. This property simplifies the model based estimations of STEC corresponding to the real STEC measurement scenarios. Furthermore, optional services for calculating the STEC by sweeping hour of the day, satellite's elevation and azimuth angles are also integrated to this service. IRI-Plas-STEC service is a very flexible tool which can calculate STEC measurements for any synthetic receiver and satellite positions. It can also be used to investigate the variability of STEC in many directions. Figure 3.12 shows a screenshot of the IRI-Plas-STEC service. Following sections summarize IRI-Plas-STEC computation options and present sample outputs.

3.5.1 Single STEC Calculation

Single STEC calculation option is the default functionality provided by the IRI-Plas-STEC service. This option calculates a single STEC value for a given time, receiver and satellite parameters. For receiver parameters, user can choose between specifying the coordinates of the receiver or entering the 4-digit IGS or EUREF station code. For satellite parameters, user can input satellite angles or

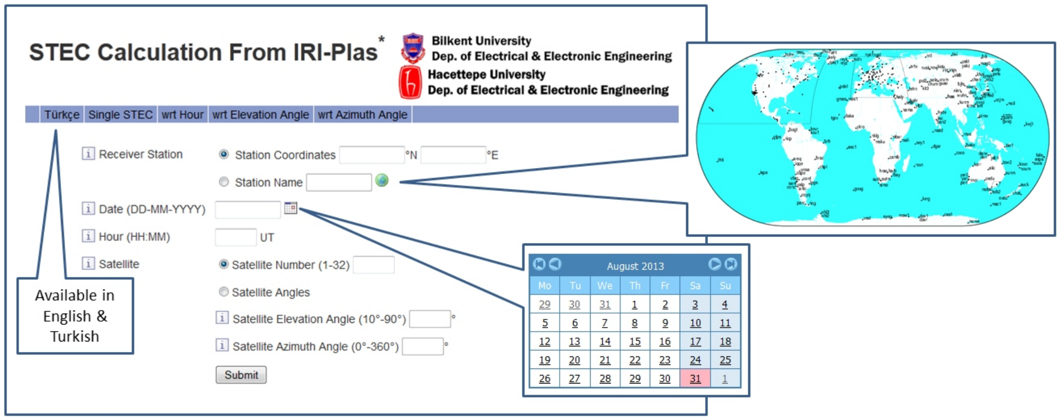

Figure 3.12: Screenshot of online IRI-Plas-STEC service main page at `www.ionolab.org`

a GPS satellite PRN identification number. IRI-Plas-STEC service collects information about the given receiver and satellites, or uses given coordinate and angle parameters directly to calculate the requested STEC value. Results are presented to the user online, together with calculation details such as slant path parameters and electron density values on the slant path obtained from IRI-Plas. Calculation time for a single STEC takes a couple of minutes. Figure 3.13 shows the screenshot of a sample single STEC calculation results. In this example, receiver station is selected as *ista*, which is located in Istanbul, Turkey; calculation date is selected as 13 June 2012, 12:00 GMT; satellite elevation angle is selected as 60°; and the satellite azimuth angle is selected as 25° yielding an estimated result of 28.31 TECU. Calculation details such as the coordinates of the receiver station, coordinates of the slant path as the altitude reaches definite altitude values and the electron density values at these points, and the length of the slant path at each altitude step are also provided to the user.

3.5.2 STEC Calculation with Respect to Hour of the Day

In this option, user provides date, receiver and satellite parameters in order to obtain hourly IRI-Plas-STEC values at a specified date. If the user specifies satellite angles, IRI-Plas-STEC values are calculated hourly for corresponding fixed slant

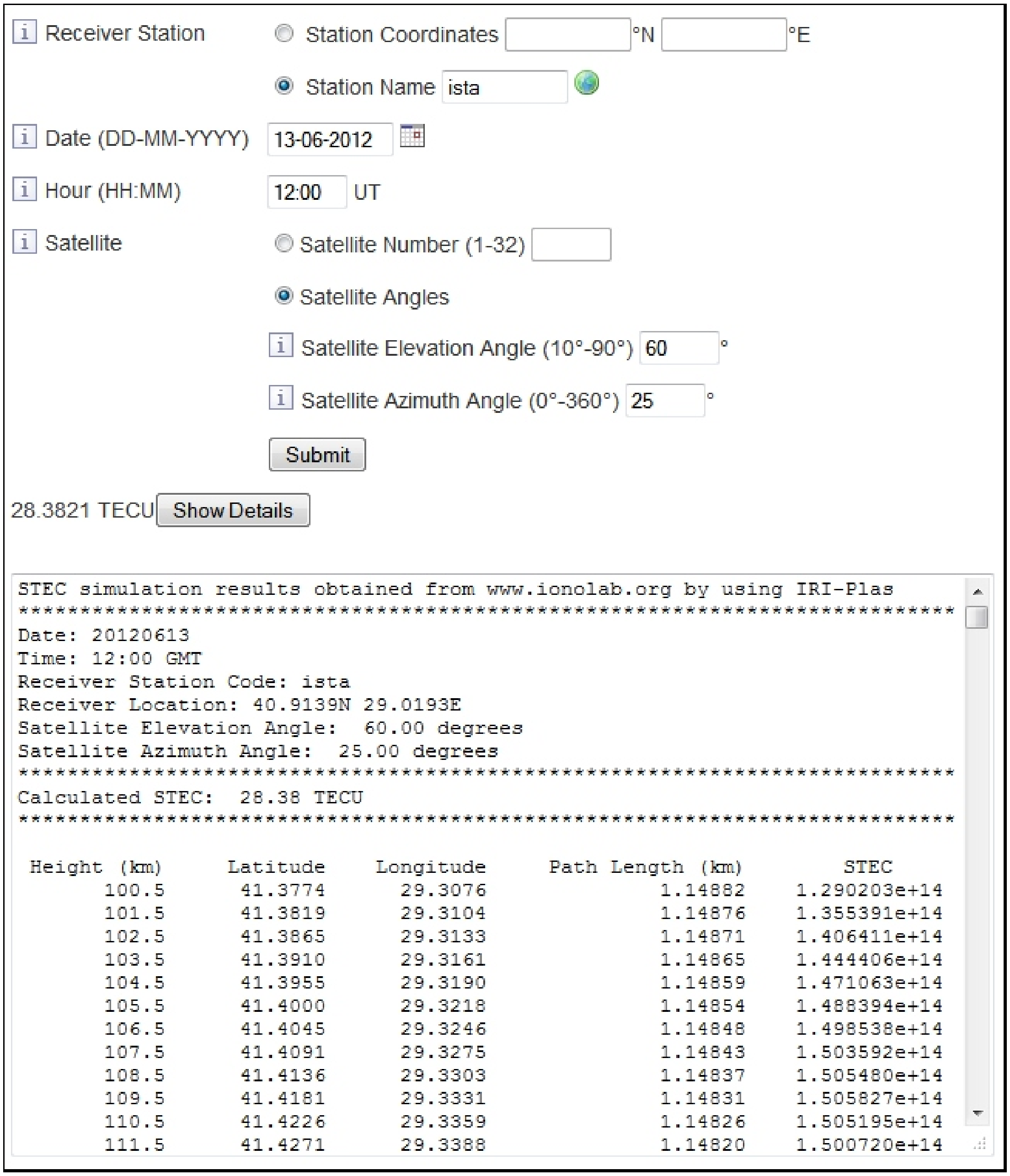

Figure 3.13: Screenshot of the results provided by IRI-Plas-STEC service for a requested single STEC computation.

path. However, if the user specifies the GPS satellite PRN identification number, GPS satellite positions on the given date are obtained from satellite ephemerides data, and IRI-Plas-STEC values are calculated hourly for a slant path that follows the satellite. Calculation time for this option takes about an hour, therefore every calculation request is queued at the server, and when the calculations are completed, user is informed by an e-mail together with the detailed results and a plot of the obtained results. If the user enters the 4-digit IGS or EUREF station code and GPS satellite PRN identification number, this option provides a very informative tool for the comparison of GPS based daily STEC measurements and IRI-Plas based STEC estimates. Figure 3.14 shows a sample email providing the obtained results. In this example, receiver station is selected as *ista*, which is located in Istanbul, Turkey. The calculation date is selected as 11 November 2009, satellite elevation angle and satellite azimuth angle are selected as 66 degrees. IRI-Plas-STEC service automatically retrieves coordinates of the receiver station and calculates STEC values from 00:00 GMT to 23:00 GMT with hourly intervals on the specified date. Figure 3.14 shows that the calculated STEC values change between 5.34 TECU, which is obtained at 03:00 GMT, and 13.80 TECU, which is obtained at 11:00 GMT.

3.5.3 STEC Calculation with Respect to Satellite Elevation Angle

In this option, user provides date, receiver and satellite azimuth angle parameters. User can specify the coordinates of the receiver or enter the 4-digit IGS or EUREF station code. STEC values are calculated for satellite elevation angle values between 10° and 90° with a step size of 10°. Calculation time for this option is about half an hour, which also depends on the overall calculation load on the IONOLAB server. Therefore, every calculation request is queued at the server, and when the calculations are finished, user is informed by an email together with the detailed results and a plot. Figure 3.15 shows content of a sample email. In this example, receiver station is selected as *ankr*, which is located in Ankara, Turkey. The calculation time is selected as 22 June 2010, 11:00 GMT

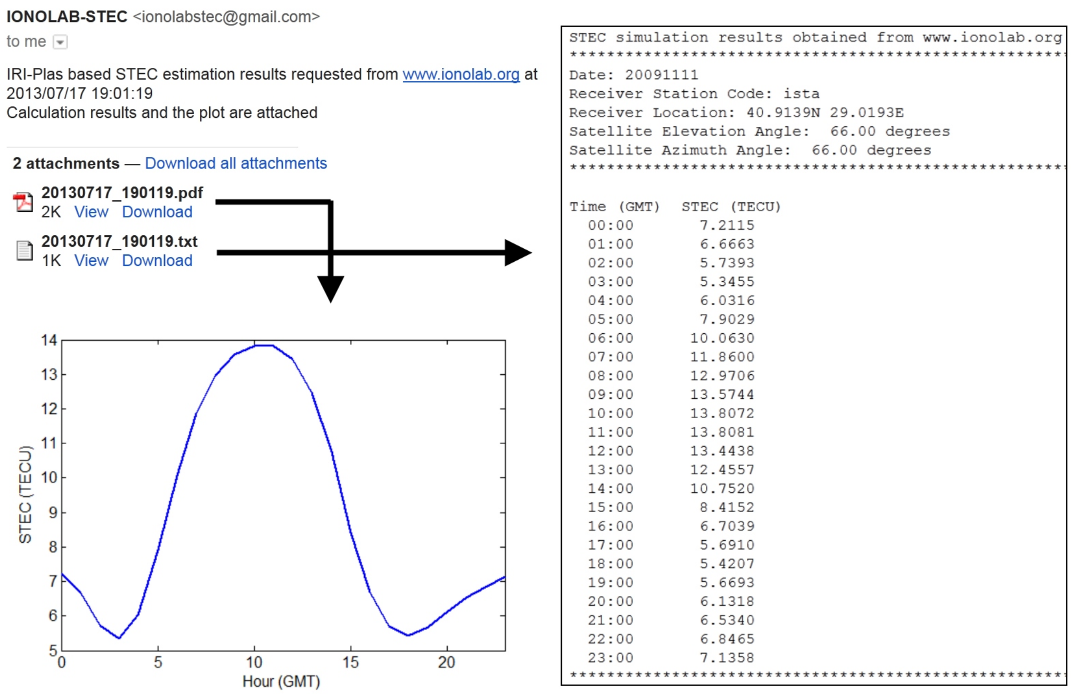

Figure 3.14: Screenshot of an email sent by IRI-Plas-STEC service that contains requested STEC calculation results with respect to hour.

and the satellite azimuth angle is selected as 78 degrees. IRI-Plas-STEC service automatically retrieved coordinates of the receiver station and calculated STEC values for satellite elevation angle values ranging from 10° to 90° with a step size of 10°. Figure 3.15 shows that the calculated STEC values have a range between 16.48 TECU, which is obtained for 85° satellite elevation angle, and 38 TECU, which is obtained for 10° satellite elevation angle.

3.5.4 STEC Calculation with Respect to Satellite Azimuth Angle

In this option, user specifies date, receiver and satellite elevation angles. User can specify the coordinates of the receiver or enter the 4-digit IGS or EUREF station code. STEC values are calculated for satellite azimuth angle values between 0° and 350° with a step size of 10°. Calculation time for this option is about an

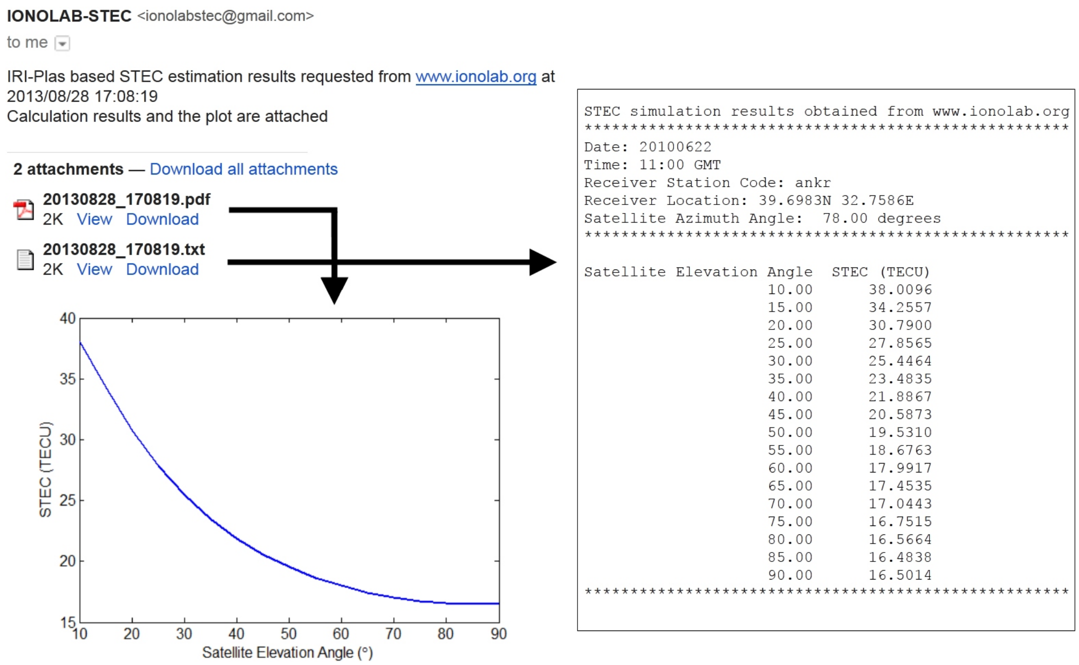

Figure 3.15: Screenshot of an email sent by IRI-Plas-STEC service that contains requested STEC calculation results with respect to satellite elevation angle.

hour, therefore every calculation request is queued at the server, and when the calculations are finished, user is informed by an email together with the detailed results and a plot. This option provides valuable information for analyzing the anisotropic characteristics of the ionosphere. Figure 3.16 shows content of a sample email. In this example, receiver station is selected as *ksmv*, which is located in Kashima, Japan. The calculation date is specified as 29 January 2009, 03:00 GMT and the satellite elevation angle is selected as 60 degrees. IRI-Plas-STEC service automatically retrieved coordinates of the receiver station and calculated STEC values for satellite azimuth angle values ranging from 0° to 350° with a step size of 10°. Figure 3.16 shows that the calculated STEC values have a range between 42.44 TECU, which is obtained for 340° satellite azimuth angle, and 49.08 TECU, which is obtained for 170° satellite azimuth angle.

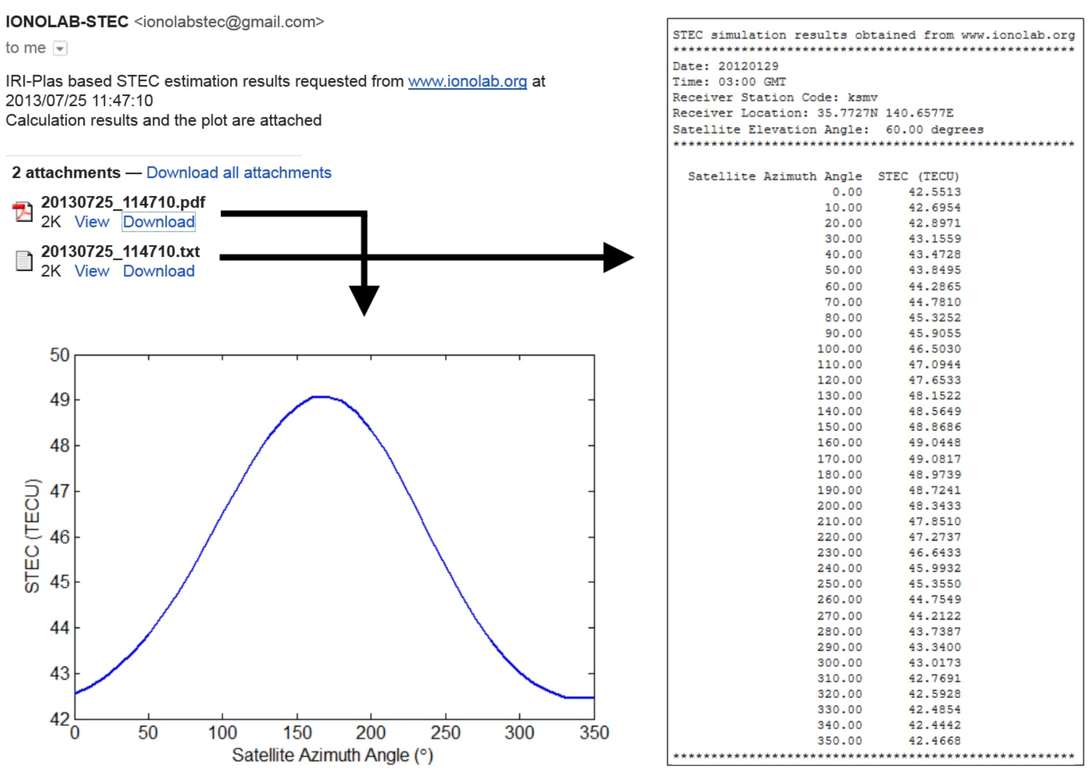

Figure 3.16: Screenshot of an email sent by IRI-Plas-STEC service that contains requested STEC calculation results with respect to satellite azimuth angle.

3.6 Conclusion

An efficient computation technique, namely IRI-Plas-STEC, is proposed for the estimation of STEC from a given 3D model of the ionosphere. IRI-Plas model, which is an extended version of the IRI to the plasmasphere is used for the estimation of the climatic component of the 3D electron density profile in the ionosphere. IRI-Plas-STEC approximates required line integration with a non-uniform Riemann sum for accurate calculation of STEC values from IRI-Plas model. A user-friendly web service based on the presented IRI-Plas-STEC calculation approach has been implemented at the `www.ionolab.org` web site, together with the calculation options such as STEC with respect to the satellite's elevation and azimuth angles and the hour of the day. The IRI-Plas-STEC can be used in various studies for ionospheric research and recovery of GNSS ionospheric delay errors.

Chapter 4

3D Electron Density Estimation in the Ionosphere

4.1 Introduction

In this chapter, a novel technique is proposed to obtain robust and accurate 3D model of the ionosphere by using both the GPS-STEC measurements obtained from a satellite-receiver network and the IRI-Plas model, which is a parametric model of the ionosphere constructed by using the physical structure of the ionosphere and empirical results obtained from various ionospheric measurement tools. This new technique will be referred to as IONOLAB-CIT hereafter.

The main objective of the IONOLAB-CIT is to obtain a 3D electron density distribution which minimizes the mean square error between the real STEC measurements obtained from a GPS receiver network and the corresponding synthetic STEC measurements obtained from the reconstructed 3D electron density distribution. Figure 4.1 shows an illustration of GPS-STEC measurements obtained from a GPS satellite-receiver network. Since GPS-STEC measurements are highly sparse and spatially non-uniformly distributed, obtaining a 3D model of the ionosphere by using only the available GPS-STEC measurements is a highly ill-conditioned problem. To overcome the issues generated by the lack of dense GPS-STEC data, the commonly used approach is to use a set of basis vectors that captures the typical behaviour of the ionosphere and estimate the expansion coefficients of the electron distribution over the chosen basis components [10], [59], [60], [61]. Although this approach provides generally acceptable reconstructions, it fails to capture anomalies that might exist. In IONOLAB-CIT, IRI-Plas model parameters are adjusted to provide physically acceptable reconstructions that are in agreement with the available GPS-STEC measurements. This objective is achieved by modifying the two input parameters of the IRI-Plas model: the F2 layer critical frequency, f_0F_2, and the maximum ionization height, h_mF_2. Both f_0F_2 and h_mF_2 parameters are perturbed by parametric surfaces over the region of interest until the model produces electron distributions whose synthetically computed STEC measurements are in better agreement with the available STEC data. The perturbation surface parameters are optimized by using numerical optimization methods: gradient descent algorithm, Broyden - Fletcher - Goldfarb - Shanno (BFGS) algorithm [62], [63], [64], [65] and Particle Swarm Optimization (PSO) [66].

In development of the IONOLAB-CIT technique, different approaches on the IRI-Plas model parameter selection and perturbation surfaces are investigated. A method using quadratic parametric perturbation surfaces for both f_0F_2 and h_mF_2 are utilized in [67]. A simple approach utilizing a first order perturbation surface only on the f_0F_2 parameter is given in [68]. It has been shown that using linear trends for TEC maps over Turkey has provided acceptable results in previous ionospheric studies [69], [70]. Similarly, in this thesis, first order perturbation surfaces for both f_0F_2 and h_mF_2 are utilized as presented in [18], along with a minor improvement in the cost function of the optimization. The cost function and its parameters given in [18] are readjusted for obtaining more robust results. In the updated cost function, deviation from the physical relation between f_0F_2 and h_mF_2 parameters given in IRI-Plas model has a quadratically increasing penalty, which produces more compliant results with ionosonde measurements.

The proposed IONOLAB-CIT technique is applied extensively to reconstruct regional 3D ionosphere over Turkey, using the data obtained from the Turkish

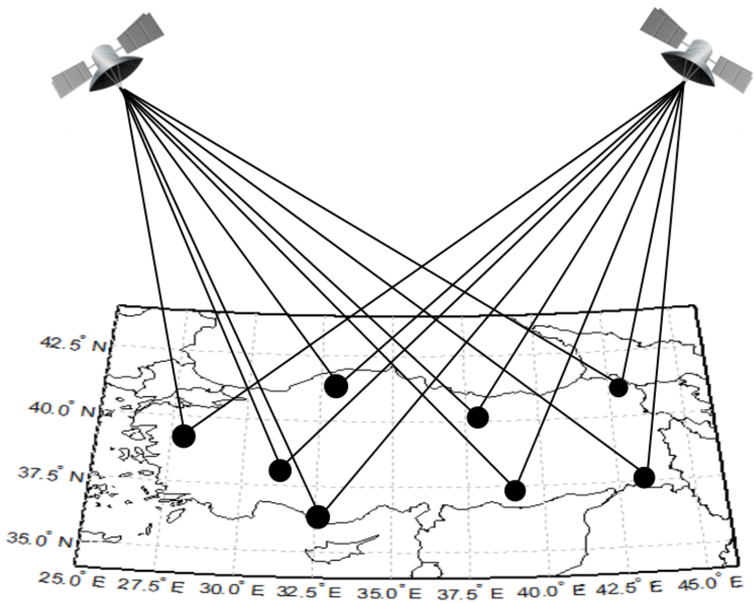

Figure 4.1: An illustration of Total Electron Content measurements by using a GPS satellite-receiver network.

National Permanent GPS Network (TNPGN-Active) for both geomagnetically calm and stormy days of the ionosphere. The map of the GPS receivers can be accessed via `https://www.tkgm.gov.tr/tr/icerik/tusaga-aktif-0`. It is observed that the IONOLAB-CIT provides highly reliable and accurate reconstructions of 3D ionospheric electron density profiles where synthetic STEC calculations and real STEC measurements are in good agreement even during the geomagnetic storm taking place in the ionosphere.

4.2 Model Based STEC Computation

IONOLAB-CIT technique optimizes IRI-Plas model parameters such that the model-based STEC computations provide close approximations to the real STEC measurements. In order to compute the STEC from the IRI-Plas model, an optimized version of the IRI-Plas-STEC computation technique is utilized as discussed in detail in Chapter 3, and [16]. In order to reduce the computational cost required for calculation of STEC values for all receiver-satellite pairs in a GPS receiver network, electron density in each voxel can be computed by using IRI-Plas model and stored in a database. Thus, for each time frame, IRI-Plas-STEC values between the GPS network receivers and the satellites can be expressed as an inner product of two vectors:

$$T_s = \mathbf{b}_s \cdot \mathbf{n}, \tag{4.1}$$

where $\mathbf{n}$ is the vectorized electron density values for all voxels in the region of interest, and $\mathbf{b}_s$ is the vector of pre-calculated values for the corresponding receiver-satellite geometry of the slant path s. Appropriate spatial resolution for the voxels can be chosen as 1° in both latitude and longitude. 3D voxels are stacked in altitude increments starting from a height of 100 km up to 20,000 km. As in Chapter 3, the altitude increments of the voxels are chosen to be 1 km in between 100 km to 600 km, 10 km in between 600 km to 1,300 km, and 50 km in between 1,300 km to 20,000 km. These altitude increments are obtained by modifying the original IRI-Plas code for higher altitude resolution.

4.3 IRI-Plas Model Parameters and Their Effects on the Electron Density Distribution

There are two important IRI-Plas input parameters that governs the variation of electron density. First one is the f_0F2, which corresponds to the critical frequency of F2 layer in the ionosphere, and is directly related with the maximum ionization level. The second one is the h_mF_2, which corresponds to the height of the maximum ionization reached in the F2 layer. Their variation depends mostly on the solar activity, and also long term geomagnetic activities [71], [72]. The effect of changing these two IRI-Plas input parameters are depicted in Figures 4.2, 4.3, and 4.4.

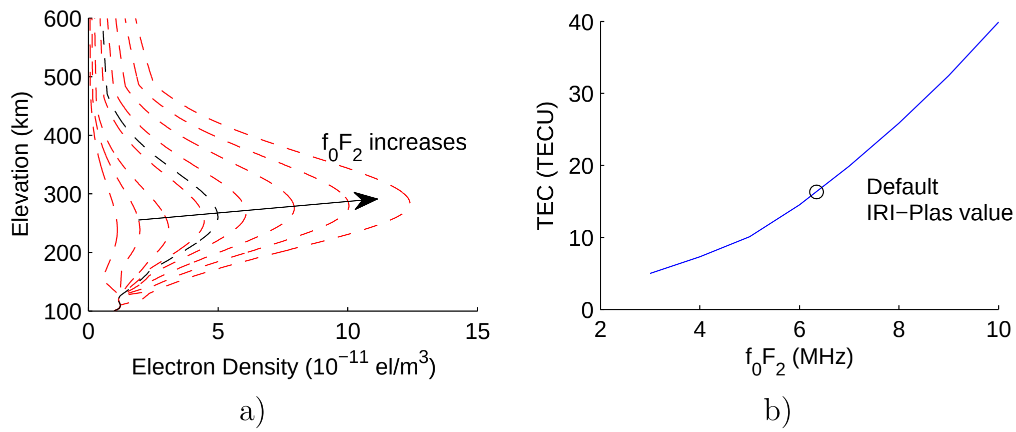

Figure 4.2: Effect of f_0F_2 on the a) electron density profile and b) vertical TEC obtained from IRI-Plas model for 5 May 2010, 12:00 GMT.

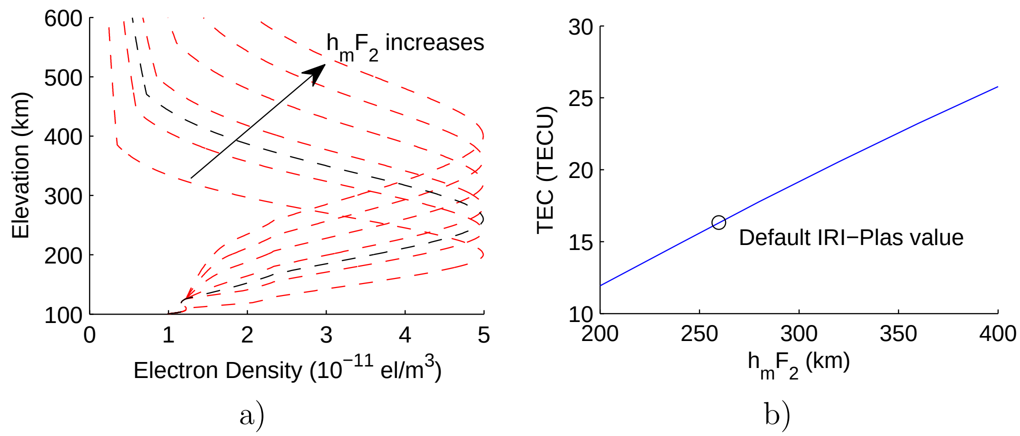

Figure 4.3: Effect of h_mF_2 on the a) electron density profile and b) vertical TEC obtained from IRI-Plas model for 5 May 2010, 12:00 GMT.

Figure 4.4 shows that for a given TEC value, there is more than one solution for f_0F_2 and h_mF_2 pair, since decreasing one of the parameters can be compensated by increasing the other. In order to find a physically acceptable solution, one has to consider both the spatial properties of these parameters and the physical relation between them.

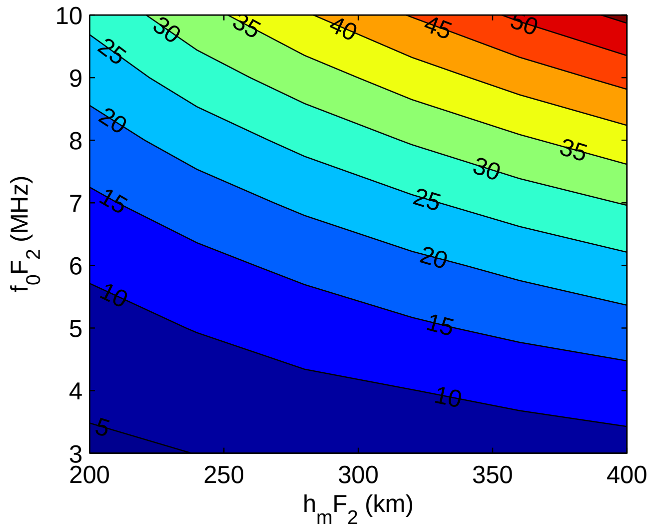

Figure 4.4: Effect of f_0F_2 and h_mF_2 on the vertical TEC obtained from IRI-Plas model for 5 May 2010, 12:00 GMT.

4.4 Regional CIT using the IRI-Plas Model and the GPS-STEC measurements: IONOLAB-CIT

The IONOLAB-CIT technique produces a 3D electron density distribution over a region of interest for the given GPS-STEC measurement set by using parameter optimization methods and the IRI-Plas ionosphere model. Following sections contain the progressive development process of the IONOLAB-CIT technique. First, the CIT problem is defined as an optimization problem, then the problem space is investigated for examining its structure, and finally three different optimization techniques are utilized for solving the CIT problem.

4.4.1 Problem Definition

In this thesis, the CIT problem is defined as an optimization problem where the objective is to find the optimum input parameters for the IRI-Plas model in the region of interest, such that the resultant 3D electron density profile obtained from the IRI-Plas model is in compliance with the available GPS-STEC measurements. The input parameters to be optimized are selected as the f_0F_2 and the h_mF_2, which have significant effects on the electron density distribution in the ionosphere.

It is possible to obtain a physically admissible set of model based VTEC values from the IRI-Plas model by adjusting the f_0F_2 and the h_mF_2 values at a location of interest [73]. However, in order to fit the 3D electron density profile obtained from the IRI-Plas model to a set of STEC measurements obtained over a region, the spatial properties of f_0F_2 and h_mF_2 have to be considered. Along with many other ionospheric parameters, the values of f_0F_2 and h_mF_2 are spatially smooth functions. In this thesis, spatial variations of f_0F_2 and h_mF_2 over the region of interest are modelled as a superposition of first order perturbation surfaces and the default f_0F_2 and h_mF_2 surfaces generated by the IRI-Plas model.

The latitude and the longitude interval of a region of interest over which 3D reconstruction of the ionospheric electron density should be obtained can be defined as:

$$A = \{(\phi, \lambda) | \phi_{min} \leq \phi \leq \phi_{max}, \lambda_{min} \leq \lambda \leq \lambda_{max}\}, \tag{4.2}$$

where ϕ and λ are the latitude and the longitude, respectively. In order to compute the perturbation surface parameters in a geometry-free environment, the perturbation surfaces are modelled in the following normalized coordinates that are bounded within [-1 1] interval:

$$\phi_n = \frac{2\phi - \phi_{max} - \phi_{min}}{\phi_{max} - \phi_{min}}, \tag{4.3}$$

$$\lambda_n = \frac{2\lambda - \lambda_{max} - \lambda_{min}}{\lambda_{max} - \lambda_{min}}. \tag{4.4}$$

First order perturbation surfaces on the default f_0F_2 and h_mF_2 values in region

A are denoted with E_F and E_H, respectively. E_F and E_H can be represented by 3 parameters each, contained in vector $\mathbf{m}$:

$$\mathbf{m} = \begin{bmatrix} \mathbf{m}^f & \mathbf{m}^h \end{bmatrix}, \tag{4.5}$$

where $\mathbf{m}^f$ and $\mathbf{m}^h$ are defined as:

$$\mathbf{m}^f = \begin{bmatrix} m_1^f & m_2^f & m_3^f \end{bmatrix}, \tag{4.6}$$

$$\mathbf{m}^h = \begin{bmatrix} m_1^h & m_2^h & m_3^h \end{bmatrix}. \tag{4.7}$$

The values of E_F and E_H at any location in A can be calculated by using the following equations:

$$E_F(\phi, \lambda, \mathbf{m}^f) = m_1^f \phi_n + m_2^f \lambda_n + m_3^f, \tag{4.8}$$

$$E_H(\phi, \lambda, \mathbf{m}^h) = m_1^h \phi_n + m_2^h \lambda_n + m_3^h. \tag{4.9}$$

Specifically, perturbed f_0F_2 and h_mF_2 values for any given location in A are obtained by using the following equations:

$$F_{opt}(\phi, \lambda, \mathbf{m}^f) = S\left(F(\phi, \lambda) + E_F(\phi, \lambda, \mathbf{m}^f), F_{min}, F_{max}\right), \tag{4.10}$$

$$\begin{aligned} H_{opt}(\phi, \lambda, F_{opt}(\phi, \lambda, \mathbf{m}^f), \mathbf{m}^h) = \\ S\left(H(\phi, \lambda, F_{opt}(\phi, \lambda, \mathbf{m}^f)) + E_H(\phi, \lambda, \mathbf{m}^h), H_{min}, H_{max}\right), \end{aligned} \tag{4.11}$$

where $F(\phi, \lambda)$ is the default value of f_0F_2 obtained from the IRI-Plas for the given latitude ϕ and the longitude λ, $F_{opt}(\phi, \lambda, \mathbf{m}^f)$ is the modified f_0F_2 parameter by using the perturbation surface parameters in $\mathbf{m}^f$, $H(\phi, \lambda, F_{opt}(\phi, \lambda, \mathbf{m}^f))$ is the default value of h_mF_2 obtained from the IRI-Plas for the given latitude ϕ, the longitude λ, and modified f_0F_2 parameter, $H_{opt}(\phi, \lambda, F_{opt}(\phi, \lambda, \mathbf{m}^f), \mathbf{m}^h)$ is the modified h_mF_2 parameter by using the perturbation surface obtained by the parameters in $\mathbf{m}^h$ onto the $H(\phi, \lambda, F_{opt}(\phi, \lambda, \mathbf{m}^f))$ surface, and S is a sigmoid-like function for bounding the results within given physical limits, $F_{min} - F_{max}$ and $H_{min} - H_{max}$.

S is defined in a way that if the input value is in between and not close to the bounding limits, it returns the same value for the output. However, if the input value is close to the bounding limits, or exceeds these limits, S provides an output asymptotically approaching to the bounding limits. This property of S provides a one-to-one function, and is important for preserving the direction of the gradient information in the problem space which is essential for many optimization methods. For the given lower limit σ_1 and the higher limit σ_2, S can be defined as:

$$S(r, \sigma_1, \sigma_2) = \begin{cases} \sigma_1 + \frac{2(\sigma_1' - \sigma_1)}{1+e^{-2\mu_1}} & \text{if } r < \sigma_1' \\ r & \text{if } \sigma_2' \geq r \geq \sigma_1' \\ \sigma_2 + \frac{2(\sigma_2' - \sigma_2)}{1+e^{-2\mu_2}} & \text{if } r > \sigma_2' \end{cases}, \tag{4.12}$$

where σ_1', σ_2', μ_1 and μ_2 are:

$$\sigma_1' = \sigma_1 + \frac{\sigma_2 - \sigma_1}{10}, \tag{4.13}$$

$$\sigma_2' = \sigma_2 - \frac{\sigma_2 - \sigma_1}{10}. \tag{4.14}$$

$$\mu_1 = \frac{r - \sigma_1'}{\sigma_1' - \sigma_1}, \tag{4.15}$$

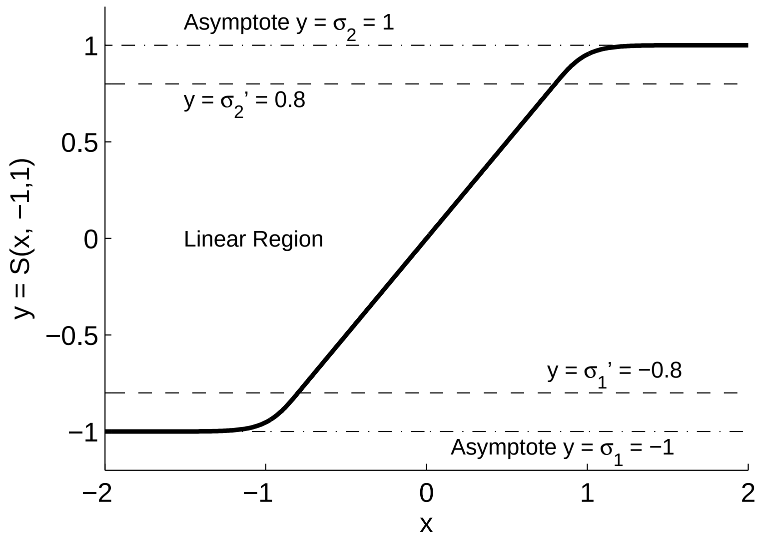

Figure 4.5: Plot of $y = S(x, -1, 1)$.

$$\mu_2 = \frac{r - \sigma_2'}{\sigma_2' - \sigma_2}. \tag{4.16}$$

A sample plot for depicting sigmoid function S is given in Figure 4.5.

A physically admissible 3D ionospheric reconstruction can be obtained for any choice of parameters in $\mathbf{m}$. The challenge is the identification of the optimal $\mathbf{m}$ for which the synthetically generated 3D ionosphere would provide STEC values that are closest to the actual measurements. Furthermore, the physical relation between the ionosphere parameters obtained for given $\mathbf{m}$ should also be considered. For a specific choice of $\mathbf{m}$, the following cost function can be used in the search for the optimal $\mathbf{m}$:

$$\begin{aligned} C(\mathbf{m}) =& \sqrt{\frac{\sum_s (T_s(\mathbf{m}) - M_s)^2}{\sum_s M_s^2}} \\ &+ \rho \frac{\sum_i \sum_j \left(H_{opt}(\phi_i, \lambda_j, F_{opt}(\phi, \lambda, \mathbf{m}^f), \mathbf{m}^h) - H(\phi_i, \lambda_j, F_{opt}(\phi, \lambda, \mathbf{m}^f))\right)^2}{\sum_i \sum_j H(\phi_i, \lambda_j, F_{opt}(\phi, \lambda, \mathbf{m}^f))^2}, \end{aligned} \tag{4.17}$$

where $T_s(\mathbf{m})$ is the calculated STEC along s for the 3D electron density matrix obtained from the IRI-Plas in region A for the given parameter set $\mathbf{m}$, M_s is the real GPS-STEC measurement obtained along s, ϕ_i and λ_j are the discrete latitude and the longitudes spanning the region A with a step size of $1°$, and ρ is an adjustable weight parameter which determines the relaxation on the physical relation between f_0F_2 and h_mF_2 parameters.

Computation of the cost function defined in (4.17) requires multiple preliminary steps. The coordinates of the GPS receiver stations, and the pseudo range and phase delay information computed at the GPS receiver stations are retrieved via RINEX files. The IONEX files are retrieved from publicly available ftp servers for the computation of receiver inter-frequency biases by using the IONOLAB-BIAS method. The GPS satellite tracks are retrieved from GPS ephemerides data provided by IGS. By using the pseudo range and phase delay information obtained via RINEX files, and the receiver inter-frequency biases obtained by the IONOLAB-BIAS method, STEC measurement between the receiver and the satellite is calculated by using the IONOLAB-STEC method. The detailed information about the IGS, IGS Ephemeris data, RINEX and IONEX files are given in Appendix B. The detailed information about the IONOLAB-BIAS can be found in [38]. The detailed information about the IONOLAB-STEC can be found in [34], [39]. After obtaining real GPS-STEC measurements by using IONOLAB-STEC method, IRI-Plas model is utilized for obtaining the 3D electron density estimation over the region of interest for the given parameter set, and the IRI-Plas-STEC values are calculated from this 3D electron density distribution for the corresponding receiver-satellite geometry. By using the difference between the IONOLAB-STEC and IRI-Plas-STEC values, IRI-Plas parameters f_0F_2 and h_mF_2 are optimized in the region of interest for minimizing the difference. The required steps and the structure of the proposed IONOLAB-CIT technique for minimizing the cost function is shown in Figure 4.6.

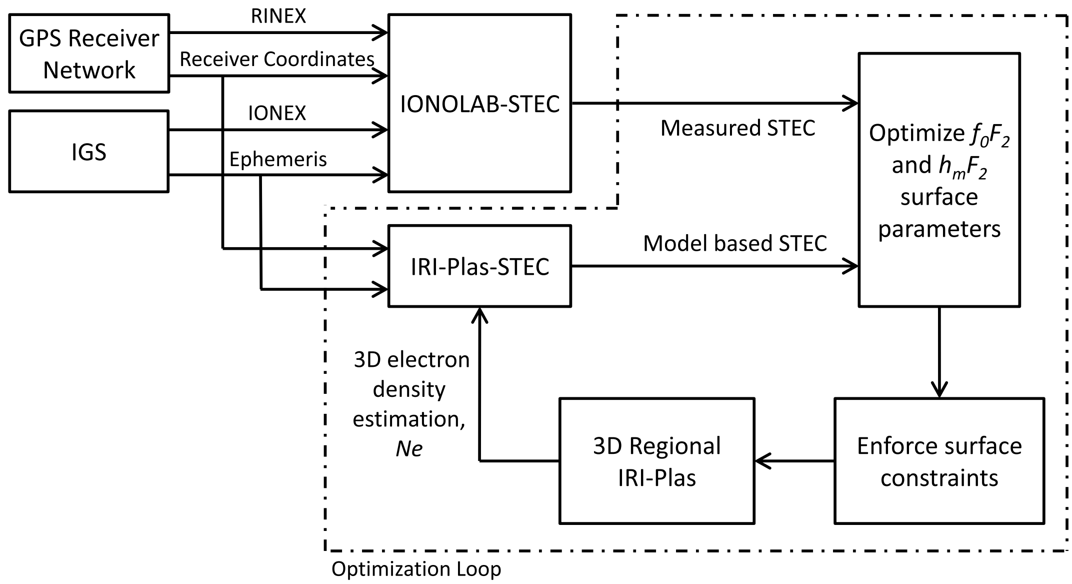

Figure 4.6: Graphical structure of the proposed 3D ionospheric reconstruction technique. Input parameters, that are searched by numerical optimization methods are fed to regional IRI-Plas model so that the discrepancy between synthetic STEC values derived from the model based reconstruction and the actual STEC values derived from the GPS measurements is minimized.

4.4.2 Investigation of the Problem Space

In the problem definition, the CIT problem is reduced to a 6 parameter optimization problem. Before utilizing an optimization technique, it is important to investigate the problem space for the structure of the cost surface. Since it is not possible to visualize 6 dimensional problem space at once, here we will investigate the cost surface over randomly selected 2 dimensional planes in the problem space. Figures 4.7a, b, c, d show a selection of these planes. In order to generate these figures, discrete values of $\mathbf{m}$ corresponding to the points lying on the selected 2-D planes are evaluated. Planes given in these figures do not contain any local minima, which indicates that using Newtonian methods for the optimization is expected to produce acceptable results. However it is not possible to say that the 6D problem space does not contain any local minima only by looking at a set of randomly selected 2D planar cost surfaces. Moreover, the problem space depends on the given measurement set, therefore one can not conclude that the problem space contain local minima or not by inspecting only a limited set of problems. Therefore, although the investigations on the problem space seems to be very suitable for the Newtonian techniques of optimization, utilizing stochastic methods which are robust against the local minima, can be useful in some scenarios.

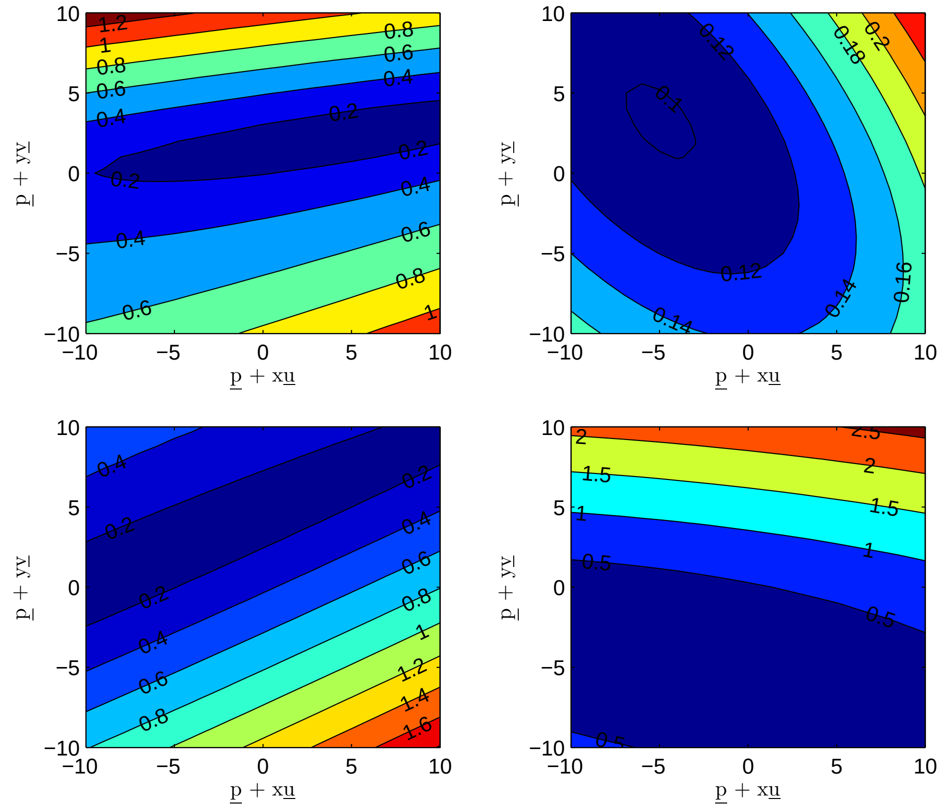

Figure 4.7: Cost values obtained for 2D planes randomly extracted from 6D problem space.

a) 10 March 2011, 22:00 GMT,
p = [0.7184 0.9686 0.5313 3.2515 1.0563 6.1096],
u = [0.1828 0.0994 0.0213 0.6254 0.3607 0.6596],
v = [-0.9028 -0.3651 0.0722 0.0783 0.1032 0.1722],
b) 28 May 2011, 17:00 GMT,
p = [0.3724 0.1981 0.4897 3.3949 9.5163 9.2033],
u = [0.0045 0.0629 0.0230 0.3607 0.4674 0.8043],
v = [0.0780 0.0733 0.0148 0.7084 0.4113 -0.5633],
c) 12 June 2011, 14:00 GMT,
p = [0.8181 0.8175 0.7224 1.4987 6.5961 5.1859],
u = [0.0930 0.0620 0.0765 0.4338 0.4134 0.7890],
v = [-0.2411 -0.1419 -0.1727 -0.2641 0.8703 -0.2544],
d) 1 September 2011, 02:00 GMT,
p = [0.7655 0.7952 0.1869 4.8976 4.4559 6.4631],
u = [0.0736 0.0783 0.0286 0.7052 0.6796 0.1687],
v = [-0.1655 -0.0157 0.3297 -0.6096 0.5221 0.4684].

4.4.3 Minimization of the Cost Function

In order to find the $\mathbf{m}$ which minimizes $C(\mathbf{m})$, gradient descent (GD) algorithm, Broyden - Fletcher - Goldfarb - Shanno (BFGS) algorithm, and Particle Swarm Optimization (PSO) techniques are utilized. The gradient descent is an iterative optimization technique which uses the first order derivatives of the function for taking steps in the problem space, whereas BFGS method uses both the first order derivatives and the second order derivatives which are derived again from the first order derivatives of the function. In our case, since the gradient of the problem space can not be calculated analytically, finite difference approximation method is used for calculation of the gradient as follows:

$$\nabla C(\mathbf{m}) = \sum_{d=1}^{n} \frac{C(\mathbf{m} + \epsilon \mathbf{z}_d) - C(\mathbf{m})}{\epsilon \|\mathbf{z}_d\|} \frac{\mathbf{z}_d}{\|\mathbf{z}_d\|}, \tag{4.18}$$

where $\mathbf{z}_d$ represents dth of a set of n orthogonal vectors in n dimensional problem space, and ϵ is a small non-negative real number.

The gradient descent method uses the below update equation for the variables of optimization, where k subscript is used for denoting the iteration number:

$$\mathbf{m}_{k+1} = \mathbf{m}_k - \psi_k \nabla C(\mathbf{m}_k), \tag{4.19}$$

ψ_k is the step size parameter found by using a line search algorithm.

The BFGS method uses the following equations for the variable updates, where k subscript is used for denoting the iteration number:

$$\mathbf{B}_k \mathbf{p}_k = -\nabla C(\mathbf{m}_k), \tag{4.20}$$

$$\mathbf{m}_{k+1} = \mathbf{m}_k + \psi_k \mathbf{p}_k, \tag{4.21}$$

$$\mathbf{s}_k = \psi_k \mathbf{p}_k, \tag{4.22}$$

$$\mathbf{y}_k = \nabla C(\mathbf{m}_{k+1}) - \nabla C(\mathbf{m}_k), \tag{4.23}$$

$$\mathbf{B}_{k+1} = \mathbf{B}_k + \frac{\mathbf{y}_k \mathbf{y}_k^T}{\mathbf{y}_k^T \mathbf{s}_k} - \frac{\mathbf{B}_k \mathbf{s}_k \mathbf{s}_k^T \mathbf{B}_k}{\mathbf{s}_k^T \mathbf{B}_k \mathbf{s}_k}. \tag{4.24}$$

ψ_k is again found by using a line search algorithm. $\mathbf{B}$ is the approximation of the Hessian matrix which is updated at each iteration. The initial value for $\mathbf{B}$ is used as the identity matrix.

In order to prevent narrow valleys in the problem space, which causes pathological problems in both methods, and since the effect of the h_mF_2 on the STEC values is very low with respect to the f_0F_2, the problem space is scaled down along the dimensions of h_mF_2 perturbation surface parameters by a factor of 100. The perturbation surface parameters for a point in the scaled problem space spanned by array $\boldsymbol{\eta}$ are calculated as follows:

$$\mathbf{m} = \begin{bmatrix} \eta_1 & \eta_2 & \eta_3 & 100\eta_4 & 100\eta_5 & 100\eta_6 \end{bmatrix}. \tag{4.25}$$

The starting points in both methods are set as the origin of the 6D problem space, which corresponds to the default IRI-Plas solution. The initial step size at each iteration is selected as an exponentially decaying function with respect to the iteration number and does not depend on the gradient. A backtracking line search based on Armijo-Goldstein condition [74] is employed in both methods, with a step size reduction ratio of 1/2.

Both gradient descent and BFGS methods fail when optimizing functions with local minima. In this CIT problem, it is not possible to determine if the problem space has local minima or not, since the problem space depends on the actual measurements obtained from the GPS receivers. For this reason, PSO which is a stochastic and iterative optimization technique, is also employed. It uses a swarm of candidate solution points, called as particles, and tries to find the optimum solution by simply moving the particles in the problem space. Particles have the memory of the best position they have found so far, and communicate with each other to learn the best position swarm has found so far. At each iteration, particles move in the problem space based on their velocity and acceleration parameters. The updated locations of the particles are evaluated by using the cost function. The particles update their best personal positions based on the results, and they communicate with each other for updating the global best position of the swarm. After that, particles are accelerated towards the best personal solution and the best global solution, with random amounts. PSO does not make assumptions about the problem space, and it is highly robust against functions with local minima. In this thesis, global communication topology is used in PSO, in which every particle except the particle itself contributes to the calculation of the global best position of that particle. The particle velocities and positions are updated by using the following equations:

$$V_k^n = w_1 V_{k-1}^n + w_2 Z_1 (B_k^n - P_k^n) + w_3 Z_2 (D_k^n - P_k^n), \tag{4.26}$$

$$P_{k+1}^n = P_k^n + V_k^n, \tag{4.27}$$

where P_k^n is the position of the particle n, V_k^n is its velocity, B_k^n is its personal best position, and D_k^n is the global best position found by the particles other than the particle n, at iteration k. Z_1 and Z_2 are random variables uniformly distributed in [0 1]. The velocity update coefficient w_1 is selected as 0.5, the acceleration coefficients w_2 and w_3 are selected as 0.05, and the number of particles in the simulations are selected as 100, as in [67].

Among the discussed three different optimization methods, gradient descent and BFGS are deterministic methods for given starting point and step size parameters. PSO, on the other hand, is a stochastic optimization method, and the results obtained for different runs typically differ from each other. The computational cost of the PSO is generally higher than the other two approaches, however PSO is generally preferred for its robustness against local minima.

4.5 Computational Cost Analysis

For each calculation of the cost function, the proposed IONOLAB-CIT technique requires the following computations:

- Computation of the default h_mF_2 surface in the region of interest by using IRI-Plas model, for the given input f_0f_2 surface which is perturbed with the parameters in $\mathbf{m}^f$.
- Computation of the 3D electron density distribution in the region of interest for the given parameter set $\mathbf{m}$ by using the IRI-Plas model.
- Computation of the set of synthetic STECs corresponding to the actual receiver and satellite positions over the reconstructed 3D electron density distribution.
- Computation of the cost function in (4.17) by using real measurement data, computed synthetic STECs and the ionospheric parameters h_mF_2 and f_0F_2.

Computation time of top two items listed above take more than 98% of the total computation time of a single cost function calculation. Therefore, the number of STEC measurements used in the reconstruction set and the computation of the cost function do not affect the total computation time significantly.

Regardless of the chosen optimization technique, above listed computations are needed for the performance evaluation of a single candidate solution. However, number of evaluations in each iteration do change with respect to the utilized optimization technique. For example, GD and BFGS methods require a single

Table 4.1: Comparions of computational cost for three optimization methods.

Optimization Method	Number of cost function evaluations for 1 iteration
GD	Number of dimensions of the problem space + Number of steps taken in line search algorithm
BFGS	Number of dimensions of the problem space + Number of steps taken in line search algorithm
PSO	Number of particles used in PSO

evaluation for each dimension for computation of the gradient in the multidimensional problem space, and 1 to 10 evaluations for backtracking line search algorithm for moving in the problem space along the negative gradient. PSO, on the other hand, require evaluation of the cost function belonging to each particle in the problem space. Since a 6D problem space is used in the proposed approach, 7-16 cost function evaluations are required for a single iteration of the GD and the BFGS methods. The number of particles used in the PSO method is 100, which corresponds to 100 cost function evaluations for each iteration. Table 4.1 compares the three methods in terms of computational cost. Although the number of calculations are high, they can be processed in parallel since most of the cost function evaluations are independent from each other. If the parallel processing units are sufficiently high, then GD and BFGS methods require one cost function computation time to determine the gradient, and after that, one cost function computation time for backtracking line search algorithm, within a single iteration, PSO on the other hand requires only one cost function computation time within a single iteration, since all the cost function evaluations can be processed in parallel.

In our implementations, utilizing GD and BFGS methods in the IONOLAB-CIT technique takes about 30-60 minutes computation time in an octa-core processing system, depending on the number of iterations until convergence. PSO on the other hand takes about 10 hours computation time in an octa-core processing system, where always maximum number of iterations are used.

4.6 Experimental Results

This section contains experimental results obtained by the IONOLAB-CIT technique. Six different types of experiments are conducted in total. In the first five experiments, the region of interest is chosen over Turkish borders. The limits of the region for estimating the 3D electron density distribution is selected in between 34° N and 44° N latitudes, 24° E and 47° E longitudes, and 100 and 20,000 km in height. In the sixth experiment, the region of interest is shifted to the West such that it covers the Greece and Western Turkey. The region in this case is selected in between 34° N and 44° N latitudes, 19° E and 42° E longitudes, and 100 and 20,000 km in height. Each experiment explained in detail and obtained results are given below.

First, in order to validate the proposed IONOLAB-CIT technique, its performance is experimented on the simulated data. Parametric disturbance surfaces over default IRI-Plas parameters f_0F_2 and h_mF_2 are constructed with parameters $\mathbf{m} = [\ 0.8 \quad -0.4 \quad 0.5 \quad 12 \quad 8 \quad 15\ ]$. Then, a 3D electron density distribution is obtained by using the IRI-Plas model and disturbed f_0F_2 and h_mF_2 parameter surfaces, at 10:00 GMT on 1 June 2011. By using the actual geometry of the TNPGN-Active receivers and the GPS satellites at the given time, synthetic STEC measurements are calculated by using (4.1). Then, the obtained synthetic STECs are fed to the IONOLAB-CIT technique in order to find the optimum perturbation surface parameters. ρ in (4.17) is used as 0 in the experiments, which means that the cost value for the optimum solution is zero. The output of the cost function with respect to iteration number obtained for each optimization method is given in Figure 4.8. The initial cost function obtained for the synthetically disturbed ionosphere is 0.195, and all methods have successfully decreased the cost function below 0.020 after 100 iterations. However, results indicate that the BFGS provides the fastest convergence among all the proposed methods.

Second, the IONOLAB-CIT technique is experimented on the real measurement data (IONOLAB-STEC) which has been provided by the TNPGN-Active. Two different dates are selected for the simulations, which are 12:00 GMT on

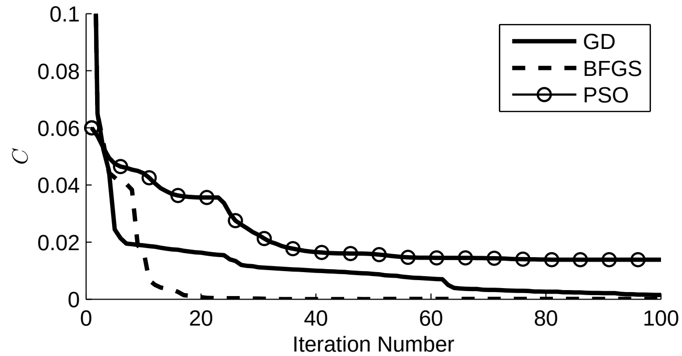

Figure 4.8: Cost function for three different optimization methods with respect to iteration count, obtained for synthetic measurement data on 1 June 2011, at 10:00 GMT. The initial cost value obtained by using default IRI-Plas parameters is 0.195.

1 September 2011 and 12:00 GMT on 10 March 2011. 1 September 2011 is a calm day and 10 March 2011 is a stormy day. In order to choose the appropriate set of STEC measurements from the IONOLAB-STEC database obtained from the TNPGN-Active stations, all receiver stations are checked if they have generated valid STEC measurements for any satellites in the given time. Next, STEC measurements for the elevation angles which are lower than 30° are filtered out. Since 80% of the electron density distribution in the ionosphere is in between 100 km and 1,500 km height, the STEC measurements obtained along slant paths which stay inside the region A below 1,500 km elevation are selected as valid measurements to be used in the IONOLAB-CIT technique. For this part of the experiment, ρ in (4.17) is selected as 3. Results obtained for the selected dates are shown in Figures 4.9 and 4.11, respectively. Figures 4.9a and 4.11a show the cost as a function of iterations for each of the optimization methods. As seen from these figures, the cost is decreased from 0.16 to 0.07 for the calm day, and from 0.43 to 0.03 for the disturbed day, respectively. Figures 4.9b and 4.11b show the default VTEC maps obtained by using the IRI-Plas model in the region. Figures 4.9c and 4.11c show the VTEC maps calculated by using the IRI-Plas model and the optimized parameters obtained by the BFGS method. Figures 4.10 and 4.12 show the perturbation surfaces and the resultant surfaces corresponding to the optimized parameters obtained by the BFGS method. Results show that the required number of iterations for the convergence of the obtained reconstructions

for both the calm and the disturbed days are very similar. Figures 4.13 and 4.14 show electron density slices extracted from the 3D electron density distributions obtained by using IRI-Plas model and the IONOLAB-CIT technique with the BFGS optimization method for selected dates. Figures 4.13a, b and 4.14a, b, show electron density slices obtained from IRI-Plas model for fixed latitudes (35° N, 38° N, 41° N, 44° N) and fixed longitudes (25° E, 32° E, 39° E, 46° E), respectively. Figures 4.13c, d and 4.14c, d, show electron density slices obtained by using IONOLAB-CIT for fixed latitudes (35° N, 38° N, 41° N, 44° N) and fixed longitudes (25° E, 32° E, 39° E, 46° E), respectively. Figure 4.15 shows the comparison of electron density values along sample GPS receiver - satellite paths computed from 3D electron density distributions of the IRI-Plas model and the IONOLAB-CIT technique.

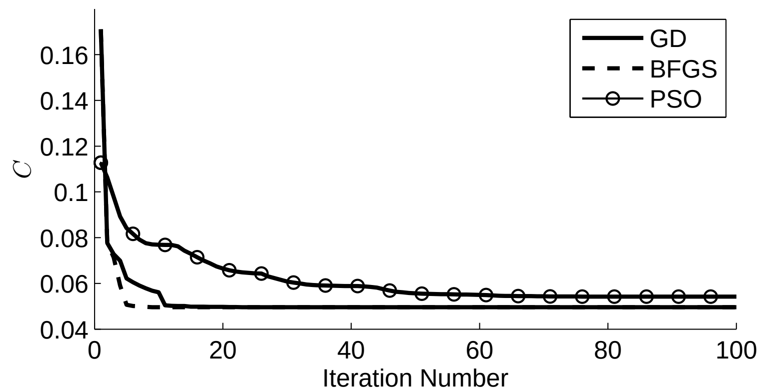

a)

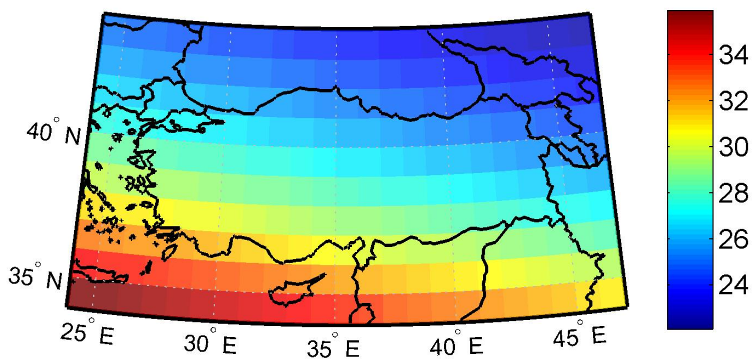

b)

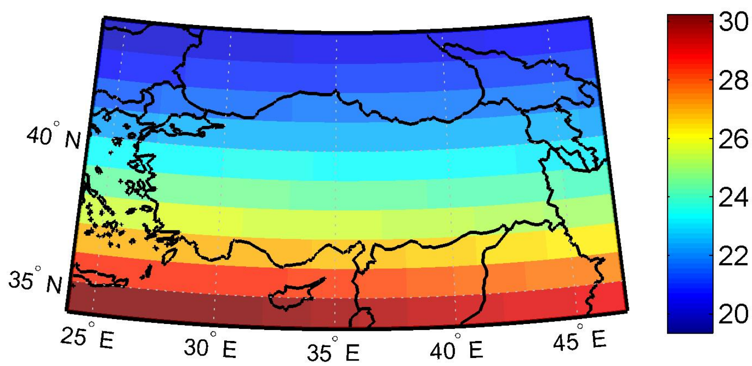

c)

Figure 4.9: 1 September 2011, 12:00 GMT, a) Cost function for three different optimization methods with respect to iteration count, b) IRI-Plas TEC (TECU), c) IONOLAB-CIT TEC (TECU).

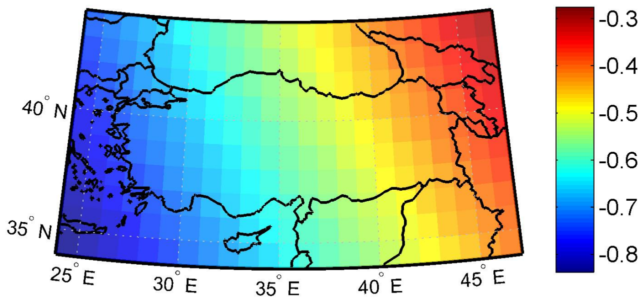

a)

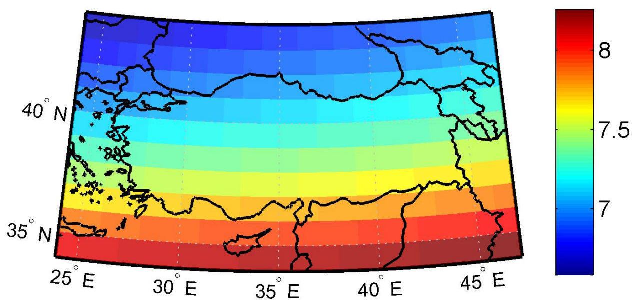

b)

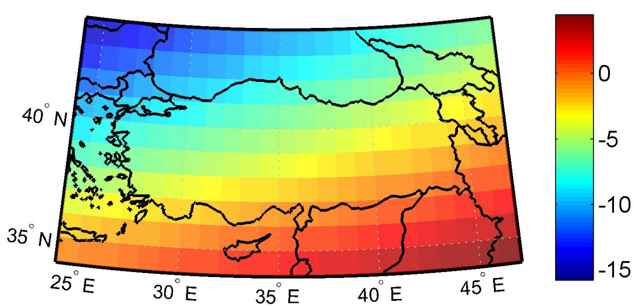

c)

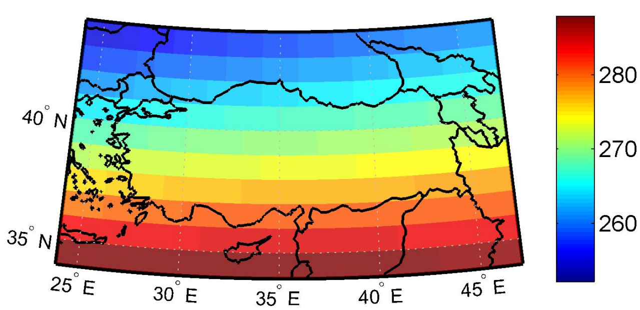

d)

Figure 4.10: 1 September 2011, 12:00 GMT, a) optimized f_0F_2 perturbation surface (MHz), b) optimized f_0F_2 surface (MHz), c) optimized h_mF_2 perturbation surface (km), d) optimized h_mF_2 surface (km).

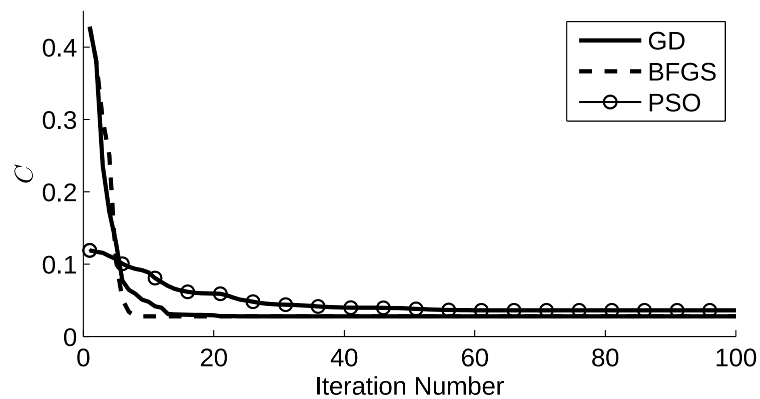

a)

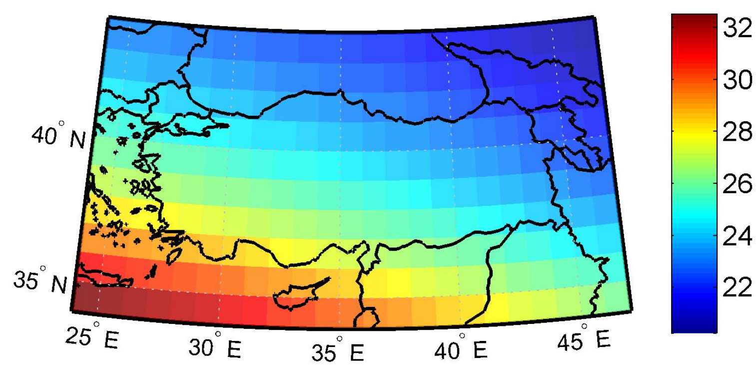

b)

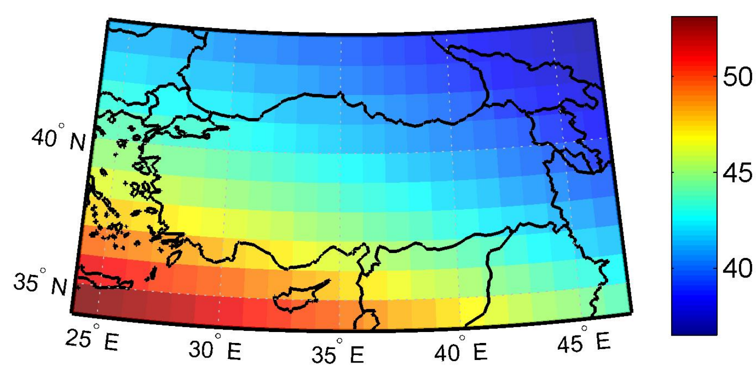

c)

Figure 4.11: 10 March 2011, 12:00 GMT, a) Cost function for three different optimization methods with respect to iteration count, b) IRI-Plas TEC (TECU), c) IONOLAB-CIT TEC (TECU).

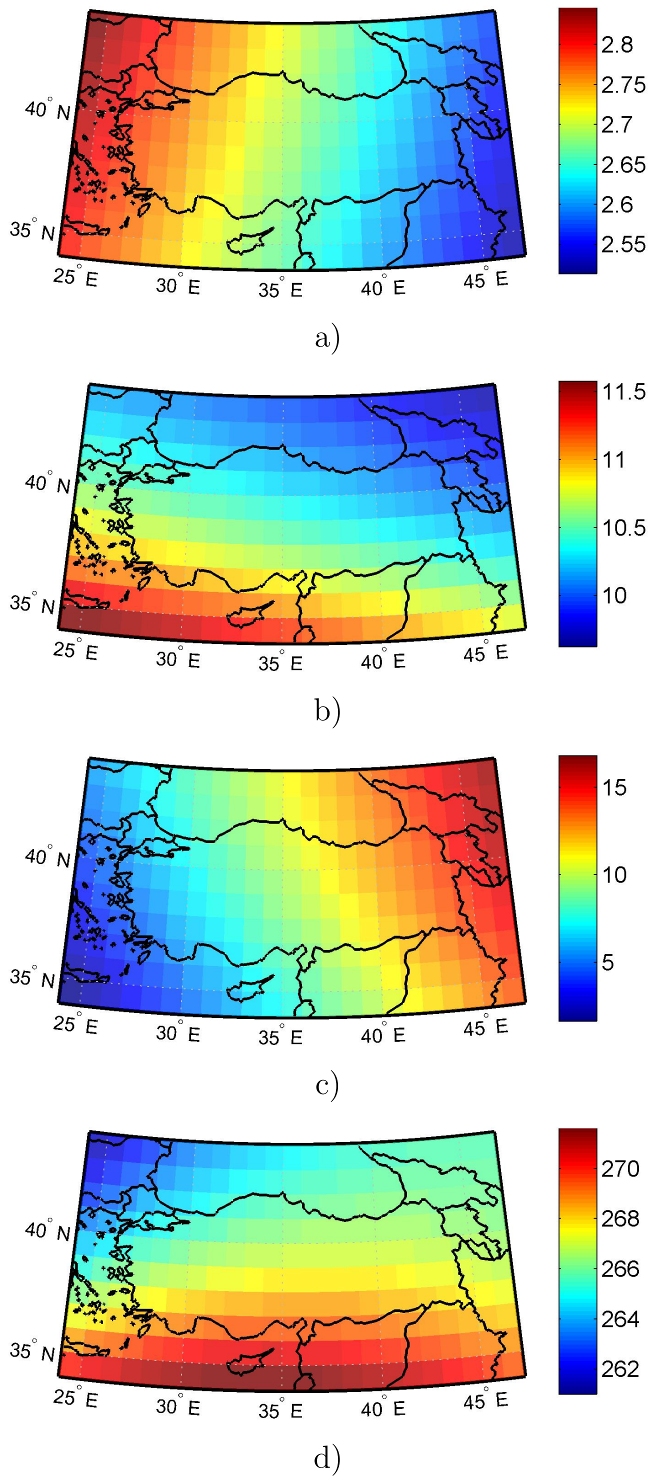

Figure 4.12: 10 March 2011, 12:00 GMT, a) optimized f_0F_2 perturbation surface (MHz), b) optimized f_0F_2 surface (MHz), c) optimized h_mF_2 perturbation surface (km), d) optimized h_mF_2 surface (km).

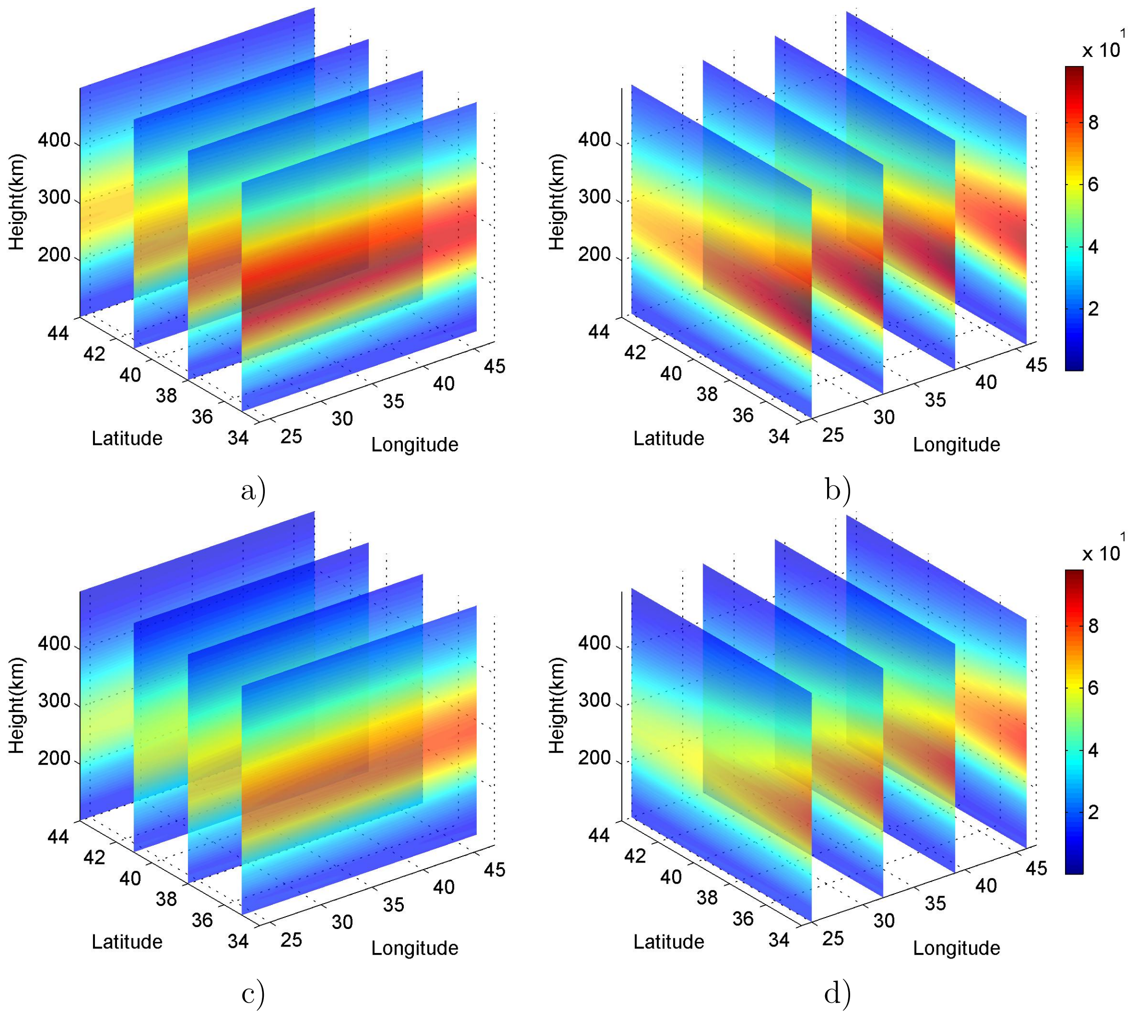

Figure 4.13: Electron density slices obtained by using IRI-Plas model and IONOLAB-CIT for 1 September 2011, 12:00 GMT, in terms of electrons / m^3. a) and b) show electron density slices obtained from IRI-Plas model for fixed latitudes (35° N, 38° N, 41° N, 44° N) and fixed longitudes (25° E, 32° E, 39° E, 46° E), respectively. c) and d) show electron density slices obtained by using IONOLAB-CIT for fixed latitudes (35° N, 38° N, 41° N, 44° N) and fixed longitudes (25° E, 32° E, 39° E, 46° E), respectively.

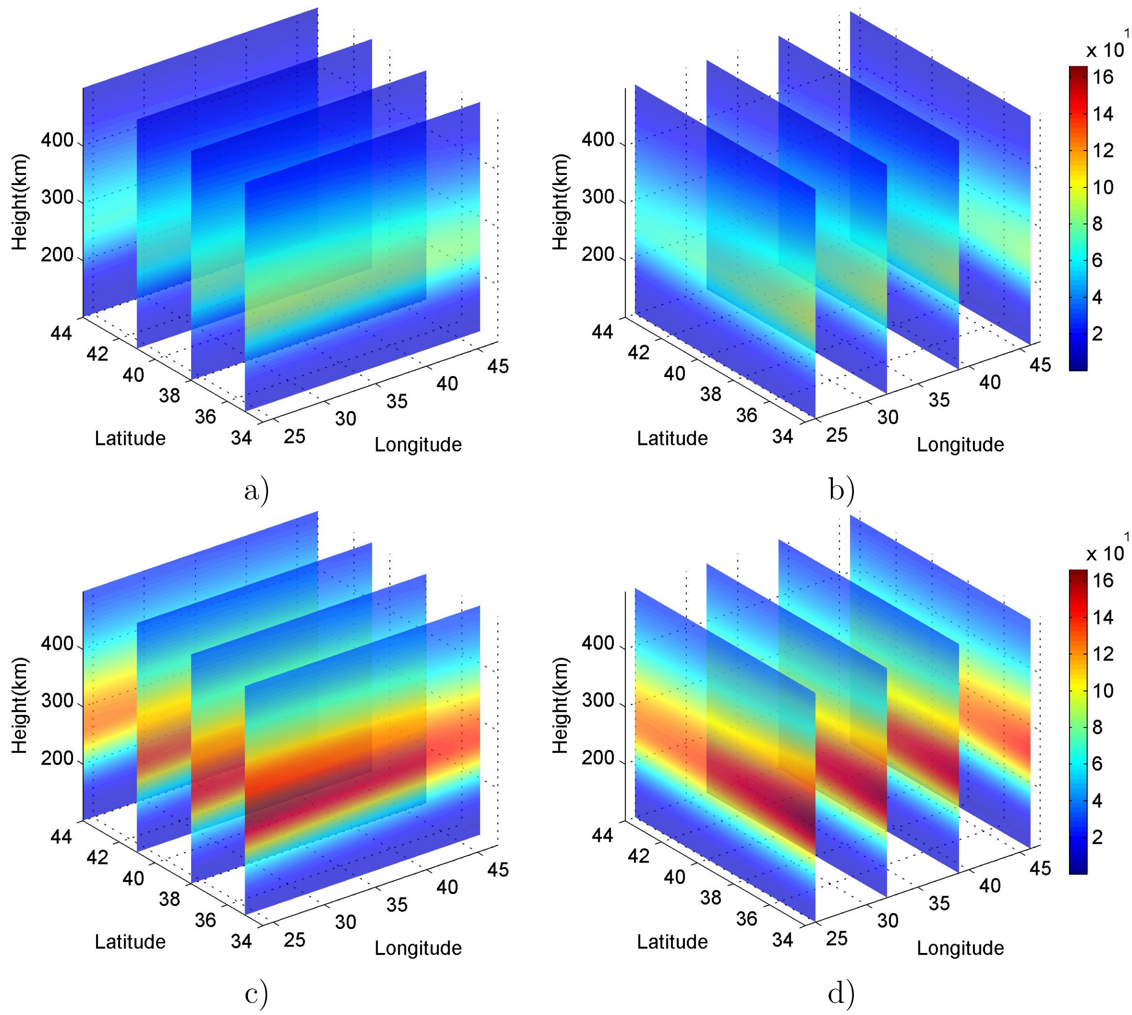

Figure 4.14: Electron density slices obtained by using IRI-Plas model and IONOLAB-CIT for 10 March 2011, 12:00 GMT, in terms of electrons / m^3. a) and b) show electron density slices obtained from IRI-Plas model for fixed latitudes (35° N, 38° N, 41° N, 44° N) and fixed longitudes (25° E, 32° E, 39° E, 46° E), respectively. c) and d) show electron density slices obtained by using IONOLAB-CIT for fixed latitudes (35° N, 38° N, 41° N, 44° N) and fixed longitudes (25° E, 32° E, 39° E, 46° E), respectively.

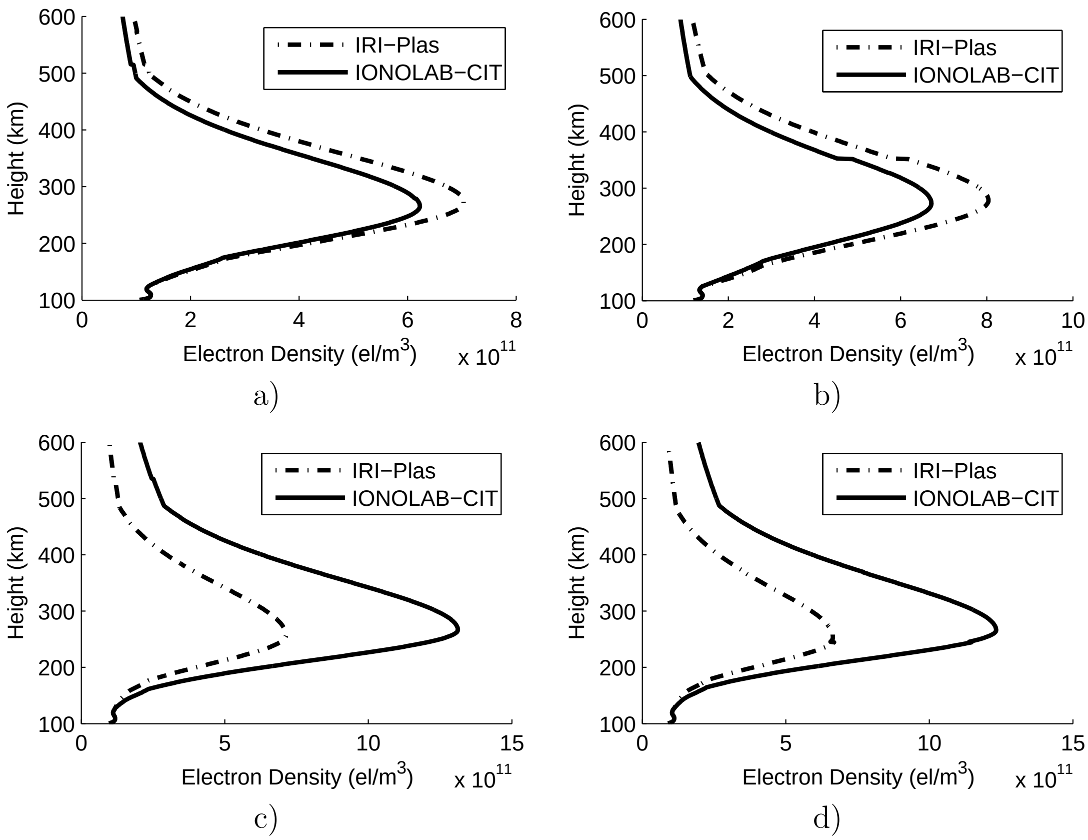

Figure 4.15: Electron density values along the GPS receiver - satellite path, obtained from the reconstructed 3D electron density distributions by using IRI-Plas model and IONOLAB-CIT. a) 1 September 2011, 12:00 GMT, receiver station: *ardh* [41.1° N, 42.7° E], GPS satellite PRN number: 29 (44.2° elevation, -82.9° azimuth), b) 1 September 2011, 12:00 GMT, receiver station: *cavd* [37.2° N, 29.7° E], GPS satellite PRN number: 30 (60.6° elevation, -36.5° azimuth), c) 10 March 2011, 12:00 GMT, receiver station: *kirs* [39.2° N, 34.2° E], GPS satellite PRN number: 23 (71.8° elevation, -23.0° azimuth), d) 10 March 2011, 12:00 GMT, receiver station: *trbn* [41.0° N, 39.7° E], GPS satellite PRN number: 23 (69.5° elevation, -50.9° azimuth).

Figures 4.16 and 4.17 show the difference between the measured GPS-STEC values and synthetically calculated STEC values from 3D electron density distributions obtained by the IRI-Plas model and the IONOLAB-CIT, on 1 September 2011, at 12:00 GMT and on 10 March 2011, at 12:00 GMT, respectively. The locations of colored dots represent the ionospheric pierce points at a shell height of 400 km corresponding to each measurement obtained from the TNPGN-Active receivers and used in the IONOLAB-CIT reconstruction. The red color indicates that the actual measurements are at least 5 percent greater than their corresponding synthetic calculations, the blue color indicates that the actual measurements are at least 5 percent smaller than their corresponding synthetic calculations, and the green color indicates that the difference between the actual and synthetic measurements are smaller than 5 percent of the actual measurements. The size of the dots represents the magnitude of difference between the actual measurements and their synthetic counterparts. In Figure 4.16a, it is observed that the actual measurements are much smaller than their synthetic counterparts calculated from the IRI-Plas model at 12:00 GMT on 1 September 2011, whereas in Figure 4.16b, it is observed that most of the synthetic measurements calculated from the IONOLAB-CIT are within 5% neighborhood of the actual measurements. It is also observed that the red and blue colored dots corresponding to positive and negative differences between the actual and synthetic measurements are very uniformly distributed among the map, which indicates a noise like structure for the residual error. In Figure 4.17a, it is observed that the actual measurements are much greater than their synthetic counterparts calculated from the IRI-Plas model at 12:00 GMT on 10 March 2011, whereas again in Figure 4.17b almost all of the synthetic measurements calculated from the IONOLAB-CIT are within 5% neighborhood of the actual measurements. Results show that the reconstructed 3D electron density distributions by the IONOLAB-CIT technique are in good agreement with the actual measurements.

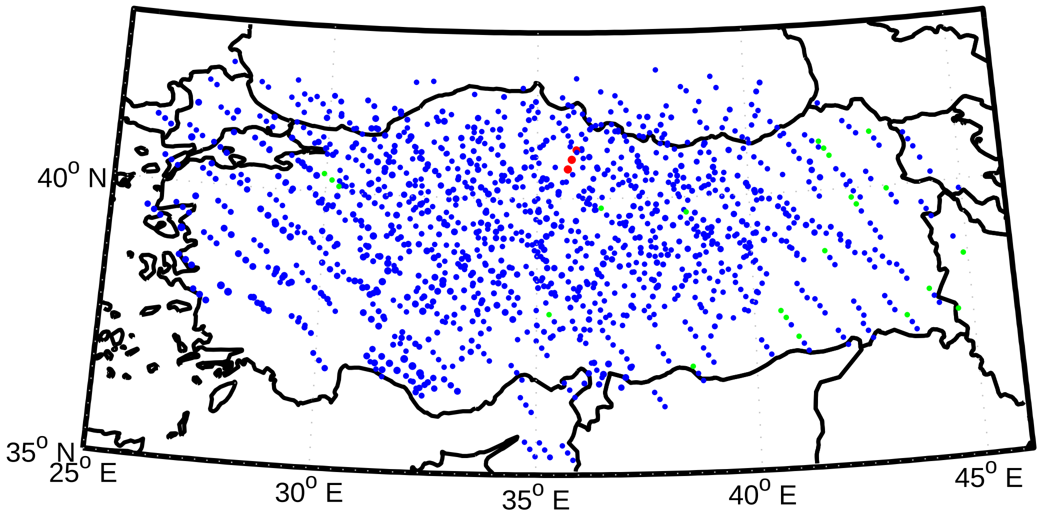

a)

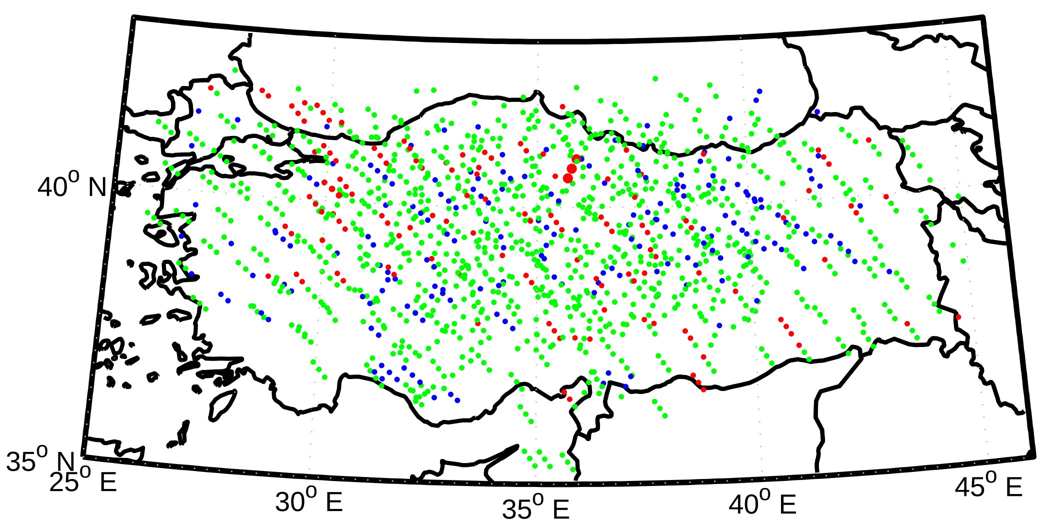

b)

Figure 4.16: The difference between the measured GPS-STEC values and synthetically calculated STEC values from 3D electron density distributions obtained by a) IRI-Plas, b) IONOLAB-CIT, on 1 September 2011, at 12:00 GMT. Red dots mean that the real measurements are at least 5 percent greater than synthetic calculations, blue dots mean that the real measurements are at least 5 percent smaller than synthetic calculations, and green dots mean that the difference between the real measurements and the synthetic calculations are smaller than 5 percent.

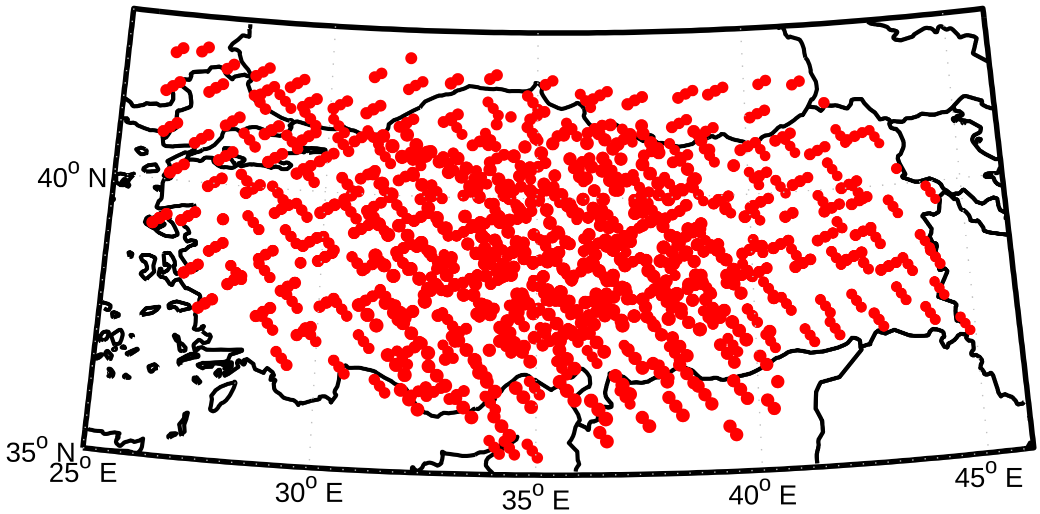

a)

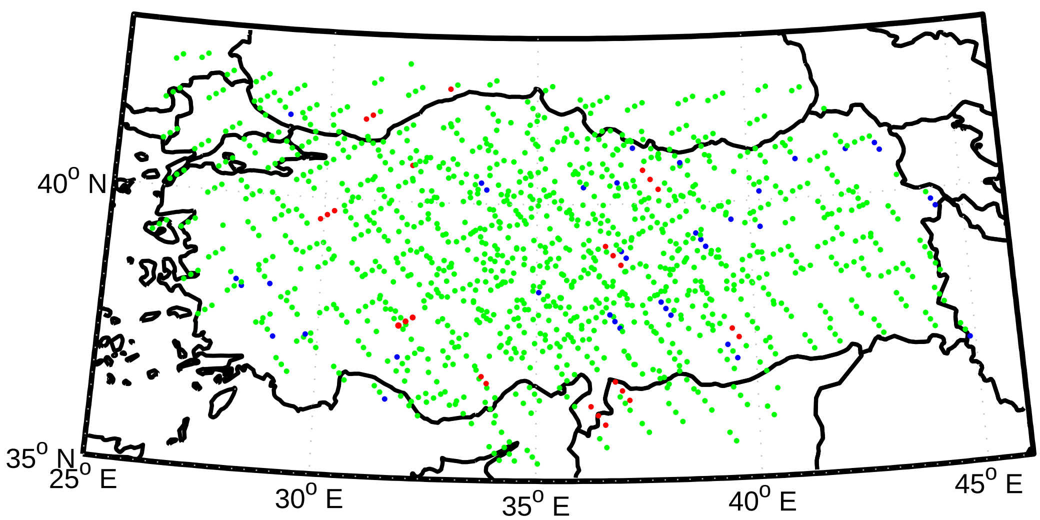

b)

Figure 4.17: The difference between the measured GPS-STEC values and synthetically calculated STEC values from 3D electron density distributions obtained by a) IRI-Plas, b) IONOLAB-CIT, on 10 March 2011, at 12:00 GMT. Red dots mean that the real measurements are at least 5 percent greater than synthetic calculations, blue dots mean that the real measurements are at least 5 percent smaller than synthetic calculations, and green dots mean that the difference between the real measurements and the synthetic calculations are smaller than 5 percent.

Table 4.2: Cost function obtained after 100 iterations for each method for different dates.

Date	Ionospheric weather	IRI-Plas	GD	BFGS	PSO
21.03.2011, 10:30 GMT	Non-disturbed	0.14655	0.04712	0.04712	0.04951
21.03.2011, 23:00 GMT	Non-disturbed	0.15180	0.07742	0.07742	0.07804
12.06.2011, 06:15 GMT	Non-disturbed	0.21583	0.04078	0.04078	0.04410
12.06.2011, 17:45 GMT	Non-disturbed	0.05706	0.04650	0.04650	0.04776
21.09.2011, 03:30 GMT	Non-disturbed	0.15304	0.08569	0.08569	0.09131
21.09.2011, 13:45 GMT	Non-disturbed	0.18615	0.02432	0.02431	0.02865
25.12.2011, 06:00 GMT	Non-disturbed	0.08900	0.03632	0.03631	0.03662
25.12.2011, 16:30 GMT	Non-disturbed	0.09381	0.05263	0.05263	0.05988
05.02.2011, 01:00 GMT	Disturbed	0.24884	0.06154	0.06154	0.06783
28.05.2011, 12:15 GMT	Disturbed	0.29944	0.02833	0.02833	0.03378
06.08.2011, 00:30 GMT	Disturbed	0.12046	0.08599	0.08599	0.08735
01.11.2011, 15:30 GMT	Disturbed	0.24716	0.03593	0.03592	0.03671

Third, the IONOLAB-CIT is experimented on the real measurement data (IONOLAB-STEC) for different dates and ionospheric weather, and the performance of each optimization method are listed in Table 4.2. The ionospheric weather indices for the listed days can be found in Appendix A. Results show that the performance of three methods are similar in most scenarios. However, in all cases, the BFGS outperforms others. Small values for cost functions obtained after using optimization methods can be attributed to the measurement noise in the TEC measurements. If the cost function is very high that it can not be explained by the measurement errors, this may indicate the necessity to use a higher order parametric perturbation surface or failure of the ionosphere model to model the ionospheric electron density adequately for that case.

Fourth, to investigate the reliability of the reconstructions, the data obtained at two GPS receiver stations located in Ankara and Malatya are excluded from the measurement set input to the reconstruction algorithm. The proposed CIT technique is run with the remaining STEC measurements for days of 1 September 2011 and 10 March 2011, both at 12:00 GMT, by using the BFGS optimization

Table 4.3: Comparison of the measured STEC values, STEC values calculated from the IRI-Plas model and the predicted STEC values calculated from the optimized 3D electron density distributions for 1 September 2011, 12:00 GMT.

Receiver Station	Receiver Location	GPS Satellite PRN	Elevation Angle	Azimuth Angle	Measured STEC	IRI-Plas STEC	Predicted STEC
Ankara, 'anrk'	39.9° N, 32.8° E	2	50°	63°	26.05	30.57	26.37
Ankara, 'anrk'	39.9° N, 32.8° E	12	65°	93°	25.79	28.12	24.28
Ankara, 'anrk'	39.9° N, 32.8° E	25	70°	-30°	23.11	26.94	22.56
Ankara, 'anrk'	39.9° N, 32.8° E	30	64°	-43°	22.30	28.02	23.33
Malatya, 'maly'	38.3° N, 38.2° E	12	71°	92°	26.47	28.36	25.32
Malatya, 'maly'	38.3° N, 38.2° E	25	66°	-35°	24.74	28.12	24.36
Malatya, 'maly'	38.3° N, 38.2° E	29	46°	-84°	31.33	35.13	30.00
Malatya, 'maly'	38.3° N, 38.2° E	30	56°	-44°	25.13	30.01	25.73

method. Then, the missing STEC measurements at the two left out stations are computed from the reconstructions, and compared with the actual STEC measurements obtained from these stations. Tables 4.4 and 4.3 show the comparison between the measured and the reconstructed STEC values. The results show that the missing STEC measurements are closely predicted by using the 3D reconstructions obtained by the IONOLAB-CIT technique, which indicates that the IONOLAB-CIT technique provides reliable reconstructions.

Fifth, in order to investigate the relation between the IONOLAB-CIT performance and the number of GPS receiver stations, new experiments are carried out by using fewer number of GPS receiver stations. IONOLAB-CIT technique is run on measurements obtained from a selected GPS receiver station set, then by using the resultant 3D electron density distribution, the cost function is calculated by using all of the available measurements. In these experiments, results obtained by using 3 and 7 GPS receiver stations are compared with the results obtained by using all of the GPS receiver stations. The experiments are carried out for 24 hours with 15 minute intervals for a calm day (1 September 2011) and

Table 4.4: Comparison of the measured STEC values, STEC values calculated from the IRI-Plas model and the predicted STEC values calculated from the optimized 3D electron density distributions for 10 March 2011, 12:00 GMT.

Receiver Station	Receiver Location	GPS Satellite PRN	Elevation Angle	Azimuth Angle	Measured STEC	IRI-Plas STEC	Predicted STEC
Ankara, 'anrk'	39.9° N, 32.8° E	20	75°	94°	43.23	24.54	43.08
Ankara, 'anrk'	39.9° N, 32.8° E	23	73°	-29°	45.57	24.60	43.29
Ankara, 'anrk'	39.9° N, 32.8° E	32	46°	103°	58.41	30.75	54.14
Malatya, 'maly'	38.3° N, 38.2° E	13	44°	-84°	56.75	33.16	57.61
Malatya, 'maly'	38.3° N, 38.2° E	20	81°	89°	41.79	24.61	42.59
Malatya, 'maly'	38.3° N, 38.2° E	23	69°	-36°	44.31	25.26	44.09

a stormy day (10 March 2011). When using all of the receiver stations, 90-136 receivers provided valid measurements during any time instant on 1 September 2011, 109-143 receivers provided valid measurements during any time instant on 10 March 2011. When using 3 or 7 receiver stations, receiver stations are selected among the ones which are almost uniformly spread over the region of interest, and which provide valid measurements during all day. Figures 4.18a, b show the selected GPS receiver stations on the map, for 3 and 7 GPS receiver station experiments, respectively. In 3 GPS receiver station experiments, the TNPGN-Active stations *feth*, *anrk* and *mard* are used. In 7 GPS receiver station experiments, the TNPGN-Active stations *feth*, *anrk*, *mard*, *istn*, *hata*, *samn* and *agrd* are used. Figures 4.19a,b show the cost values obtained by using 3, 7 and all of the stations, together with the corresponding cost of default IRI-Plas model reconstructions. Results show that using 7 GPS receiver stations for both calm and stormy days gives similar performance to using all of the GPS receiver stations available. However, when the GPS receiver station number is decreased to 3, IONOLAB-CIT may fail to perform as good in some of the scenarios. On 1 September 2011, at 08:30 GMT and at 20:45 GMT, using 3 GPS receiver stations in the IONOLAB-CIT produces significantly larger cost values than using all of

Table 4.5: Average number of iterations for convergence in BFGS optimization method with respect to the number of GPS receiver stations used in the reconstructions.

	3 stations	7 stations	All stations
1 September 2011	32.50	29.82	28.13
10 March 2011	33.11	31.70	28.06

the available GPS receiver stations. These sudden performance drops happen especially when there are significant errors in the measurements which bypasses the filters used in the measurement set formation, and the satellite transitions where new satellites become available while the previous satellites leave the receiver line of sight. On 10 March 2011, between 00:15 and 07:00 GMT, using 3 GPS receiver stations in the IONOLAB-CIT again produces significantly larger cost values than using all of the available GPS receiver stations. This result can be related to the fact that the spatial correlation of the ionosphere decreases on stormy days, and the lower number of receiver stations increases the sensitivity of the IONOLAB-CIT to the disturbances in the ionosphere. In conclusion, for a mid-latitude region like Turkey, 7 GPS receiver stations are sufficient for both calm and stormy days to obtain good results with the IONOLAB-CIT technique. Using fewer GPS receiver stations may produce acceptable results if there are no significant errors in the satellite measurements and the ionosphere is calm.

The average number of iterations for convergence is also investigated with respect to number of stations used in reconstructions. Table 4.5 shows average number of iterations for convergence in BFGS optimization method when using 3, 7 or all GPS receiver stations in reconstructions on 1 September 2011 and on 10 March 2011. Results show that the convergence rate for all cases are similar. The slight increase in the iteration number for convergence when using lower number of stations can be related with the fact that the solution can diverge from the default IRI-Plas model solution more significantly when using lower number of stations, because lower number of stations increases the sensitivity of the IONOLAB-CIT to measurement errors.

Sixth, to provide further verification on the performance of the proposed

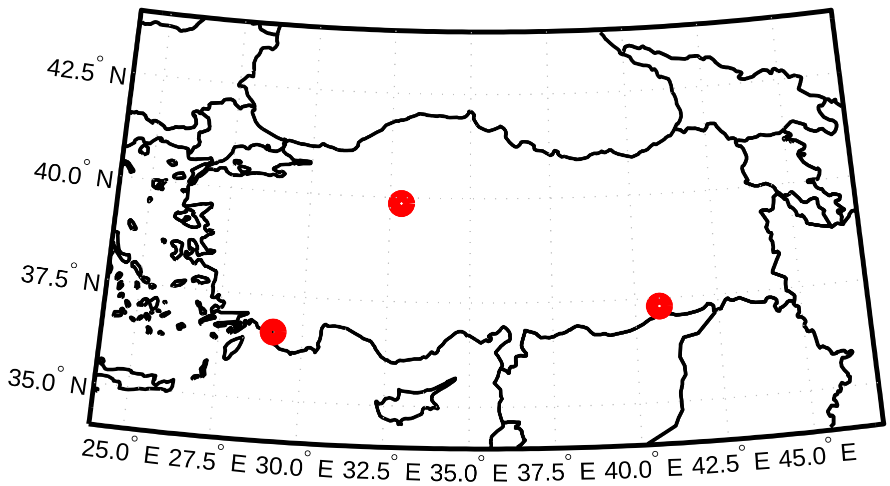

a)

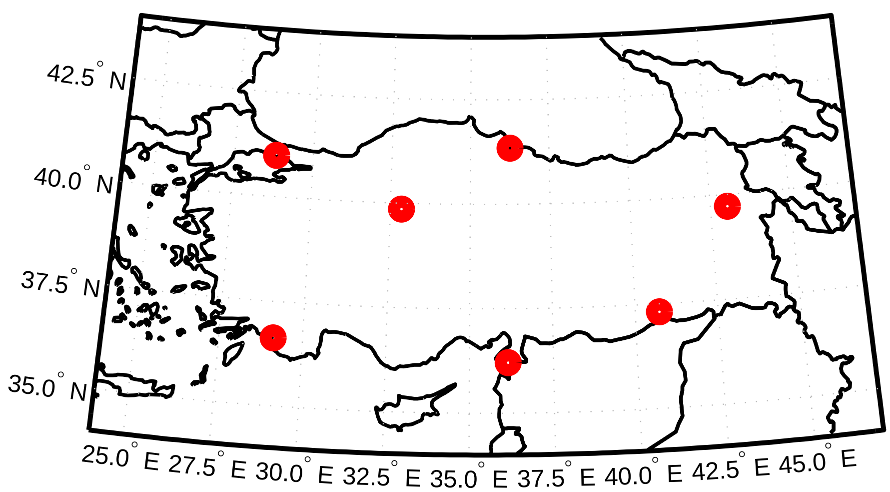

b)

Figure 4.18: Utilized GPS receiver stations in a) 3 GPS receiver station experiments, b) 7 GPS receiver station experiments.

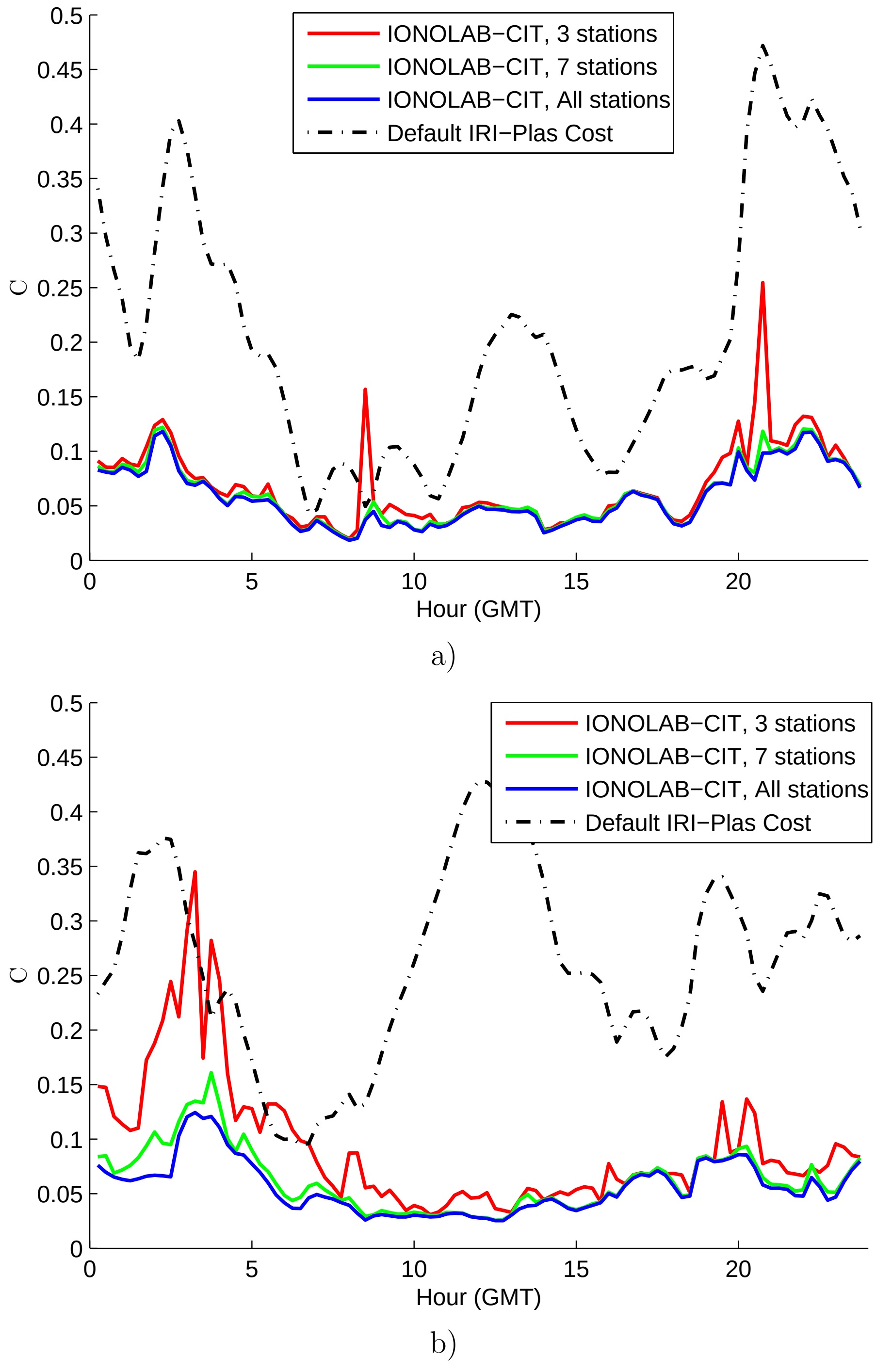

Figure 4.19: Comparison of the cost values obtained by the IONOLAB-CIT technique, with respect to the utilized GPS receiver station number, on a) calm day (1 September 2011), b) stormy day (10 March 2011).

IONOLAB-CIT technique, the IONOLAB-CIT results are compared with the ionosonde measurements. Unfortunately, there are no ionosonde measurements available over Turkey for comparison. The nearest ionosonde station to Turkey is located at Athens [38.0° N, 23.5° E]. In order to compare Athens ionosonde measurements with the IONOLAB-CIT results, the reconstruction region of the IONOLAB-CIT is shifted to the West without changing the size of the region. The limits of the region for estimating the 3D electron density distribution is selected in between 34° N and 44° N latitudes, 19° E and 42° E longitudes, and 100 and 20,000 km in height. Figure 4.20 shows the region and the GPS receiver stations used in the IONOLAB-CIT technique. In order to use the IONOLAB-CIT technique over this region, IGS stations in Greece (*aut1*, *duth*, *larm*, *noa1*, *pat0*, *tuc2*), and Macedonia (*orid*), and TNPGN-Active stations in Turkey (*afyn*, *anrk*, *ante*, *antl*, *bing*, *istn*, *izmi*, *lefk*, *nigd*, *samn*, and *sivs*) are used. Figures 4.21a, b show the comparison of plasma frequencies with respect to height provided by the IRI-Plas model and the IONOLAB-CIT technique, with the plasma frequencies obtained by using the ionosonde measurements and the two widely used automatic ionogram scaling techniques ARTIST [75] and POLAN [76], for calm and stormy days, respectively. The BFGS optimization technique is used in both IONOLAB-CIT results. The ionosonde measurement data is obtained from `http://ngdc.noaa.gov/ionosonde/data/`. Results show that the IONOLAB-CIT provides closer results to the ionosonde measurements with respect to the IRI-Plas model.

The IONOLAB-CIT technique conducts a search for the optimal parameters for the reconstruction of the 3D electron density distribution for the given GPS-STEC measurement set by using iterative optimization approaches. All of the conducted experiments show significant increase in the compliance between the actual and synthetic measurements obtained from the reconstructed 3D electron density distributions. Three different optimization methods are investigated in the experiments, and BFGS method is shown to be the optimum choice to be used in the IONOLAB-CIT problem for the selected optimization parameter set.

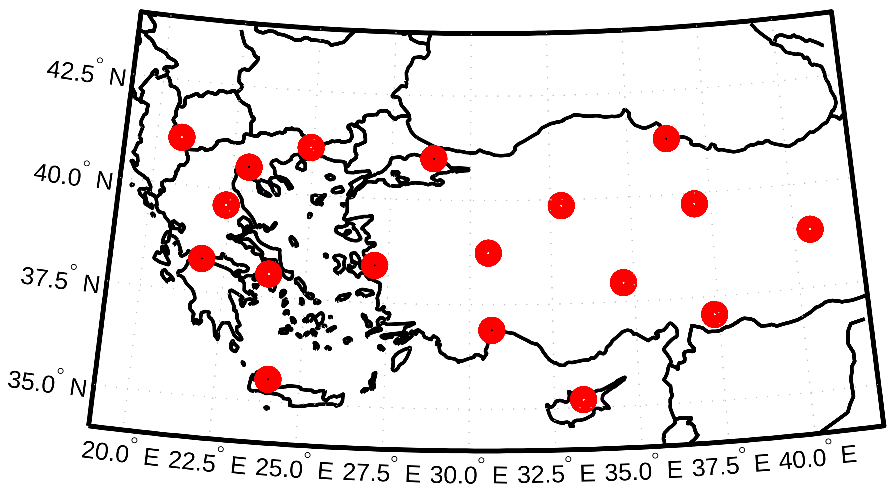

Figure 4.20: The region of reconstruction used in the IONOLAB-CIT technique for ionosonde comparison experiment and utilized GPS receiver stations.

4.7 Conclusion

A new approach, namely IONOLAB-CIT, is presented for estimation of 3D electron density distribution in the ionosphere by using GPS-STEC measurements and the IRI-Plas model. The IRI-Plas input parameters f_0F_2 and h_mF_2 are adjusted by using additive parametric perturbation surfaces, such that the synthetic STEC measurements calculated from the resultant 3D electron density distribution is in compliance with the real GPS-STEC measurements obtained from a GPS receiver network. The surface parameters are optimized by using gradient descent, BFGS and PSO methods. 3D electron density distributions over Turkey are generated by using the real GPS-STEC measurement data obtained from TNPGN-Active stations. Results show that the reconstructed 3D electron density distributions have significantly improved conformity with the measurements, with respect to the default 3D electron density distributions obtained from the IRI-Plas model. Reconstructions are also validated by predicting the STEC measurements that are left out in the reconstruction phase. IONOLAB-CIT is run over Greece and Western Turkey and the obtained results are compared with the ionosonde measurements in Athens. It is shown that the IONOLAB-CIT is in better agreement with the ionosonde measurements with respect to the IRI-Plas

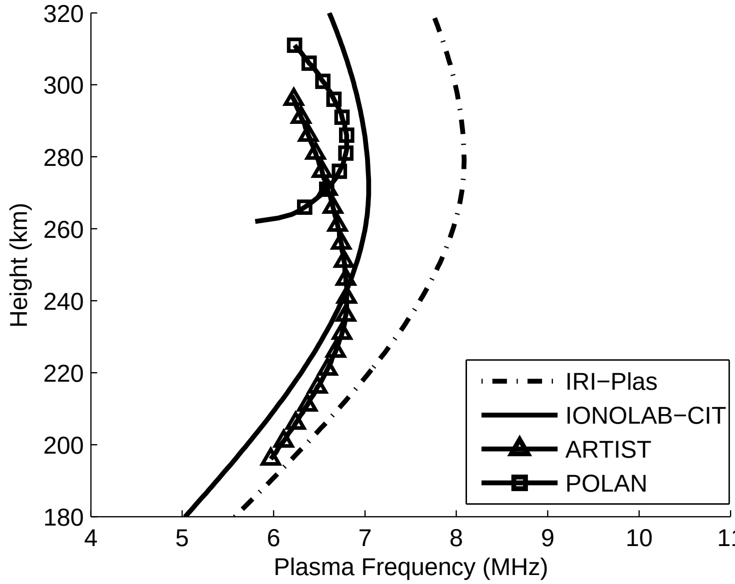

a)

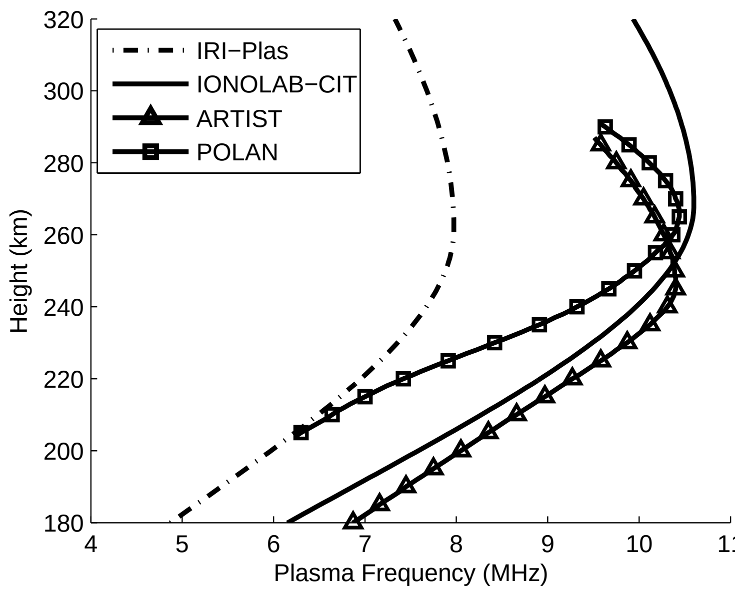

b)

Figure 4.21: Comparison of the plasma frequencies obtained by using the IRI-Plas model and the proposed IONOLAB-CIT technique, with the plasma frequencies obtained by using ionosonde measurements and two automatic ionogram scaling techniques ARTIST and POLAN, at Athens [38.0° N, 23.5° E], on a) calm day (1 September 2011, 12:00 GMT), b) stormy day (10 March 2011, 12:00 GMT).

model. The proposed approach can be easily extended to operate over a larger set of parameters if necessary. Ionospheric measurements like ionosonde measurements, GPS occultation measurements can be added to the IONOLAB-CIT technique by modifying the cost function accordingly.

Chapter 5

4-D CIT: Reconstructions in Space - Time

5.1 Introduction

The electron density distribution in the ionosphere has a spatially and temporally varying structure. Due to the global nature of the main processes governing the ionization processes, electron density distribution in the ionosphere is highly correlated in space and time. For mid-latitude ionosphere, it has been observed that the temporal correlation or wide sense stationarity period can vary from 15 to 20 minutes for calm days of the ionosphere, and from 3 to 25 minutes for disturbed days of the ionosphere [77]. To provide more robust results, the model based reconstructions should exploit the temporal continuity in the physical structure of the ionosphere [42].

Classical approaches proposed for imaging the ionospheric electron density distribution take advantage of the smooth time-varying structure of the ionosphere. TEC measurements obtained between a Low Earth Orbit (LEO) satellite and an array of receiver stations are used in these CIT techniques. Measurements obtained at multiple time instants during a satellite pass are used for imaging a vertical slice of the electron density distribution. Since there is a significant time difference between the measurements, these methods assume ionosphere to be invariant during the duration of a satellite pass [1], [2], [3].

GPS-STEC measurements obtained from all possible pairs of multiple satellites and receiver stations can give a snapshot of the ionosphere. CIT techniques utilizing GPS-STEC measurements in the literature are generally described at a fixed time, and they handle the problem independently for each time instant resulting in reduced performance [12], [13], [18]. However, the ionosphere is highly correlated in time and GPS-STEC measurements have significant information about the past and future states of the ionosphere. In order to accommodate the temporal changes in the ionosphere, Kalman filtering approach is used in various approaches [61], [78], [79], [80], [81]. Electron density values in voxels are tracked in time by using Kalman filtering method in [78]. The coefficients of the empirical orthogonal functions (EOFs) forming the perturbation values onto the default electron density values obtained from ionosphere models are tracked by using Kalman filtering method in [61]. Kalman filtering is used in data assimilation approaches by linearization of physical models describing ionospheric parameters [79], [80]. Some methods using iterative approaches for 3D imaging of the ionosphere used previous results via a Kalman filtering approach for projecting the previous results forward in time for initializing the next analysis [81]. A time-dependent algorithm for ionospheric imaging has also been proposed without using Kalman filtering techniques where electron density values are allowed to change linearly over time [82].

In this chapter, the IONOLAB-CIT technique which is proposed in Chapter 4 for 3D imaging of the ionospheric electron density distribution is extended to exploit the temporal structure of the ionosphere. Instead of tracking the ionospheric electron density distribution directly, IONOLAB-CIT results, which correspond to the parameters of the perturbation surfaces onto the ionospheric parameters f_0F_2 and h_mF_2, are tracked and smoothed in time by using Kalman filtering techniques. Following sections contain the progressive development process of the 4D IONOLAB-CIT technique. First, the relation between the sun zenith angle and the ionospheric electron density is investigated by using the

IRI-Plas model. Second, in order to investigate the temporal correlation among the IONOLAB-CIT results, the IONOLAB-CIT technique is applied on two sets of calm and stormy days, providing reconstructions at every 15 minutes for the whole day. As expected, results of the experiments have indicated high temporal correlation. Next, possible state transition models for the IONOLAB-CIT results are proposed for estimating the temporal relation between consecutive states of the ionosphere and the temporal validity of these estimations are examined for increasingly larger time intervals. Finally, Kalman based tracking/smoothing methods are implemented for tracking/smoothing the IONOLAB-CIT results in time domain, for both obtaining more robust solutions and decreasing the computational cost of the IONOLAB-CIT technique. Results showed that Kalman based tracking/smoothing techniques produce more robust reconstructions especially when the data of few GPS receivers are used in the reconstructions.

5.2 The Relation Between the Solar Zenith Angle and the Ionospheric Electron Density

The major factor of ionization in the ionosphere is the solar radiation. Therefore solar zenith angle is one of the most important parameters for modelling the ionospheric electron density distribution. In this thesis, the relationship between the solar zenith angle and the ionospheric electron density are investigated by using the IRI-Plas model. The geodetic coordinates are transformed into a new coordinate system which has the reference point (0° Latitude, 0° Longitude) as the point where the sun zenith angle is zero. As the earth rotates, this new coordinate system also rotates with respect to the geodetic coordinate system, such that every fixed location in this new coordinate system has a fixed local zenith angle. It is expected that the ionospheric electron density distribution to remain statistically stationary with respect to time for a fixed point in the new coordinate system, while it changes rapidly for a fixed point in geodetic coordinate system. Some of the proposed CIT methods in the literature have used this sun-fixed coordinate system for making use of the solar dominance on the ionospheric

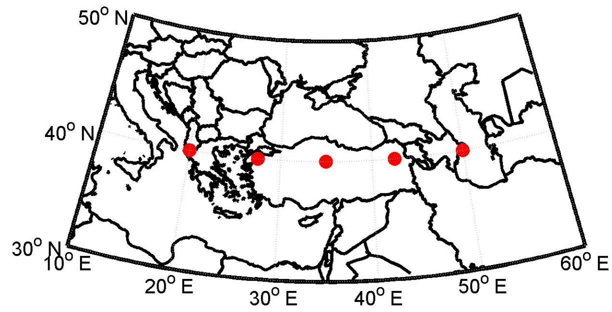

a)

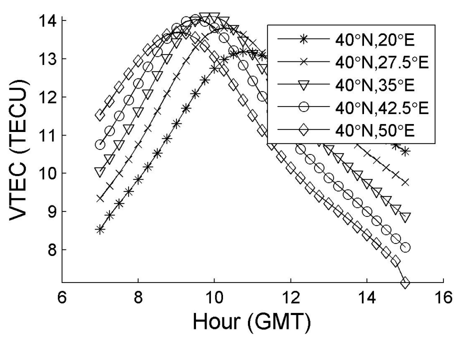

b)

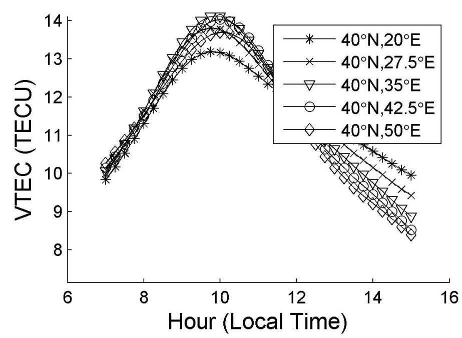

c)

Figure 5.1: Comparison of the VTEC values in global time and local time on 21 March 2009. a) Selected receiver station locations, b) VTEC values in global time, c) VTEC values in local time.

electron density [61], [83], whereas others used the geodetic coordinate system, because of the fact that ionospheric disturbances do not simply follow the sun zenith angle [82]. In order to investigate the effect of the solar zenith angle in the IRI-Plas, VTEC values at selected locations on fixed latitudes are calculated from the IRI-Plas model for three different days and three different latitudes, and plotted with respect to the fixed local and fixed global times. Since points on a fixed latitude with the same local time corresponds to the same coordinates in the sun-fixed coordinate system, VTEC values are expected to align better in local time. Figures 5.1, 5.2 and 5.3 show how the ionosphere changes at the receiver locations in local time and global time.

Figures 5.1, 5.2 and 5.3 show that temporal correlation of ionospheric electron density values are higher when the reference coordinate system is selected as the

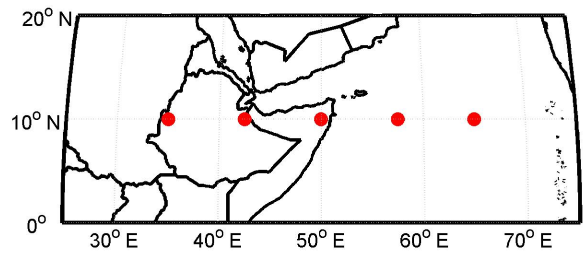

a)

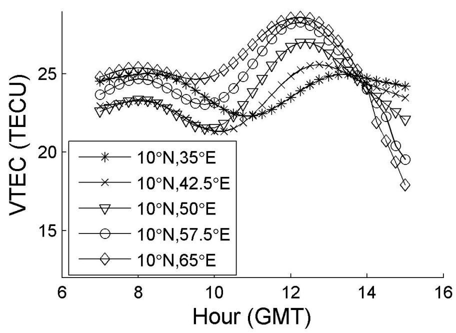

b)

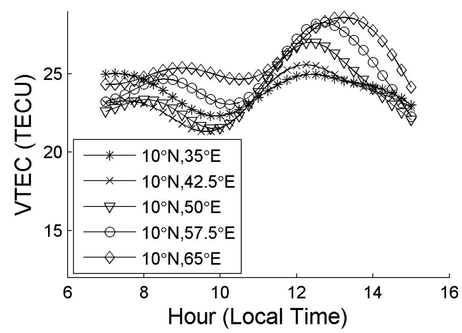

c)

Figure 5.2: Comparison of the VTEC values in global time and local time on 21 June 2009. a) Selected receiver station locations, b) VTEC values in global time, c) VTEC values in local time.

sun-fixed coordinate system rather than the geodetic coordinate system. This result supports that the electron density values are strongly correlated with the solar zenith angle. The important question is whether the perturbation surface parameters found by the IONOLAB-CIT are strongly correlated in time in a similar way. Following sections examine temporal characteristics of the IONOLAB-CIT results to find an answer to this question.

5.3 Temporal Analysis of CIT Results

In Chapter 4, the IONOLAB-CIT is proposed for estimating the 3D electron density distribution of the ionosphere by using a set of geographically distributed

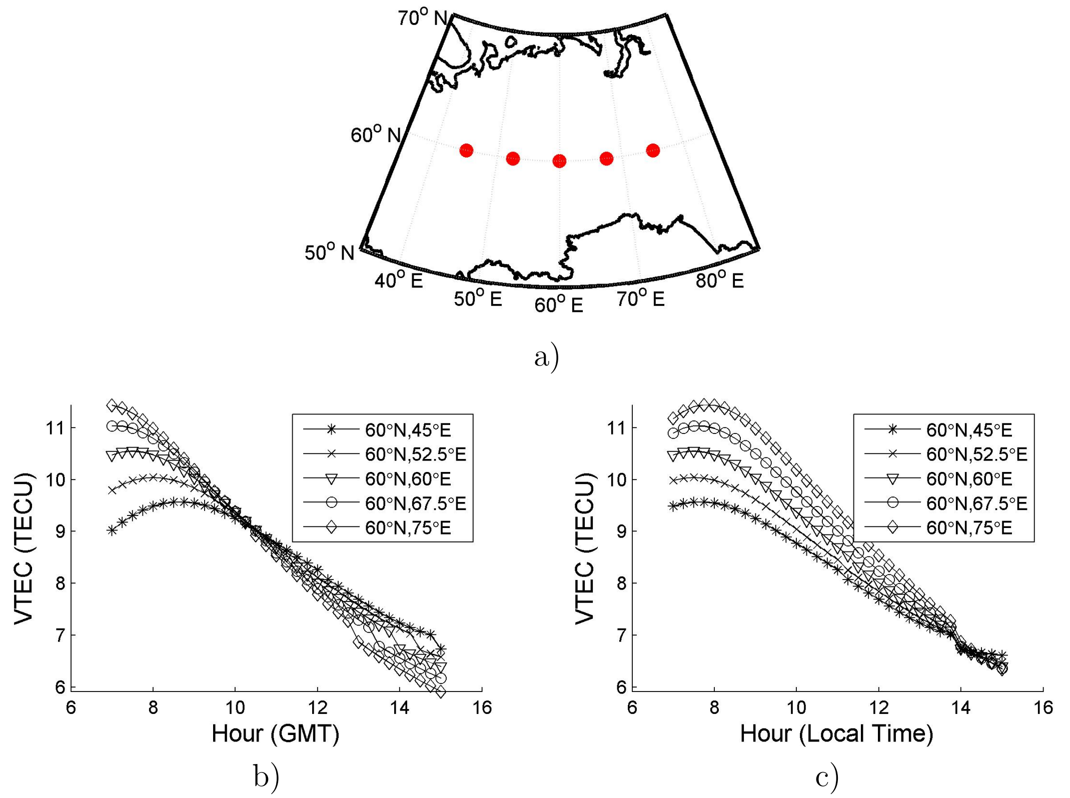

Figure 5.3: Comparison of the VTEC values in global time and local time on 21 September 2009. a) Selected receiver station locations, b) VTEC values in global time, c) VTEC values in local time.

GPS measurements and the IRI-Plas model. The results showed significant improvement in the compliance between the IRI-Plas model and the actual GPS measurements. In this section, temporal variation of the solution parameters found by using the IONOLAB-CIT is investigated. The following set of calm and solar active days are chosen for this investigation:

- 10 March 2011 (stormy day),
- 28 May 2011 (stormy day),
- 12 June 2011 (calm day),
- 1 September 2011 (calm day).

The reconstructions of the IONOLAB-CIT technique corresponding to these days generated the perturbation surface parameters that minimizes the cost function given in (4.17). Figures 5.4, 5.5, 5.6, and 5.7 show the cost functions obtained by using the IRI-Plas and the IONOLAB-CIT and the corresponding perturbation surface parameters for 15 minute time intervals. Independent runs of the IONOLAB-CIT on both calm and stormy days show that the perturbation surface parameters are highly correlated in time. It is also observed that the temporal correlation of f_0F_2 perturbation surface parameters are more significant than the temporal correlation of h_mF_2 perturbation surface parameters. This result can be utilized in two ways:

- First, the perturbation surface parameters obtained from previous measurements can be utilized in a way to decrease the computation cost.
- Second, the perturbation surface parameters can be tracked or even smoothed out in time for obtaining more robust results.

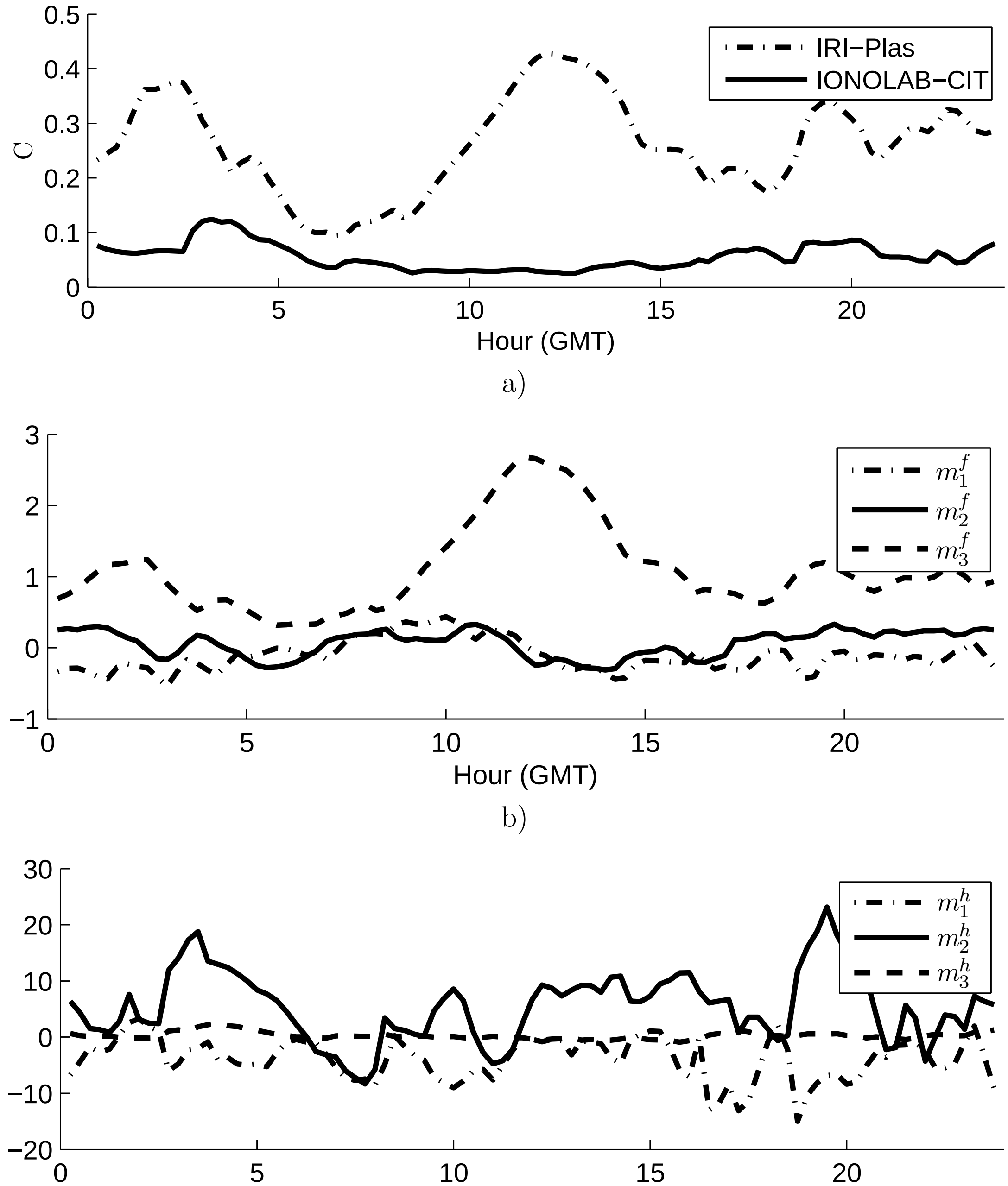

Figure 5.4: Results obtained by the IONOLAB-CIT technique on 10 March 2011. a) Comparison of cost functions obtained by IRI-Plas and IONOLAB-CIT, b) Perturbation surface parameters on f_0F_2 parameter, c) Perturbation surface parameters on h_mF_2 parameter.

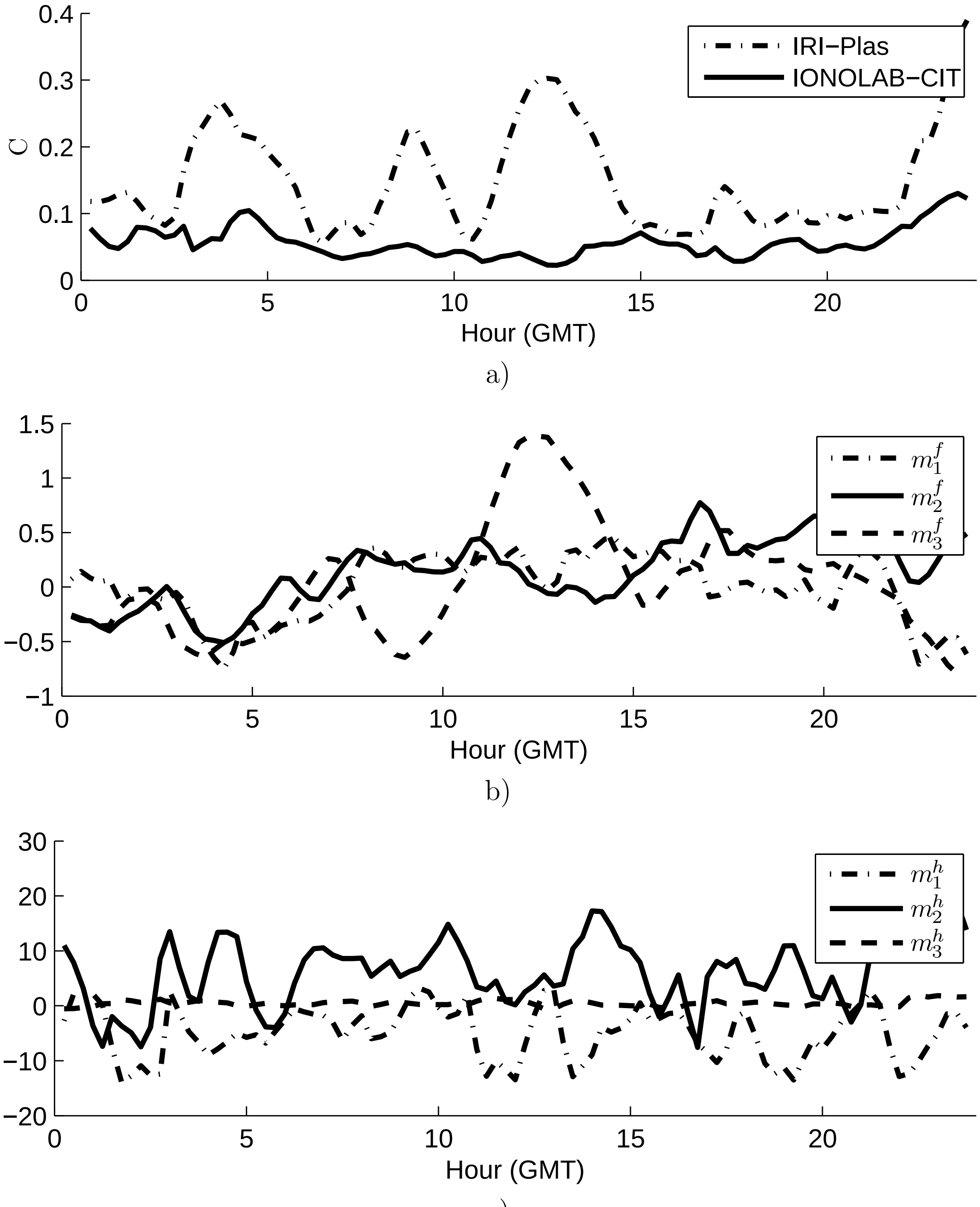

a)

b)

c)

Figure 5.5: Results obtained by the IONOLAB-CIT technique on 28 May 2011. a) Comparison of cost functions obtained by IRI-Plas and IONOLAB-CIT, b) Perturbation surface parameters on f_0F_2 parameter, c) Perturbation surface parameters on h_mF_2 parameter.

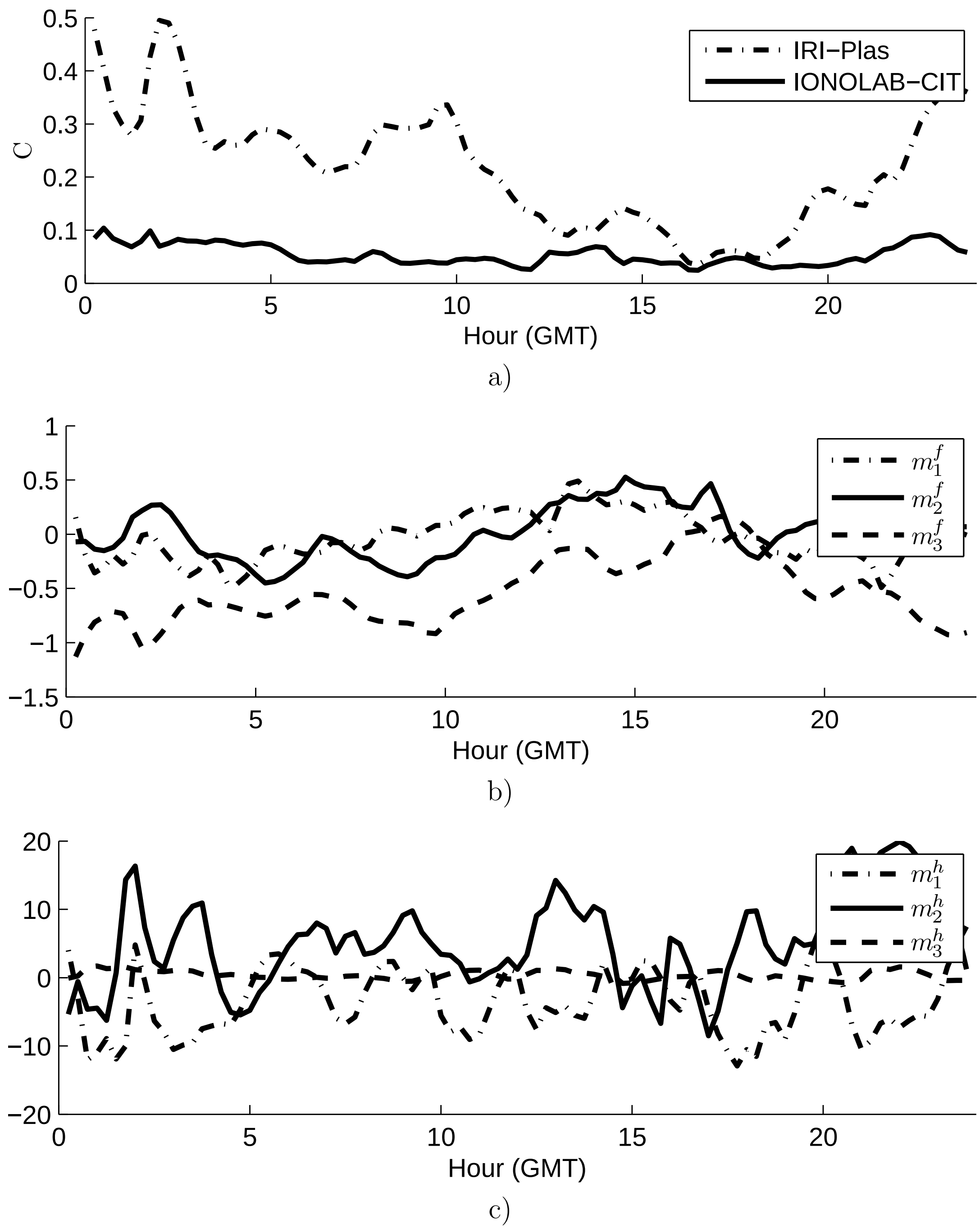

Figure 5.6: Results obtained by the IONOLAB-CIT technique on 12 June 2011. a) Comparison of cost functions obtained by IRI-Plas and IONOLAB-CIT, b) Perturbation surface parameters on f_0F_2 parameter, c) Perturbation surface parameters on h_mF_2 parameter.

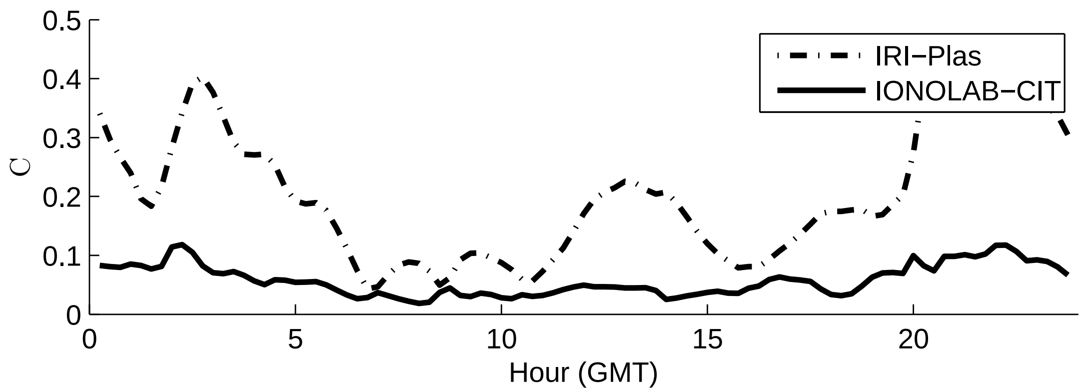

a)

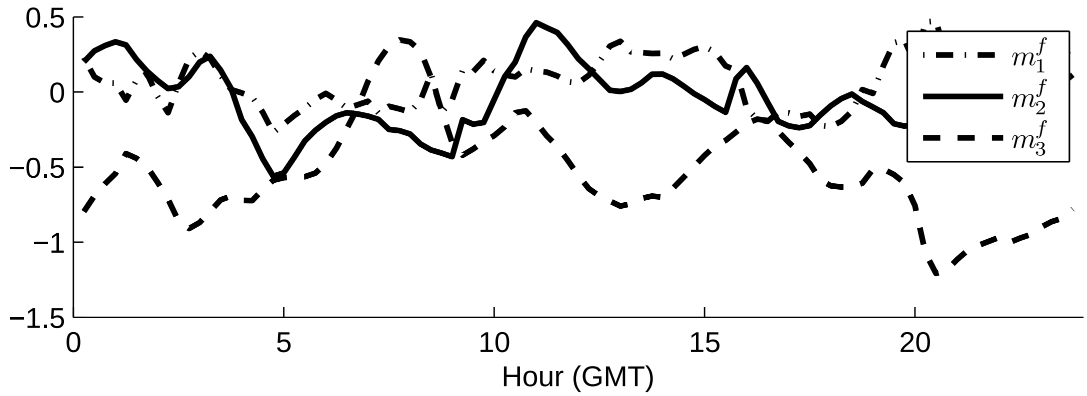

b)

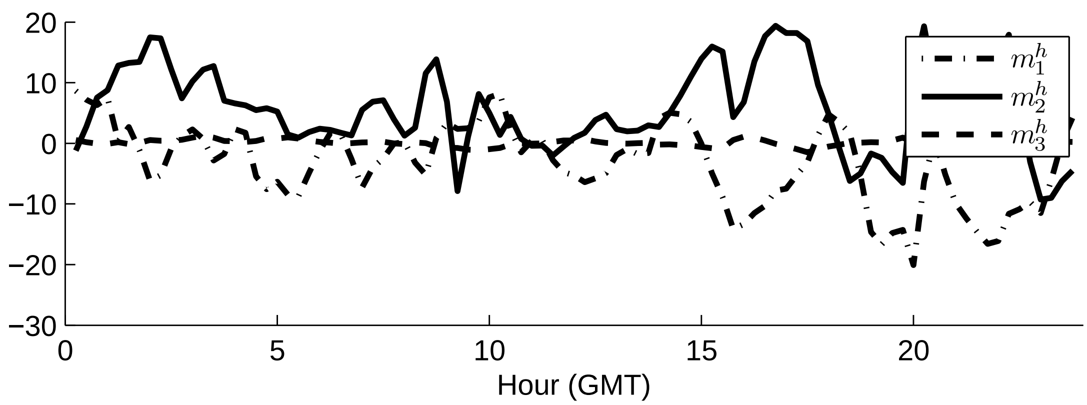

c)

Figure 5.7: Results obtained by the IONOLAB-CIT technique on 1 September 2011. a) Comparison of cost functions obtained by IRI-Plas and IONOLAB-CIT, b) Perturbation surface parameters on f_0F_2 parameter, c) Perturbation surface parameters on h_mF_2 parameter.

5.4 Temporal Validity of CIT Results

In previous sections, it is observed that there is a high temporal correlation of perturbation surface parameters. This result indicates that the ionospheric tomography results can be improved based on the previously obtained reconstructions. In this section, temporal limit of the validity of this assumption is investigated. In order to do that, perturbation surface parameters obtained by using previous measurement sets are used for predicting the future perturbation surface parameters and the cost functions obtained for the predicted perturbation surface parameters are plotted for increasingly longer time intervals. A state transition model has to be defined for predicting the future perturbation surface parameters from previous results. The state of the system at time t is denoted by the vector $\mathbf{m}_t$, which contains the perturbation surface parameters found by the IONOLAB-CIT technique at time t. The state transition model is assumed to be linear and time independent, thus it is expressed as a matrix denoted by $\mathbf{F}$. The state transition noise at time t is denoted by $\mathbf{w}_t$. The state transition equation can be written as a matrix multiplication as follows:

$$\mathbf{m}_t = \mathbf{F}\mathbf{m}_{t-1} + \mathbf{w}_t. \tag{5.1}$$

Since the perturbation surface onto the parameter h_mF_2 is defined as the perturbation surface onto the default IRI-Plas h_mF_2 surface obtained for the given input f_0F_2 surface, the perturbation surface parameters for f_0F_2 and h_mF_2 are physically independent from each other. This simplifies the problem, since the state transition models corresponding to the f_0F_2 and h_mF_2 parameters can be defined independently. Since we do not know the physical structure of the underlying model, we propose three different approaches for defining state transition model. In all cases, the state transition model is assumed to be linear, thus they are defined as state transition matrices.

In the first one, it is assumed that the ionospheric perturbation surfaces are highly correlated in time and stay constant with respect to the geodetic coordinate system. In this case, the state transition matrix is defined as the identity matrix.

$$\mathbf{F}_1 = \mathbf{I}_{6\times 6}. \tag{5.2}$$

In the second one, it is assumed that the ionospheric perturbation surfaces are highly correlated in time and stay constant with respect to the sun-fixed coordinate system. In this case, the state transition matrix is defined as the following:

$$\mathbf{F}_2 = \begin{bmatrix} 1 & 0 & 0 & 0 & 0 & 0 \\ 0 & 1 & 0 & 0 & 0 & 0 \\ 0 & \frac{2}{\lambda_{max}-\lambda_{min}}\frac{360}{24}\Delta t & 1 & 0 & 0 & 0 \\ 0 & 0 & 0 & 1 & 0 & 0 \\ 0 & 0 & 0 & 0 & 1 & 0 \\ 0 & 0 & 0 & 0 & \frac{2}{\lambda_{max}-\lambda_{min}}\frac{360}{24}\Delta t & 1 \end{bmatrix}, \tag{5.3}$$

where λ_{min} and λ_{max} represent the minimum and maximum values of longitude in the region of interest, respectively, and Δt represents the time interval in hours.

In the third one, by using the results obtained from the IONOLAB-CIT, a linear regression analysis method is used to find a state transition matrix that produces the minimum mean square error. Linear regression method tries to find the optimum linear relation between a dependent variable and one or more independent variables. The dependent variable can be predicted by using the obtained linear relation model and the independent variable(s). In the regression analysis, the perturbation surface parameters calculated by the IONOLAB-CIT are used as dependent variables, and the perturbation surface parameters calculated by the IONOLAB-CIT corresponding to the previous time instant are used as the independent variables. Let $\mathbf{m}_t$ denote the array containing the perturbation surface parameters calculated by the IONOLAB-CIT technique at time t, and $m_{t,k}$ denote the kth parameter in $\mathbf{m}_t$. The corresponding regression model can be written as follows:

$$\mathbf{y_k} = \mathbf{X}\mathbf{f}_k + \epsilon_\mathbf{k}, \tag{5.4}$$

where $\epsilon_\mathbf{k}$ is the error term, and $\mathbf{y_k}$ and $\mathbf{X}$ are defined as:

$$\mathbf{y_k} = \begin{bmatrix} m_{1,k} \\ m_{2,k} \\ \cdots \\ m_{t,k} \end{bmatrix}, \tag{5.5}$$

$$\mathbf{X} = \begin{bmatrix} \mathbf{m}_0^T \\ \mathbf{m}_1^T \\ \cdots \\ \mathbf{m}_{t-1}^T \end{bmatrix}. \tag{5.6}$$

The least squares estimation for $\mathbf{f}_k$ can be found by using the following equation:

$$\hat{\mathbf{f}}_k = \left(\mathbf{X}^T\mathbf{X}\right)^{-1}\mathbf{X}^T\mathbf{y_k}. \tag{5.7}$$

The state transition matrix found by the linear regression method can be written as follows:

$$\mathbf{F}_3 = \begin{bmatrix} \hat{\mathbf{f}}_0^T \\ \hat{\mathbf{f}}_1^T \\ \hat{\mathbf{f}}_2^T \\ \hat{\mathbf{f}}_3^T \\ \hat{\mathbf{f}}_4^T \\ \hat{\mathbf{f}}_5^T \end{bmatrix}. \tag{5.8}$$

The state transition matrices found by the linear regression method for days 10 March 2011, 28 May 2011, 12 June 2011 and 1 September 2011 are shown in Table 5.1.

Table 5.1: The state transition matrices found by the linear regression method for days 10 March 2011, 28 May 2011, 12 June 2011 and 1 September 2011.

10 March 2011	$\begin{bmatrix} 0.8948 & 0.0449 & -0.0227 & -0.0025 & 0.0001 & -0.0016 \\ -0.0193 & 0.9337 & -0.0240 & -0.0056 & 0.0012 & -0.0166 \\ 0.1666 & 0.2432 & 1.0211 & 0.0002 & -0.0047 & 0.0278 \\ -1.6115 & -0.1905 & -0.6192 & 0.7293 & -0.0261 & -0.4427 \\ -2.2091 & -0.7800 & 0.9729 & 0.0117 & 0.7707 & 0.5969 \\ -0.0734 & 0.0230 & -0.0087 & 0.0020 & 0.0052 & 0.8897 \end{bmatrix}$
28 May 2011	$\begin{bmatrix} 0.9036 & 0.0043 & 0.0594 & 0.0048 & 0.0002 & 0.0204 \\ -0.0335 & 0.9833 & -0.0110 & 0.0002 & 0.0004 & 0.0053 \\ -0.0006 & 0.0565 & 0.9814 & 0.0020 & -0.0054 & 0.0414 \\ -0.4809 & -0.7323 & -0.0859 & 0.8333 & -0.0270 & -0.0160 \\ -0.5502 & 1.7334 & 0.3886 & -0.0746 & 0.8121 & 1.3133 \\ -0.1055 & 0.0869 & -0.0737 & -0.0158 & 0.0057 & 0.7088 \end{bmatrix}$
12 June 2011	$\begin{bmatrix} 0.9379 & -0.0603 & 0.0382 & 0.0041 & 0.0027 & 0.0536 \\ 0.0564 & 0.8994 & 0.0150 & 0.0033 & 0.0031 & 0.0214 \\ 0.0532 & 0.0576 & 0.9339 & 0.0041 & -0.0042 & 0.0113 \\ 0.6308 & -2.5860 & 1.4042 & 0.8144 & 0.0654 & 0.0447 \\ -2.0605 & 1.2511 & -0.4184 & -0.1354 & 0.8336 & -0.0393 \\ -0.2519 & 0.2769 & -0.1133 & -0.0155 & -0.0087 & 0.7440 \end{bmatrix}$
1 September 2011	$\begin{bmatrix} 0.8215 & -0.0163 & -0.0310 & -0.0021 & -0.0025 & -0.0263 \\ 0.0618 & 0.9247 & -0.0178 & -0.0008 & -0.0014 & -0.0528 \\ -0.0480 & -0.0082 & 0.9421 & 0.0052 & -0.0025 & 0.0166 \\ 0.2893 & -0.4772 & 1.1756 & 0.8222 & 0.0446 & -0.5348 \\ 5.9651 & -0.9710 & 1.3819 & -0.0299 & 0.9042 & 3.1134 \\ -0.1053 & 0.2264 & -0.1449 & -0.0007 & -0.0073 & 0.7282 \end{bmatrix}$

Figures 5.8 - 5.19 show the cost functions obtained for the predicted perturbation parameters for each state transition matrix and for increasingly longer time intervals, for selected calm and stormy days.

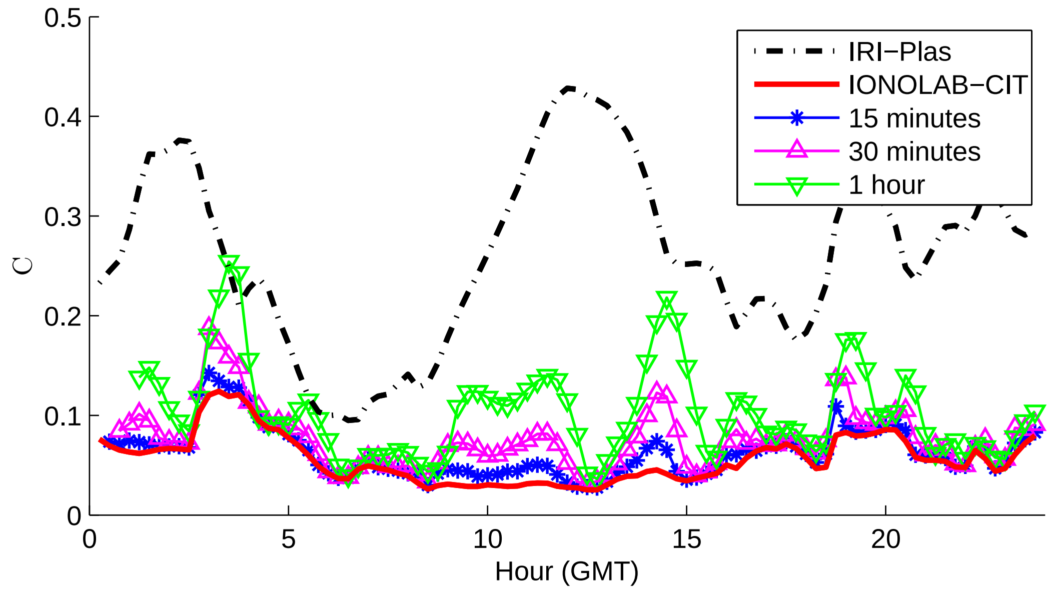

Figure 5.8: Cost functions of the perturbation surface parameters predicted by using the state transition matrix $\mathbf{F}_1$ for increasingly longer time intervals, on 10 March 2011.

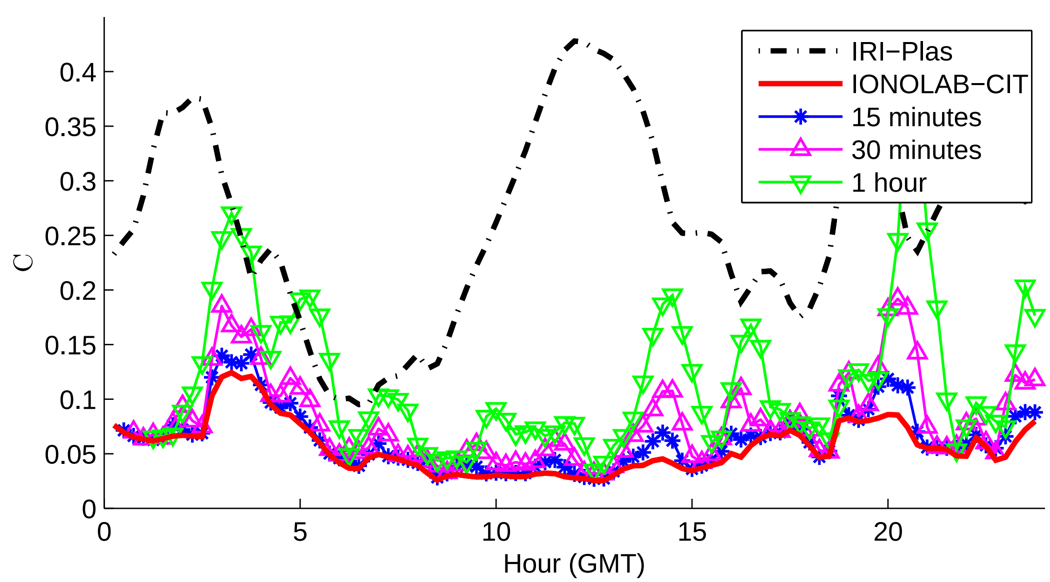

Figure 5.9: Cost functions of the perturbation surface parameters predicted by using the state transition matrix $\mathbf{F}_2$ for increasingly longer time intervals, on 10 March 2011.

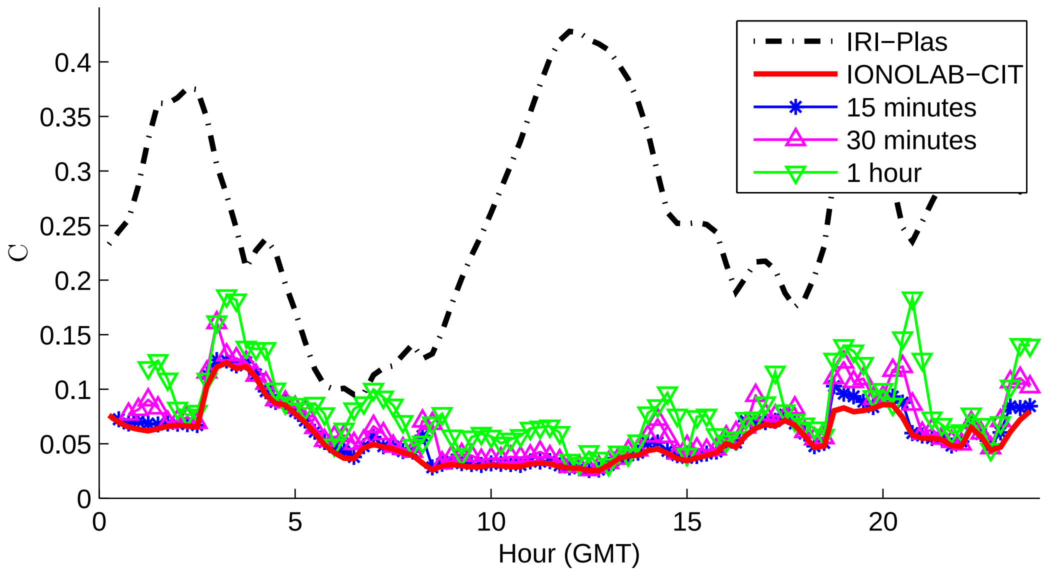

Figure 5.10: Cost functions of the perturbation surface parameters predicted by using the state transition matrix $\mathbf{F}_3$ for increasingly longer time intervals, on 10 March 2011.

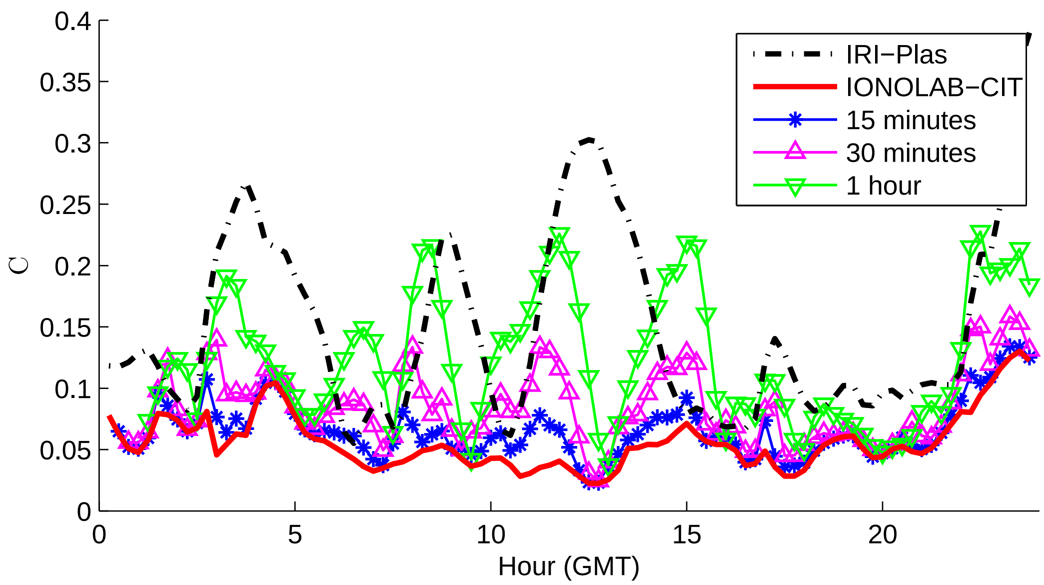

Figure 5.11: Cost functions of the perturbation surface parameters predicted by using the state transition matrix $\mathbf{F}_1$ for increasingly longer time intervals, on 28 May 2011.

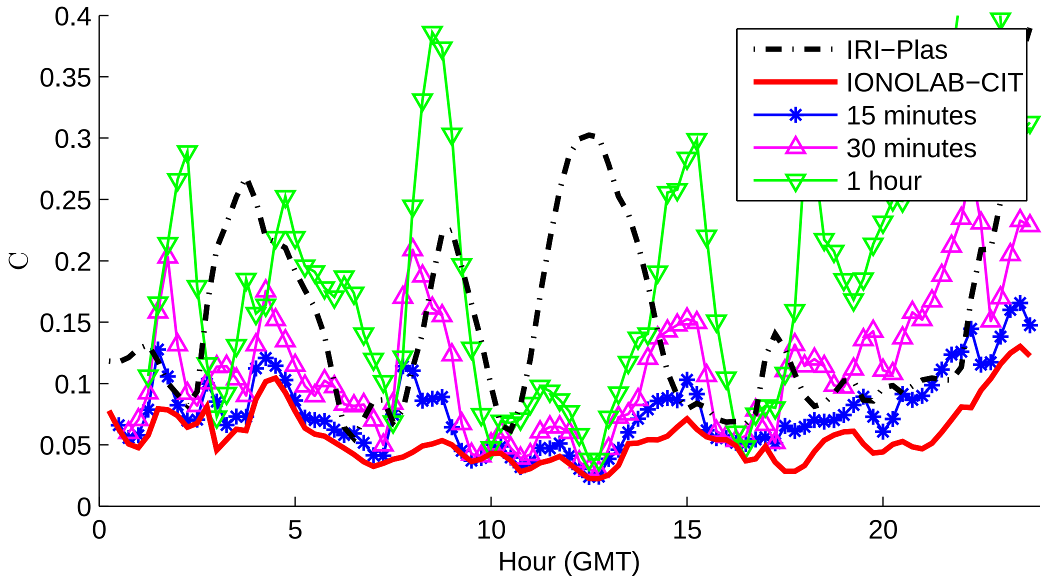

Figure 5.12: Cost functions of the perturbation surface parameters predicted by using the state transition matrix $\mathbf{F}_2$ for increasingly longer time intervals, on 28 May 2011.

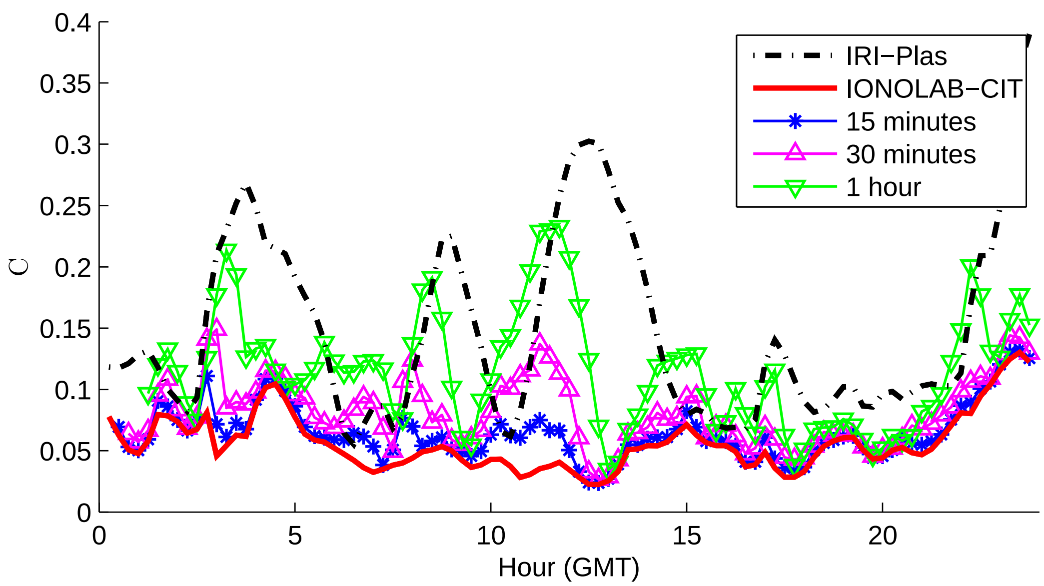

Figure 5.13: Cost functions of the perturbation surface parameters predicted by using the state transition matrix $\mathbf{F}_3$ for increasingly longer time intervals, on 28 May 2011.

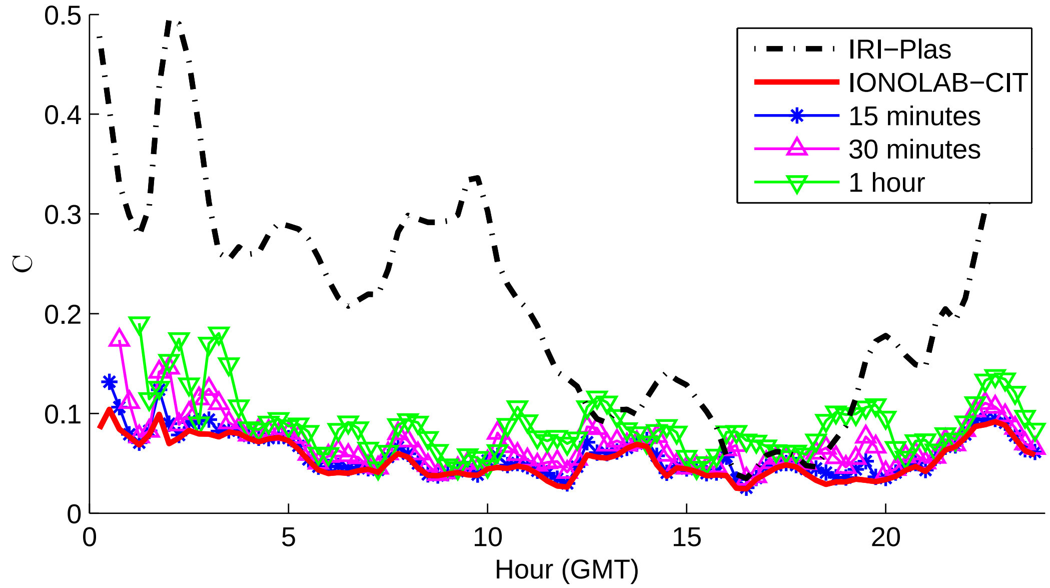

Figure 5.14: Cost functions of the perturbation surface parameters predicted by using the state transition matrix $\mathbf{F}_1$ for increasingly longer time intervals, on 12 June 2011.

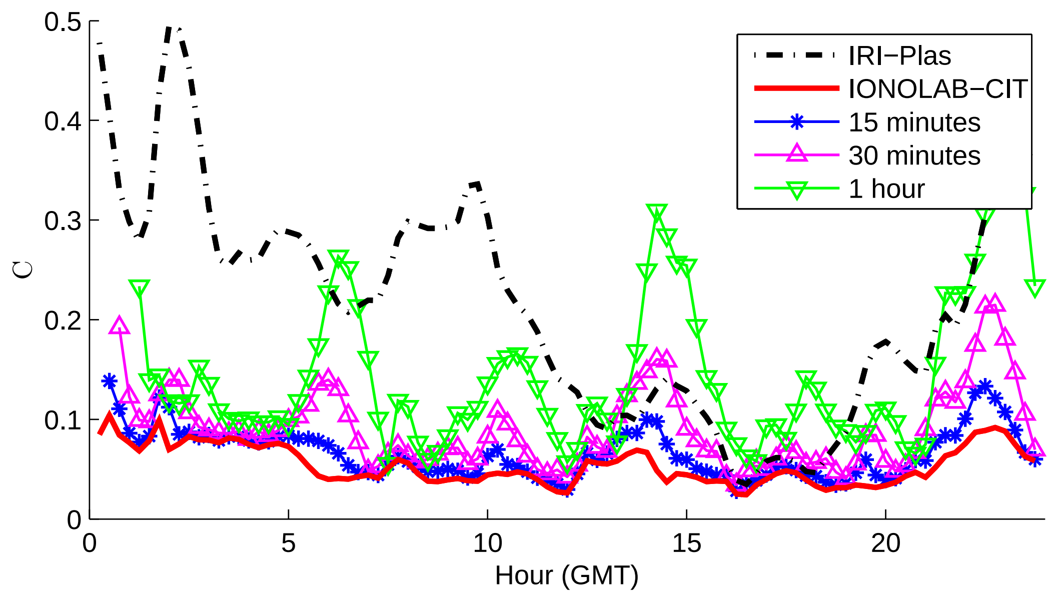

Figure 5.15: Cost functions of the perturbation surface parameters predicted by using the state transition matrix $\mathbf{F}_2$ for increasingly longer time intervals, on 12 June 2011.

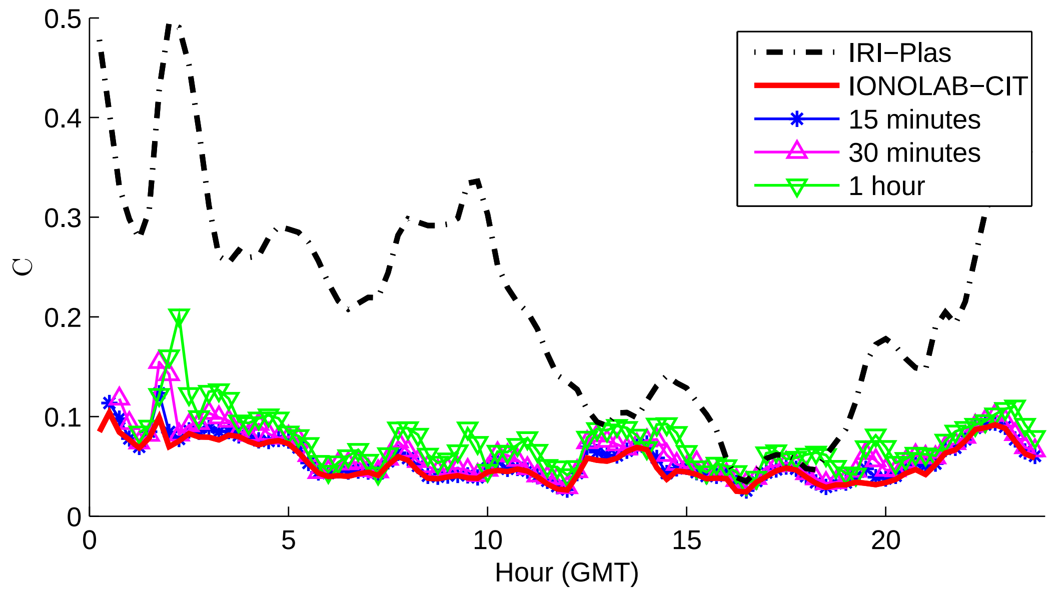

Figure 5.16: Cost functions of the perturbation surface parameters predicted by using the state transition matrix $\mathbf{F}_3$ for increasingly longer time intervals, on 12 June 2011.

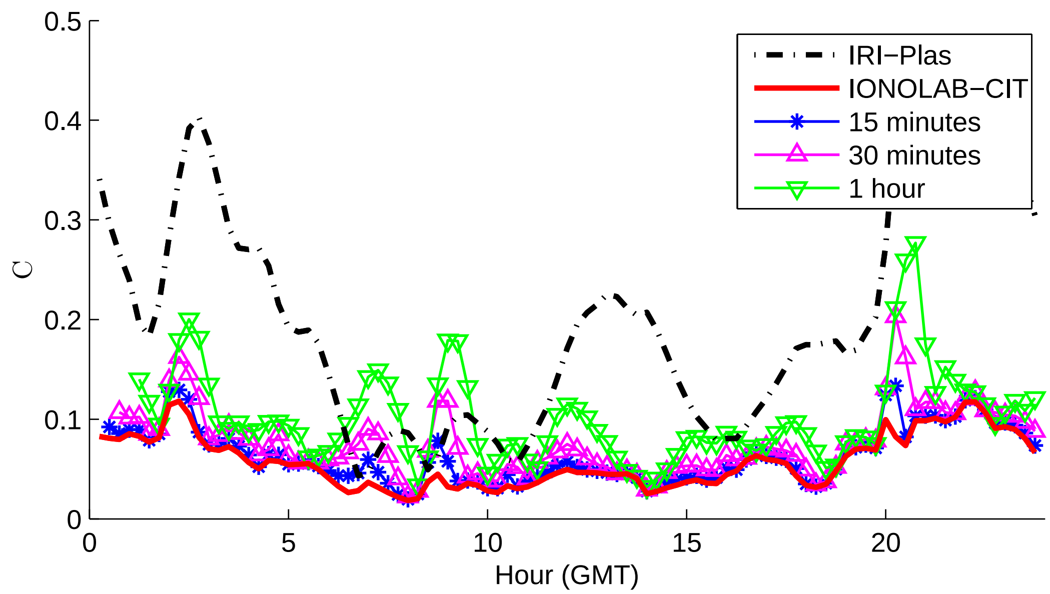

Figure 5.17: Cost functions of the perturbation surface parameters predicted by using the state transition matrix $\mathbf{F}_1$ for increasingly longer time intervals, on 1 September 2011.

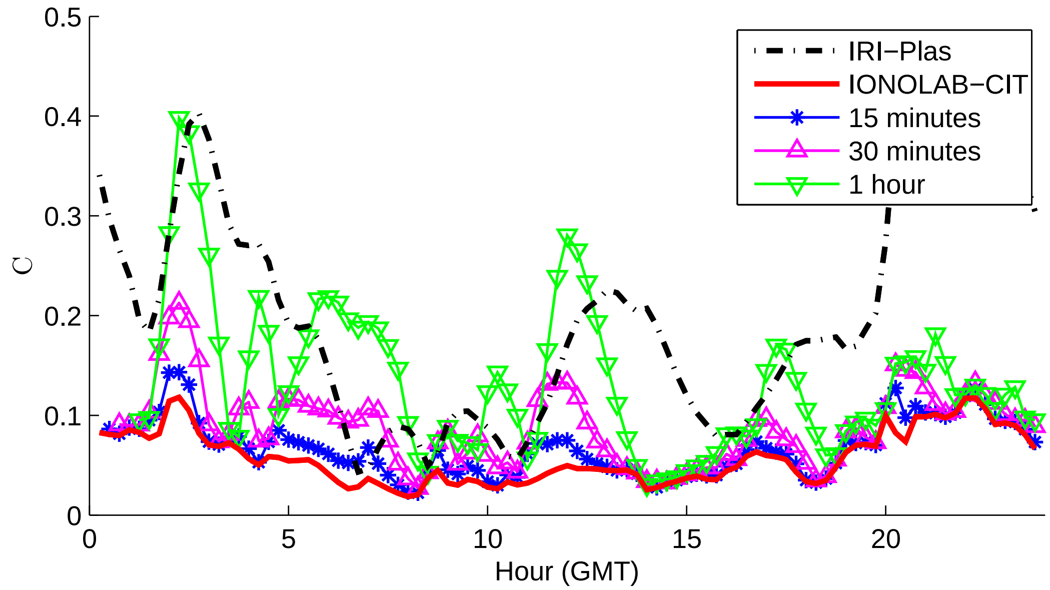

Figure 5.18: Cost functions of the perturbation surface parameters predicted by using the state transition matrix $\mathbf{F}_2$ for increasingly longer time intervals, on 1 September 2011.

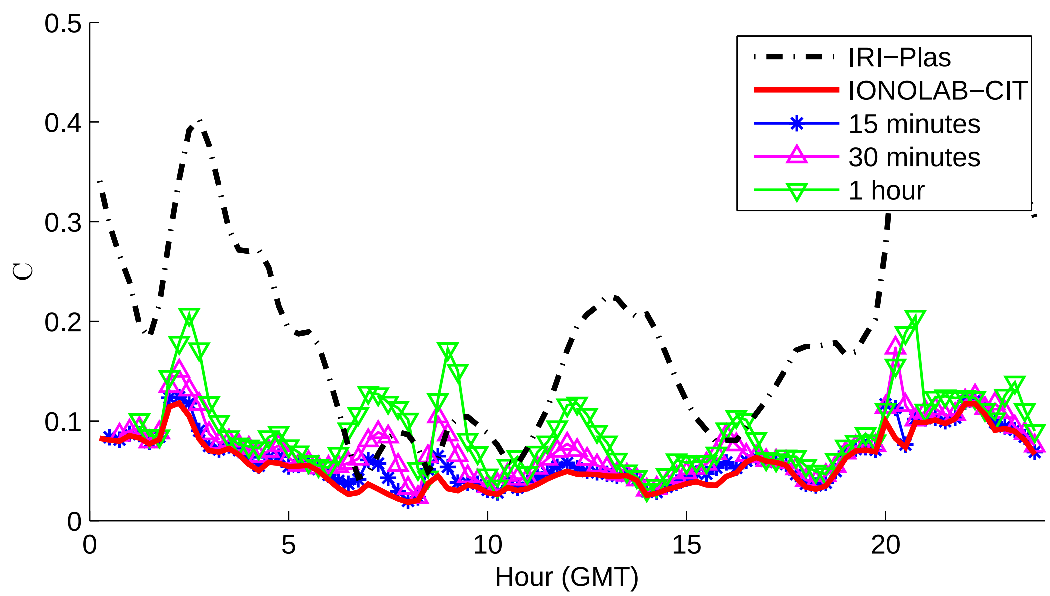

Figure 5.19: Cost functions of the perturbation surface parameters predicted by using the state transition matrix $\mathbf{F}_3$ for increasingly longer time intervals, on 1 September 2011.

Obtained results show that both $\mathbf{F}_1$ and $\mathbf{F}_3$ produce similar estimates, which are better than those found by $\mathbf{F}_2$. This result indicates that using previous disturbance surfaces which are obtained over the same region defined in geodetic coordinates produce better estimates than rotating them with respect to the sun zenith angle. Results also show that the temporal validity of the CIT results obtained by using the IONOLAB-CIT decreases as the time interval between the measurements and the predictions get larger, and after time interval reaches to certain values, using previous results may increase the cost function above the cost value obtained by using the default IRI-Plas parameters. Figures 5.20, 5.21, 5.22 and 5.23 contain the average cost values obtained by using the state transition matrices $\mathbf{F}_1$, $\mathbf{F}_2$ and $\mathbf{F}_3$ for increasingly longer intervals, and their comparison with IONOLAB-CIT and IRI-Plas results. Results indicate that, in the case of $\mathbf{F}_1$, using the predicted perturbation surface parameters produces better results than using the default IRI-Plas parameters even for a 3 hour interval for days 10 March 2011, 12 June 2011 and 1 September 2011. On 28 May 2011, using the predicted perturbation surface parameters produces better results than using the default IRI-Plas parameters up to 1 hour interval. This is basically because of the low cost value obtained by using the IRI-Plas model on 28 May 2011, which indicates that the IRI-Plas model more successfully predicts the ionosphere on that day. Based on the results, it is safe to say that predicting future perturbation surface parameters by using the state transition matrix $\mathbf{F}_1$ on the previous IONOLAB-CIT results obtained up to 1 hour ago produces better results than using the IRI-Plas model directly. Results also show that, the state transition matrix $\mathbf{F}_1$ produces very similar results to $\mathbf{F}_3$, which is the optimum matrix in terms of MMSE estimation.

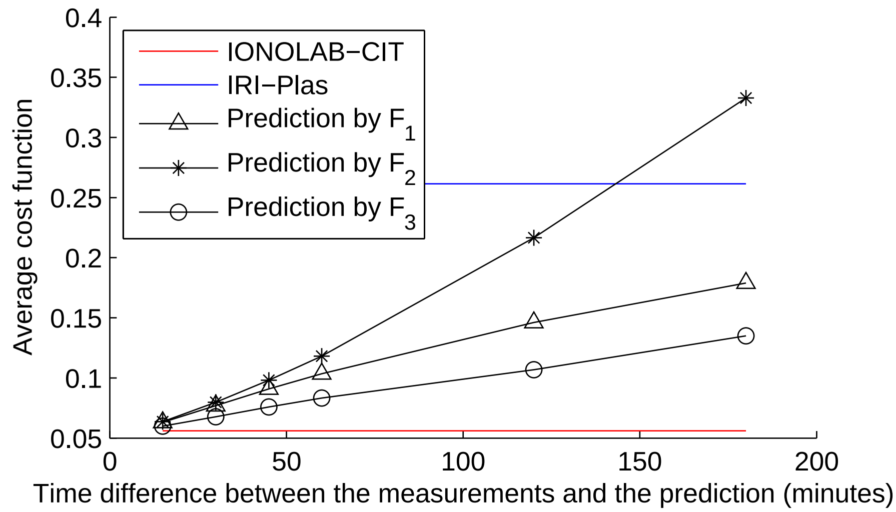

Figure 5.20: Average cost values obtained by using $\mathbf{F}_1$, $\mathbf{F}_2$ and $\mathbf{F}_3$ state transition matrices for increasingly longer time intervals, and their comparison with IONOLAB-CIT and IRI-Plas results, on 10 March 2011.

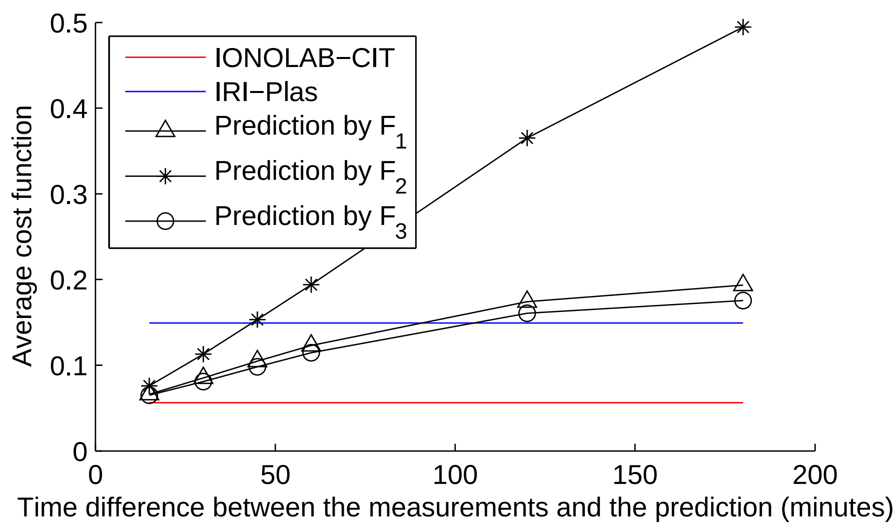

Figure 5.21: Average cost values obtained by using $\mathbf{F}_1$, $\mathbf{F}_2$ and $\mathbf{F}_3$ state transition matrices for increasingly longer time intervals, and their comparison with IONOLAB-CIT and IRI-Plas results, on 28 May 2011.

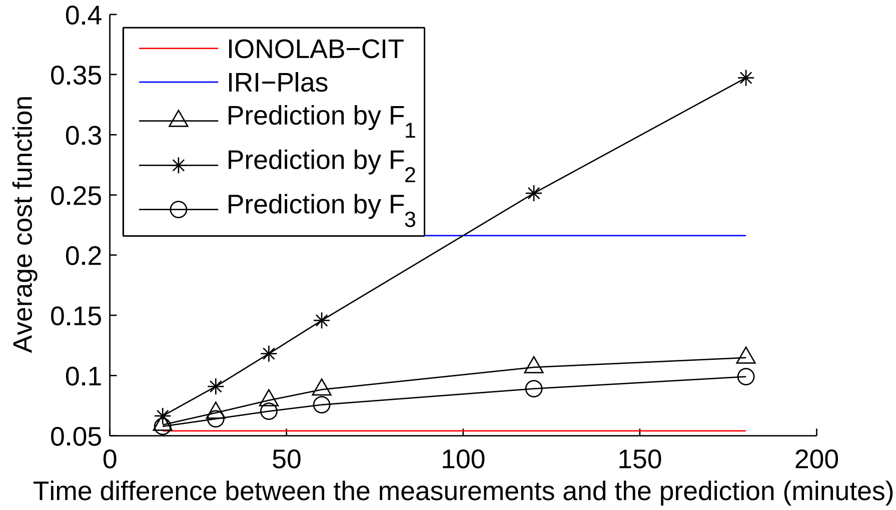

Figure 5.22: Average cost values obtained by using $\mathbf{F}_1$, $\mathbf{F}_2$ and $\mathbf{F}_3$ state transition matrices for increasingly longer time intervals, and their comparison with IONOLAB-CIT and IRI-Plas results, on 12 June 2011.

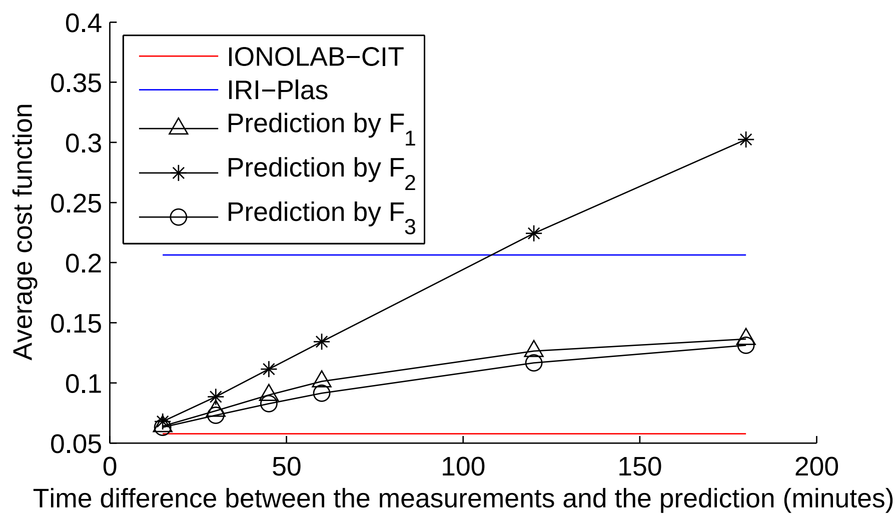

Figure 5.23: Average cost values obtained by using $\mathbf{F}_1$, $\mathbf{F}_2$ and $\mathbf{F}_3$ state transition matrices for increasingly longer time intervals, and their comparison with IONOLAB-CIT and IRI-Plas results, on 1 September 2011.

5.5 On-line Tracking of the Perturbation Parameters in Time

In order to track perturbation surface parameters in time, a Kalman filtering based approach is implemented over the sequence of perturbation surface parameters [84]. Use of Kalman filtering increases the robustness and accuracy of the proposed CIT technique.

In our application of the Kalman filter, the state of the system at time instant t is represented as the vector $\mathbf{m}_t$ containing perturbation surface parameters, the state transition matrix is time independent and is represented as $\mathbf{F}$, and there is no control input to the system. The state update equation is given as:

$$\mathbf{m}_t = \mathbf{F}\mathbf{m}_{t-1} + \mathbf{w}_t, \tag{5.9}$$

where $\mathbf{w}_t$ represents the state transition noise at time instant t. The observable parameter of the system is the perturbation surface parameters estimated by the IONOLAB-CIT technique, and it is related to the system state via the following equation:

$$\mathbf{z}_t = \mathbf{m}_t + \mathbf{v}_t, \tag{5.10}$$

where $\mathbf{z}_t$ is the observation, and $\mathbf{v}_t$ is the observation noise at time instant t. Since the perturbation parameters are uncorrelated with each other, the state transition noise and the observation noise are selected as:

$$\mathbf{w}_t \sim N(0, \mathbf{Q}), \tag{5.11}$$

$$\mathbf{Q} = q\mathbf{I}_{6\times 6}, \tag{5.12}$$

$$\mathbf{v}_t \sim N(0, \mathbf{R}), \tag{5.13}$$

$$\mathbf{R} = r\mathbf{I}_{6\times 6}. \tag{5.14}$$

After determining the state transition and the observation models of the system, Kalman filter prediction and update phases can be written as:

Prediction:

$$\hat{\mathbf{m}}_{t|t-1} = \mathbf{F}\hat{\mathbf{m}}_{t-1|t-1}, \tag{5.15}$$

$$\mathbf{P}_{t|t-1} = \mathbf{F}\mathbf{P}_{t-1|t-1}\mathbf{F}^T + \mathbf{Q}. \tag{5.16}$$

Update:

$$\hat{\mathbf{y}}_t = \mathbf{z}_t - \hat{\mathbf{m}}_{t|t-1}, \tag{5.17}$$

$$\mathbf{S}_t = \mathbf{P}_{t|t-1} + \mathbf{R}, \tag{5.18}$$

$$\mathbf{K}_t = \mathbf{P}_{t|t-1}\mathbf{S}_t^{-1}, \tag{5.19}$$

$$\hat{\mathbf{m}}_{t|t} = \hat{\mathbf{m}}_{t|t-1} + \mathbf{K}_t\hat{\mathbf{y}}_t, \tag{5.20}$$

$$\mathbf{P}_{t|t} = (\mathbf{I} - \mathbf{K}_t)\mathbf{P}_{t|t-1}. \tag{5.21}$$

The noise coefficients q and r determine the reliance on the state transition model or the measurements, i.e., the IONOLAB-CIT results. In this scenario, the ratio of q and r, rather than their exact values, is important for Kalman filtering results.

5.6 Off-line Smoothing of the Perturbation Surface Parameters in Time

Kalman filtering approach produces estimates depending on the current and previous observations, and it is the optimum causal filtering when the system and observation noises are Gaussian-distributed. However, it is possible to smooth the estimates further by using the off-line Kalman smoothing technique. In order to do that, the Rauch-Tung-Striebel smoother, which is basically a two-pass algorithm based on the Kalman filter approach is implemented in this thesis [85]. This smoother works by applying forward and backward passes on the estimated perturbation surface parameters. Forward pass is the same as the Kalman filtering approach, however, the state estimations and covariance matrices are stored to be used in the backward pass. The backward pass is performed by the following recursive equations:

$$\hat{\mathbf{m}}_{t|n} = \hat{\mathbf{m}}_{t|t} + \mathbf{C}_t(\hat{\mathbf{m}}_{t+1|n} - \hat{\mathbf{m}}_{t+1|t}), \tag{5.22}$$

$$\mathbf{P}_{t|n} = \mathbf{P}_{t|t} + \mathbf{C}_t(\mathbf{P}_{t+1|n} - \mathbf{P}_{t+1|t})\mathbf{C}_t^T, \tag{5.23}$$

where n is the total number of observations, and $\mathbf{C}$ is defined as:

$$\mathbf{C}_t = \mathbf{P}_{t|t}\mathbf{F}^T\mathbf{P}_{t+1|t}^{-1}. \tag{5.24}$$

It is possible to use Kalman smoothing approach on-line as a non-causal filter for better estimations. As the new measurements are obtained, the previous estimations can be further corrected after some time delay.

5.7 Results

In the following simulations, the state transition matrix is used as $\mathbf{F}_1$, the state transition noise $\mathbf{Q}$ is selected as $0.2\mathbf{I}$, and the measurement noise $\mathbf{R}$ is selected as $0.1\mathbf{I}$. The region of reconstruction is selected in between 34° N and 44° N latitudes, 24° E and 47° E longitudes, and 100 and 20,000 km in height. The real GPS-STEC measurements computed by the IONOLAB-STEC method from the data obtained from TNGPN-Active stations are used in the experiments. Three different sets of experiments are carried out by using the Kalman tracking and the Kalman smoothing methods. Each experiment explained in detail and obtained results are given below.

In the first set of experiments, data from all available GPS receiver stations are used, and all of the results obtained by the IONOLAB-CIT technique within 24 hours are used in the observation set of the Kalman smoothing method. Figures 5.24-5.35 show perturbation surface parameters obtained on 1 September 2011 and 10 March 2011, with using a) only the IONOLAB-CIT technique, b) the IONOLAB-CIT and the Kalman tracking and c) the IONOLAB-CIT and the Kalman smoothing approaches. Results show how the Kalman tracking/smoothing methods smooth out the obtained perturbation surface parameters in time. Results also show that the Kalman tracking latency on the IONOLAB-CIT results is minimized by the Kalman smoothing approach. Figures 5.36 and 5.37 show cost functions obtained by using the Kalman tracking/smoothing methods on 1 September 2011 and 10 March 2011, compared with the IONOLAB-CIT results, which are obtained independently. Since the IONOLAB-CIT technique minimizes the cost function independently from the previous results, it achieves the minimum cost function. Using the Kalman tracking/smoothing on the results slightly increases this cost. However, using independent IONOLAB-CIT runs for each time instant may suffer from over fitting in the presence of noisy data. Therefore, obtaining the minimum cost function does not necessarily mean obtaining the most robust result.

In the second set of experiments, 3 GPS receiver station experiment in Chapter 4 is repeated with the Kalman tracking and smoothing methods. All of the results obtained by the IONOLAB-CIT technique within 24 hours are used in the observation set of the Kalman smoothing method. Figures 5.38 and 5.39 show results obtained by using 3 GPS receiver stations given in Figure 4.18a on 1 September 2011 and 10 March 2011, with and without using the Kalman tracking/smoothing approaches. Results show that the cost function obtained with and without using Kalman filtering approaches are very similar in most cases. However, for the problematic cases where the IONOLAB-CIT produces significantly high cost values with respect to the full GPS receiver station set experiments, Kalman tracking and smoothing approaches produce better cost values. This result can be interpreted as that using Kalman tracking/smoothing methods increases the robustness of the results obtained by the IONOLAB-CIT technique, especially when the data from a few GPS receiver stations are used in the reconstruction.

In the third set of experiments, 3 GPS receiver station experiment in Chapter 4 is repeated with the Kalman smoothing method for different observation set sizes in time. The Kalman smoothing method is run by using all results obtained by the IONOLAB-CIT technique up to 15 minutes into the future, and the results are compared with the performance of the Kalman smoothing method when all of the results obtained by the IONOLAB-CIT technique within 24 hours are used. Figures 5.40 and 5.41 show results obtained by using 3 GPS receiver stations given in Figure 4.18a on 1 September 2011 and 10 March 2011. Results show that the performance difference between two cases is very small, which indicates that using the Kalman smoothing method on-line with 15 minutes delay is sufficient for exploiting the advantage of the Kalman smoothing method.

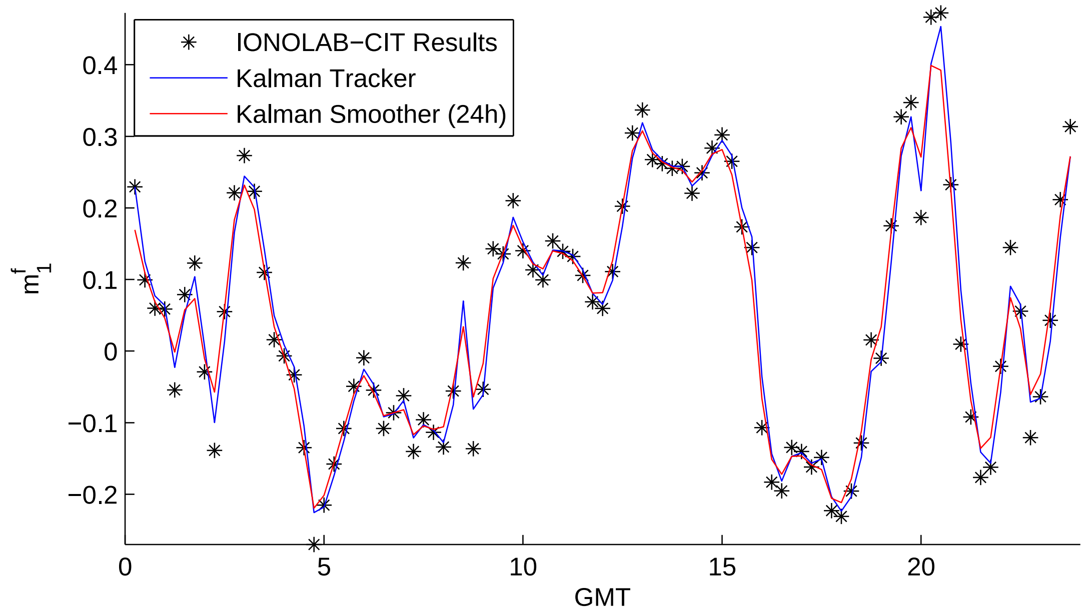

Figure 5.24: IONOLAB-CIT results, and Kalman tracking and smoothing results for m_1^f, on 1 September 2011.

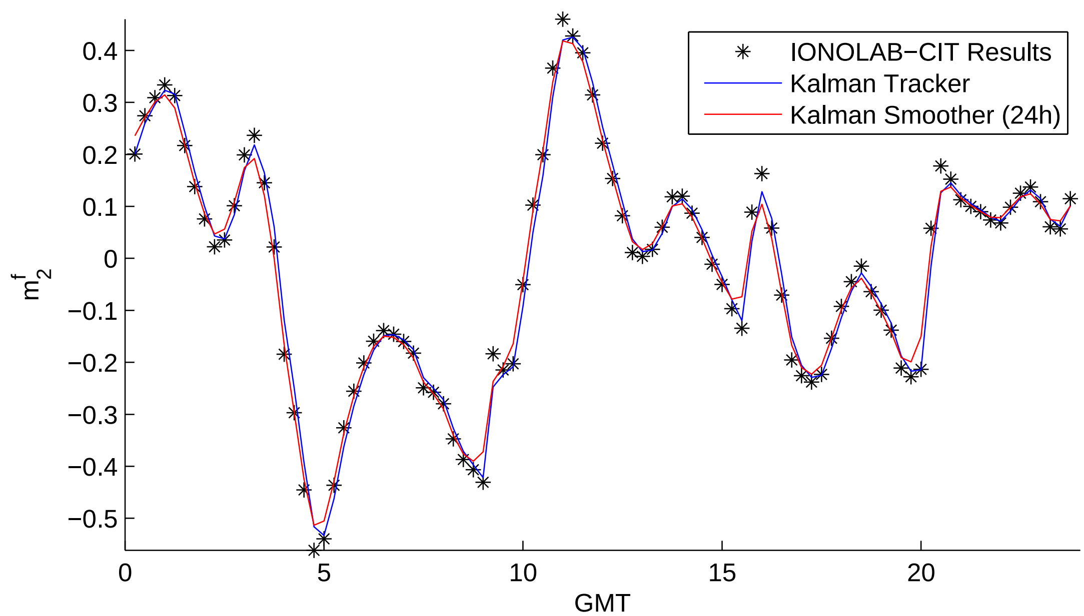

Figure 5.25: IONOLAB-CIT results, and Kalman tracking and smoothing results for m_2^f, on 1 September 2011.

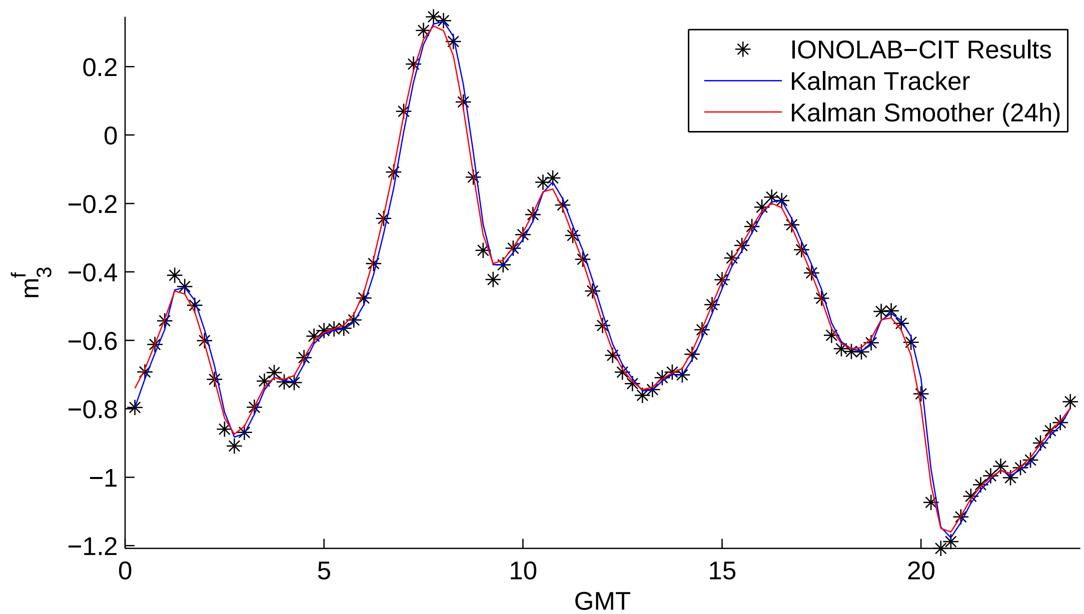

Figure 5.26: IONOLAB-CIT results, and Kalman tracking and smoothing results for m_3^f, on 1 September 2011.

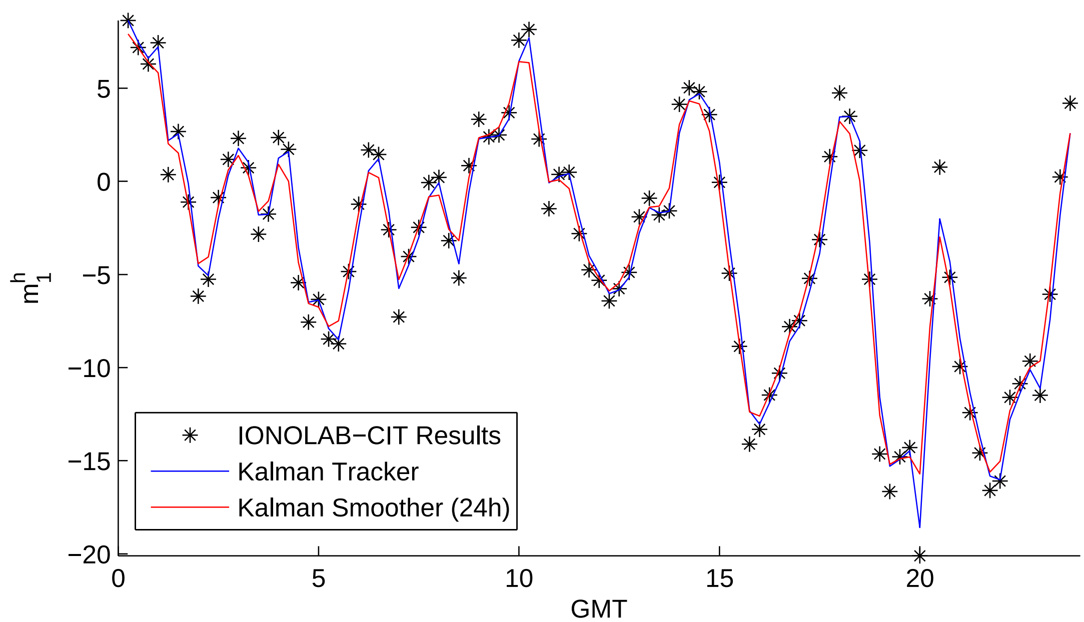

Figure 5.27: IONOLAB-CIT results, and Kalman tracking and smoothing results for m_1^h, on 1 September 2011.

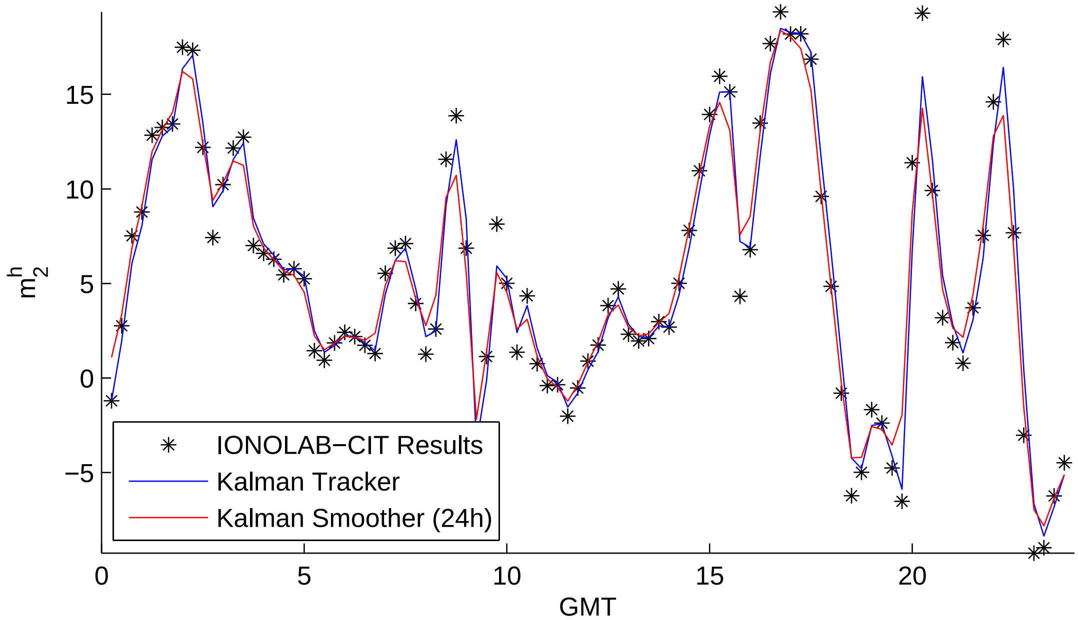

Figure 5.28: IONOLAB-CIT results, and Kalman tracking and smoothing results for m_2^h, on 1 September 2011.

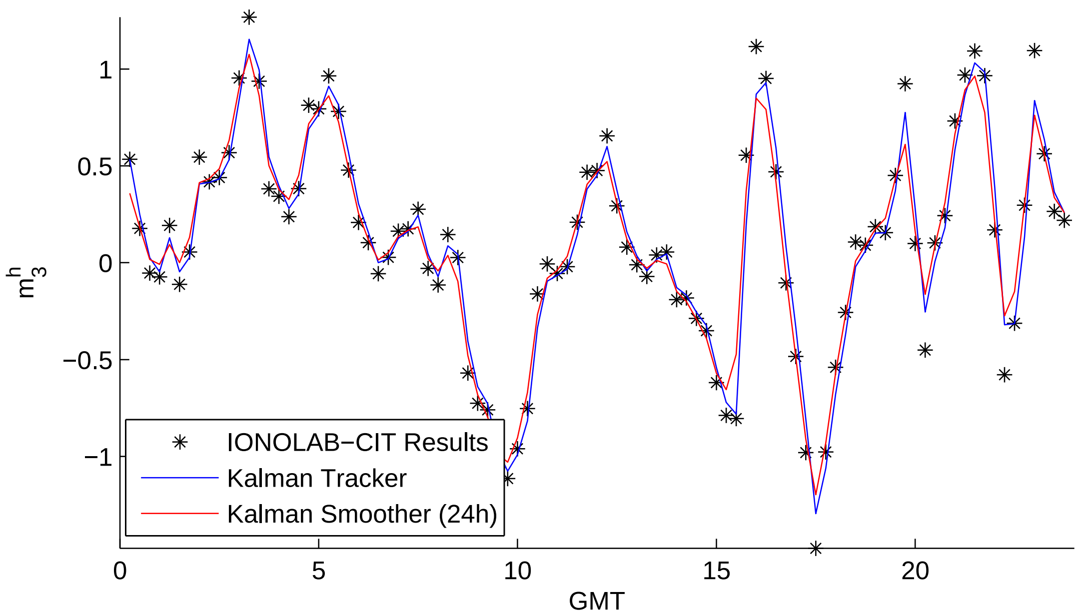

Figure 5.29: IONOLAB-CIT results, and Kalman tracking and smoothing results for m_3^h, on 1 September 2011.

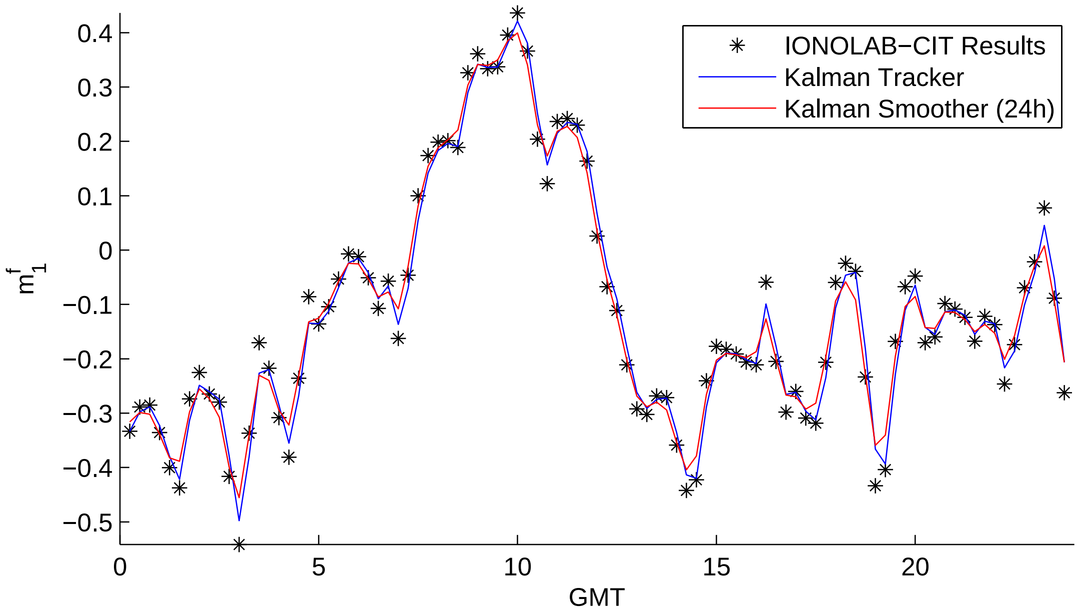

Figure 5.30: IONOLAB-CIT results, and Kalman tracking and smoothing results for m_1^f, on 10 March 2011.

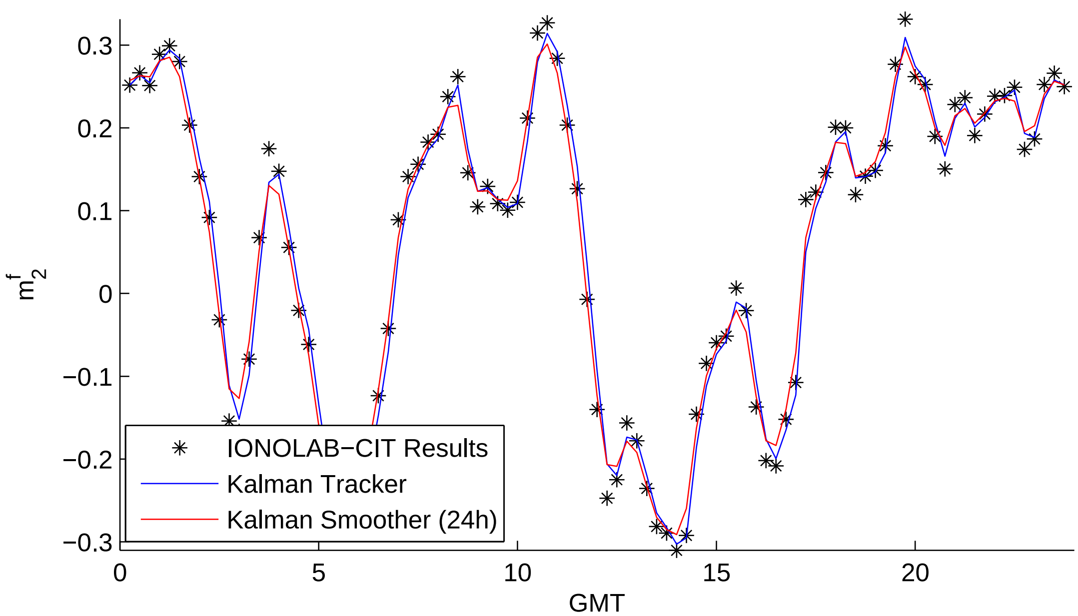

Figure 5.31: IONOLAB-CIT results, and Kalman tracking and smoothing results for m_2^f, on 10 March 2011.

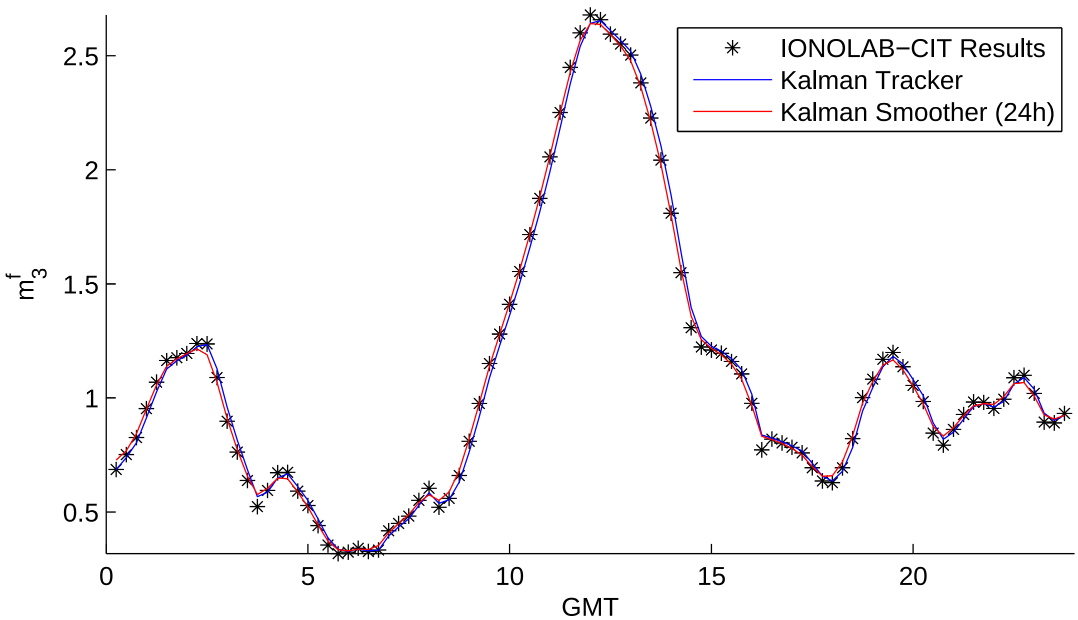

Figure 5.32: IONOLAB-CIT results, and Kalman tracking and smoothing results for m_3^f, on 10 March 2011.

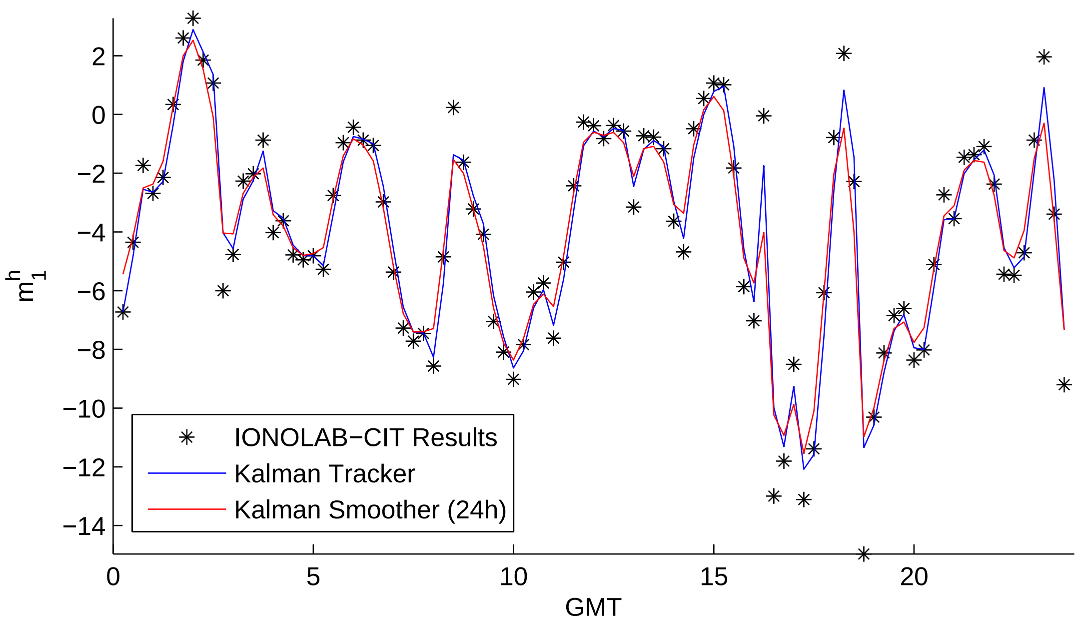

Figure 5.33: IONOLAB-CIT results, and Kalman tracking and smoothing results for m_1^h, on 10 March 2011.

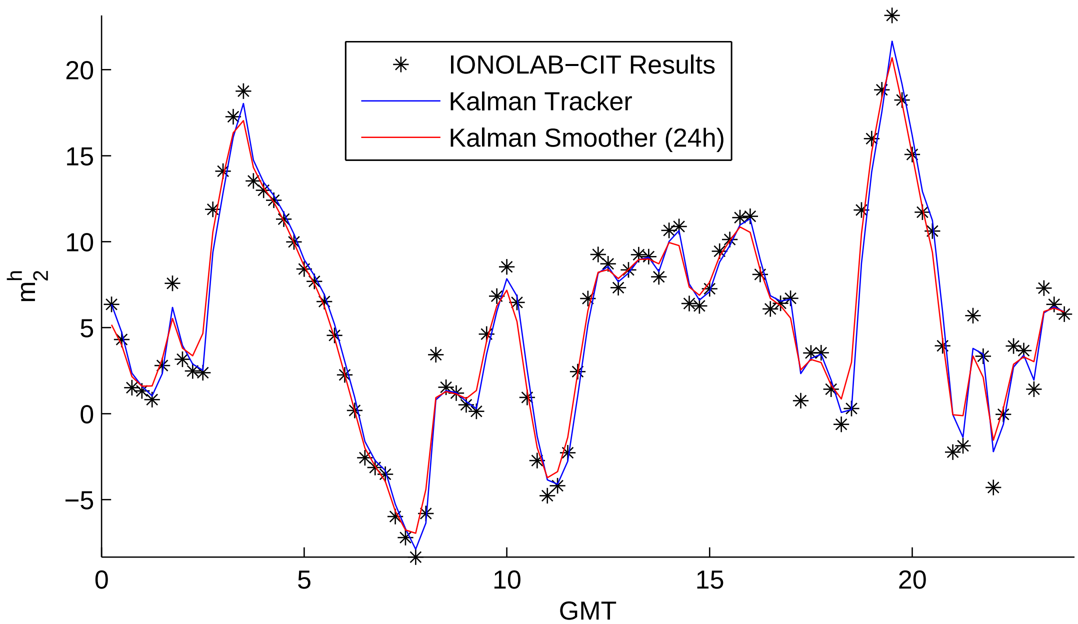

Figure 5.34: IONOLAB-CIT results, and Kalman tracking and smoothing results for m_2^h, on 10 March 2011.

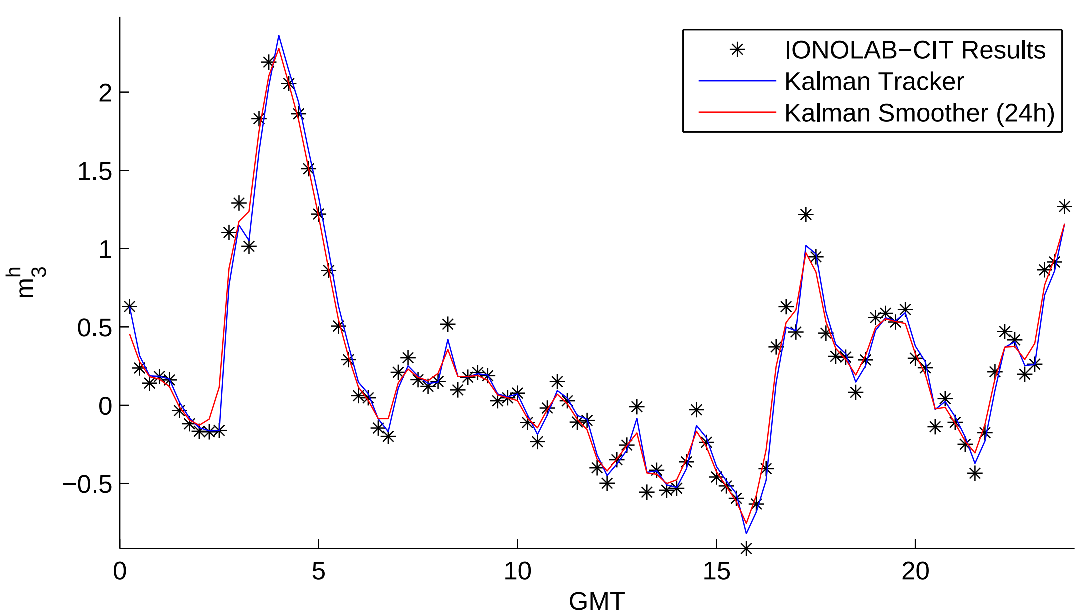

Figure 5.35: IONOLAB-CIT results, and Kalman tracking and smoothing results for m_3^h, on 10 March 2011.

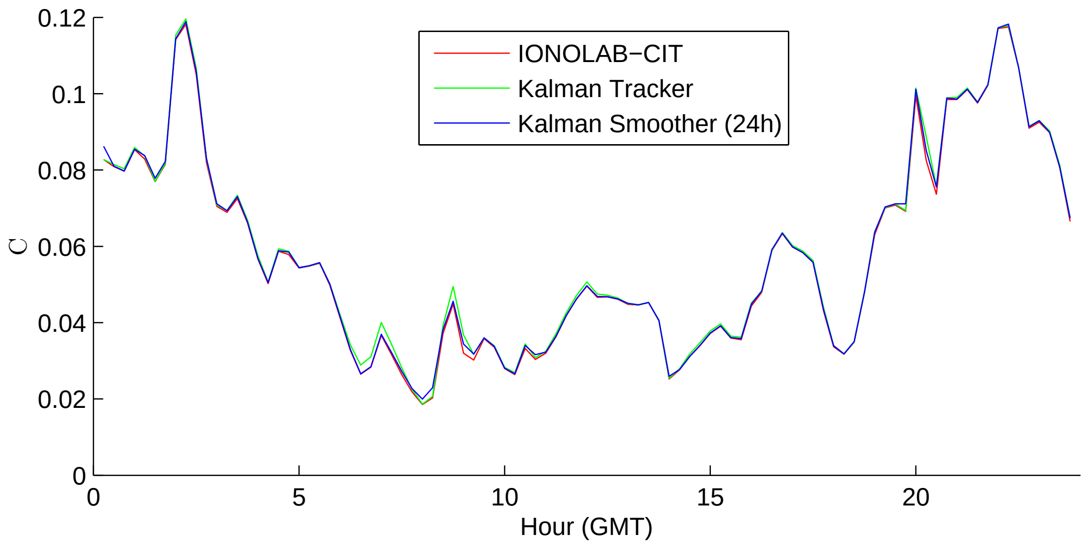

Figure 5.36: Cost function obtained for independent runs of IONOLAB-CIT, and cost function obtained after application of Kalman tracking and Kalman smoothing methods on 1 September 2011, when all GPS receiver stations are used in reconstructions.

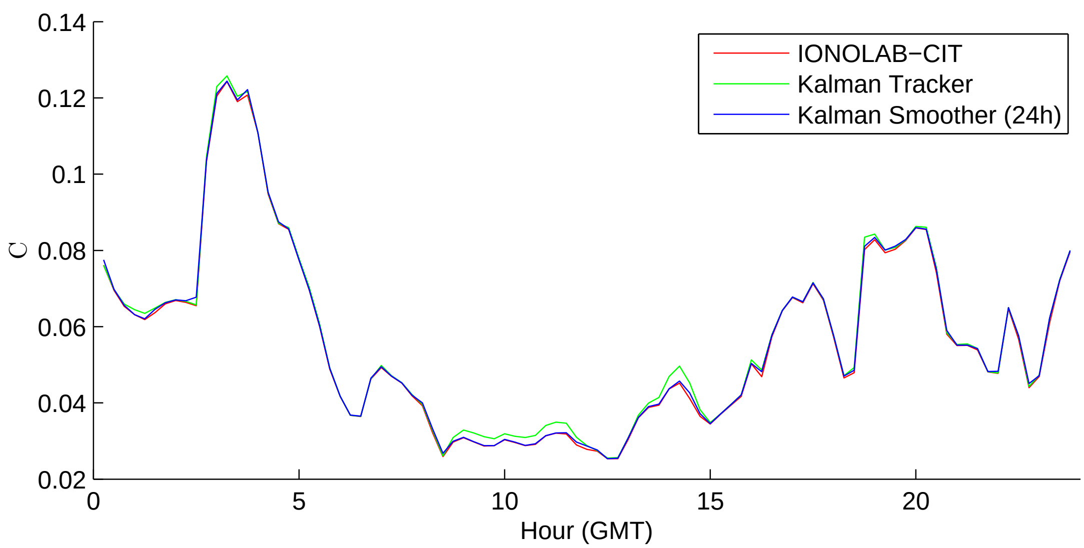

Figure 5.37: Cost function obtained for independent runs of IONOLAB-CIT, and cost function obtained after application of Kalman tracking and Kalman smoothing methods on 10 March 2011, when all GPS receiver stations are used in reconstructions.

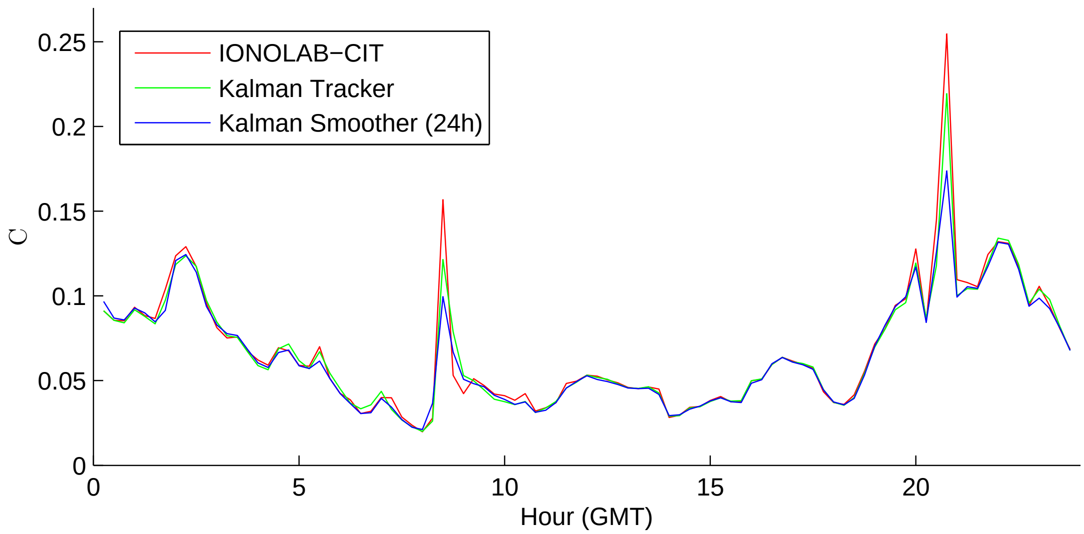

Figure 5.38: Cost function obtained for independent runs of IONOLAB-CIT, and cost function obtained after application of Kalman tracking and Kalman smoothing methods on 1 September 2011, when 3 GPS receiver stations are used in reconstructions.

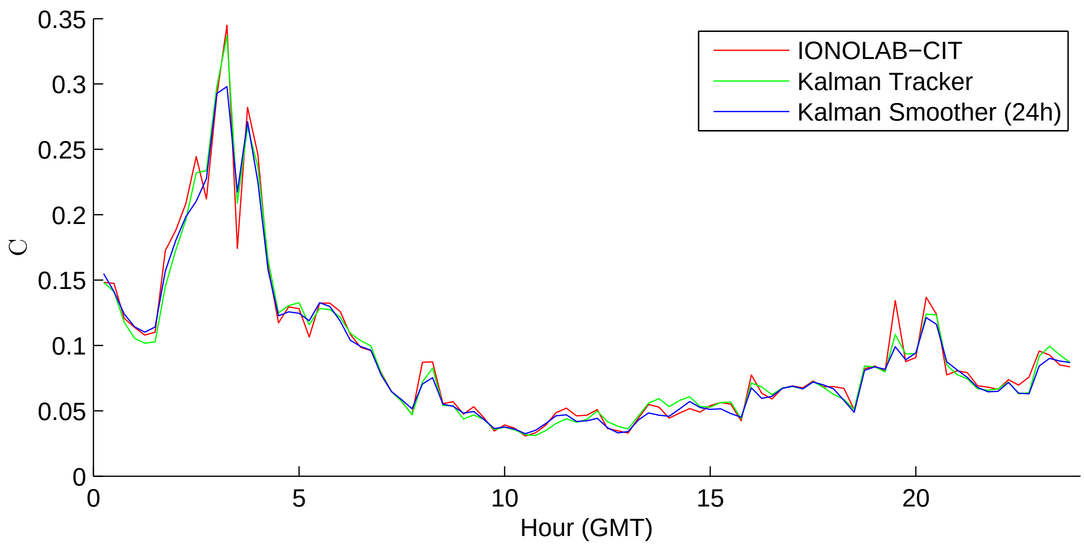

Figure 5.39: Cost function obtained for independent runs of IONOLAB-CIT, and cost function obtained after application of Kalman tracking and Kalman smoothing methods on 10 March 2011, when 3 GPS receiver stations are used in reconstructions.

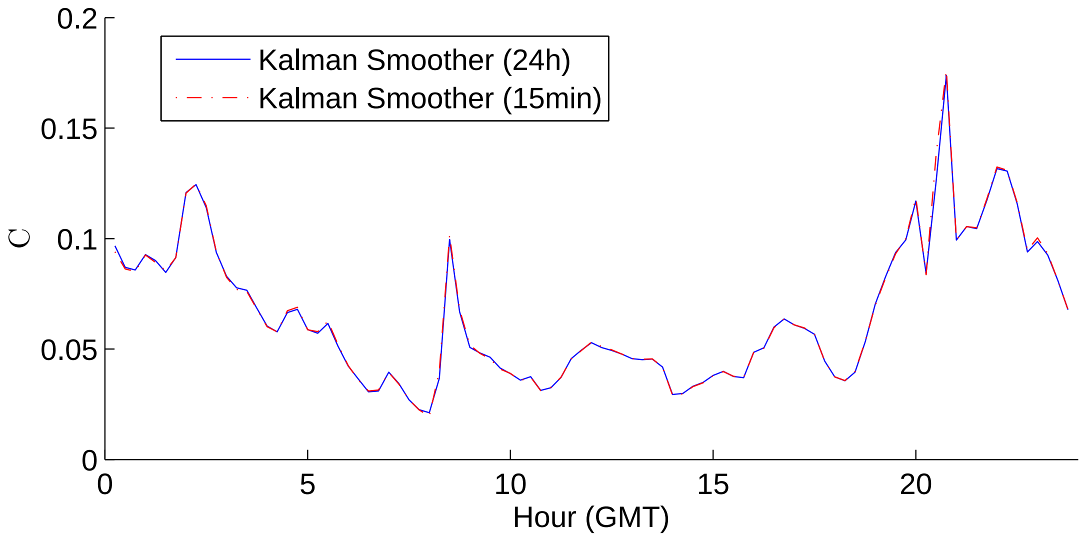

Figure 5.40: Kalman smoothing results on 1 September 2011, when 3 GPS receiver stations are used in reconstructions, by using all results obtained by the IONOLAB-CIT technique up to 15 minutes into the future, and by using all results obtained by the IONOLAB-CIT technique within 24 hours.

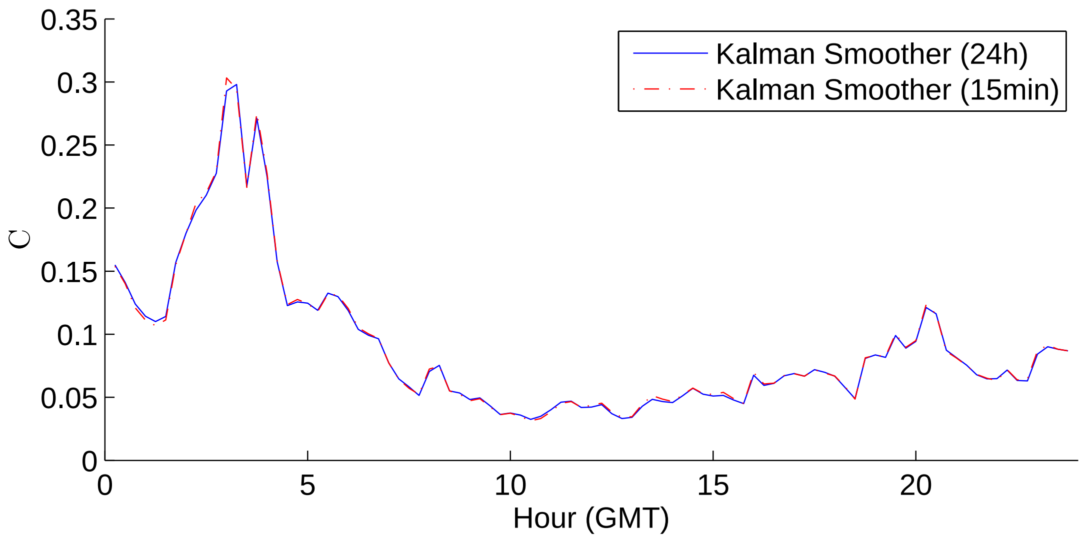

Figure 5.41: Kalman smoothing results on 10 March 2011, when 3 GPS receiver stations are used in reconstructions, by using all results obtained by the IONOLAB-CIT technique up to 15 minutes into the future, and by using all results obtained by the IONOLAB-CIT technique within 24 hours.

Table 5.2: Computational cost advantage of using Kalman prediction step for the next initial point in the IONOLAB-CIT technique.

Date	C_I	C_T	K_D	K_C	Computation Decrement
1 September 2011	0.205	0.064	28.18	5.20	%18.5
10 March 2011	0.262	0.063	27.96	5.69	%20.4
28 May 2011	0.150	0.066	29.71	4.88	%16.4
12 June 2011	0.213	0.059	28.57	5.72	%20.0

5.8 Computational Cost Analysis

When using the IONOLAB-CIT technique, the state transition equation can be used for estimating the initial search point in the problem space of the next time instant. This process not only decreases the computational cost of the IONOLAB-CIT technique, but also starts the optimization search in a closer neighbourhood of the solution and decreases the probability of converging to the local minima in the problem space. In order to present a metric about the computational cost advantage of this method, average value of the initial cost functions obtained by using the default IRI-Plas parameters C_I, and the average value of the cost functions for predicted perturbation surface parameters C_T are given in Table 5.2. The average decrement in the computational cost is calculated by dividing the average number of iterations for decreasing the cost function from C_I to C_T, which will be denoted with K_D, by the average number of iterations for convergence when using the default IRI-Plas parameters, which will be denoted as K_C. Results indicate an average decrease between %16 and %20 in the computational cost. Note that, these results are obtained for very strict stopping criteria for the BFGS method (solution candidate point in 6D space has moved less than 10^{-3} and the cost function has changed less than 10^{-4} in the last 3 iterations). If the stopping criteria is relaxed, the computational cost advantage of using the predicted perturbation surface parameters in terms of percentage will increase significantly.

5.9 Conclusion

The CIT results obtained by the IONOLAB-CIT technique are investigated in time for a set of calm and stormy days of ionosphere. It is observed that there is a high temporal correlation in the optimized parametric perturbation surfaces defined over the f_0F_2 and h_mF_2 surfaces. A linear state transition model is constructed which uses the perturbation surface parameters as the state of the system. Three state transition matrices are evaluated with increasingly longer time intervals on the obtained results. It is observed that the state transition matrix which assumes the perturbation surface parameters stay constant with respect to geodetic coordinates provides reliable predictions up to 1 hour time intervals with respect to the IRI-Plas model. Since the predictions produce better estimates with respect to default IRI-Plas parameters for small time intervals, computational cost advantage of using the predictions in the IONOLAB-CIT technique is also investigated. Initiating the optimization search in the problem space from the predicted values of perturbation surface parameters decrease the computational cost by 16% - 20%. Using the results obtained from these studies, a Kalman tracking approach, and a Kalman smoothing approach based on Rauch-Tung-Striebel smoother are implemented onto the IONOLAB-CIT results, in order to increase the robustness of the proposed IONOLAB-CIT technique. Result showed that using Kalman tracking/smoothing methods increase the robustness of the results obtained by the IONOLAB-CIT technique, especially when few number of GPS receiver stations are used in reconstructions.

Chapter 6

Conclusions

In this thesis, a novel computerized ionospheric tomography technique, namely the IONOLAB-CIT, is proposed for obtaining robust 3D model of the ionosphere by using the IRI-Plas model and a set of GPS measurements geographically distributed over the region of reconstruction. Experiments done on the simulated data validated that the proposed technique achieves this objective. The IONOLAB-CIT is experimented over Turkey, by using the real GPS receiver data obtained from TNPGN-Active stations. Results showed significant improvement in the compliance between the measurements and the obtained 3D model of the ionosphere. The STEC measurements obtained from a set of left out GPS receiver stations are also predicted successfully by using the IONOLAB-CIT reconstructions. The CIT reconstructions obtained by the IONOLAB-CIT are also compared with the real ionosonde measurements. It has been shown that the IONOLAB-CIT produces significantly improved results in terms of compliance with the ionosonde measurements, with respect to IRI-Plas model, as well.

The proposed IONOLAB-CIT technique require accurate calculation of the synthetic STEC values from the IRI-Plas model. For this purpose, a method for highly accurate synthetic STEC calculation from the IRI-Plas model, namely the IRI-Plas-STEC, is introduced in this thesis. A publicly available space weather service based on IRI-Plas-STEC is implemented at the `www.ionolab.org` website.

The proposed IONOLAB-CIT technique produces 3D model of the ionosphere within a coherence interval of the ionosphere. However, obtained reconstruction results show high temporal correlation, which indicates that an extension in time domain for the IONOLAB-CIT technique is possible. This led to the implementation of Kalman based methods for tracking the parameters of the reconstructions in time domain. For this purpose, Kalman tracking method is implemented, which can be used for both obtaining more reliable results online, and decreasing the computational cost of the associated optimization. Also, a Kalman smoothing method, based on the Rauch-Tung-Striebel smoother, is implemented for obtaining further improvement on the reconstructions offline.

The IONOLAB-CIT does not strictly depend on the IRI-Plas model itself, or the ionospheric parameters to be optimized. It can be modified to use any other ionosphere model with different optimization parameters and perturbation surface models. GPS occultation measurements can be added to the measurement set like any other GPS-STEC measurements without any special effort. Moreover, any other type of measurement can be added to proposed CIT technique by modifying the cost function to be optimized and determining a penalty term for each type of measurement. Depending on the measurements, ionosphere model, selected disturbance surface models etc, problem space may include local minima or stationary points. In this thesis, three different optimization methods, namely gradient descent, BFGS and PSO, are experimented on both simulated and real data. Although BFGS method is preferred in this thesis for its greater performance, some problems may require optimization methods which are more robust against local minima. In these cases, PSO is a nice option which achieved good optimization results like BFGS in many cases. Gradient descent method, on the other hand, may be preferred for its simplicity.

The number of GPS receiver stations on the performance of the IONOLAB-CIT method is also investigated. It has been shown that 7 GPS receiver stations are sufficient for obtaining satisfactory results by using the IONOLAB-CIT technique, over a mid latitude region as large as Turkey, on both calm and stormy days of the ionosphere. Lower number of GPS receiver stations may decrease the performance of the technique significantly, especially when the ionosphere is disturbed by the solar storms. In these cases, using Kalman tracking and Kalman smoothing methods help to reduce the cost obtained by the IONOLAB-CIT technique.

The computational cost of the IONOLAB-CIT is not lightweight. However, since the computations within an iteration of the IONOLAB-CIT can be processed in parallel, it is possible to obtain near real-time results with a decent computer system. As indicated in the thesis, utilizing the temporal correlation property of the IONOLAB-CIT results may further help in decreasing the computational cost of the IONOLAB-CIT technique.

The IONOLAB-CIT is a unique technique which utilizes GPS-STEC measurements directly for the reconstruction of 3D electron density distribution compliant with the physical properties of the ionosphere obtained from the IRI-Plas model. 3D reconstruction of the electron density distribution enables accurate calculations in the ionosphere and has tremendous advantages over 2D reconstructions available in the literature. Time domain extension of the IONOLAB-CIT technique enables further improved results in the reconstructions.

Bibliography

[1] J. R. Austen, S. J. Franke, and C. H. Liu, "Ionospheric imaging using computerized tomography," *Radio Science*, vol. 23, no. 3, pp. 299–307, 1988.

[2] T. D. Raymund, J. R. Austen, S. J. Franke, C. H. Liu, J. A. Klobuchar, and J. Stalker, "Application of computerized-tomography to the investigation of ionospheric structures," *Radio Science*, vol. 25, no. 5, pp. 771–789, 1990.

[3] S. Pryse and L. Kersley, "A preliminary experimental test of ionospheric tomography," *Journal of Atmospheric and Terrestrial Physics*, vol. 54, no. 7-8, pp. 1007–1012, 1992.

[4] C. Mitchell, L. Kersley, J. A. T. Heaton, and S. E. Pryse, "Determination of the vertical electron density profile in ionospheric tomography: Experimental results," *Annales Geophysicae*, vol. 15, no. 6, pp. 747–752, 1997.

[5] O. Arikan, F. Arikan, and C. B. Erol, "3-D computerized ionospheric tomography with random field priors," in *Mathematical Methods in Engineering* (K. Taş, J. Tenreiro Machado, and D. Baleanu, eds.), pp. 325–334, Springer Netherlands, 2007.

[6] G. A. Hajj, R. Ibaez-Meier, E. R. Kursinski, and L. J. Romans, "Imaging the ionosphere with the global positioning system," *International Journal of Imaging Systems and Technology*, vol. 5, no. 2, pp. 174–187, 1994.

[7] S. V. Fridman, L. J. Nickisch, M. Aiello, and M. Hausman, "Real-time reconstruction of the three-dimensional ionosphere using data from a network of GPS receivers," *Radio Science*, vol. 41, no. 5, 2006. RS5S12.

[8] Y. Yao, J. Tang, P. Chen, S. Zhang, and J. Chen, "An improved iterative algorithm for 3-D ionospheric tomography reconstruction," *IEEE Transcations on Geoscience and Remote Sensing*, vol. 52, no. 8, pp. 4696–4706, 2014.

[9] O. Arikan, F. Arikan, and C. B. Erol, "Computerized ionospheric tomography with the IRI model," *Advances in Space Research*, vol. 39, no. 5, pp. 859–866, 2007.

[10] O. Erturk, O. Arikan, and F. Arikan, "Tomographic reconstruction of the ionospheric electron density as a function of space and time," *Advances in Space Research*, vol. 43, no. 11, pp. 1702–1710, 2009.

[11] J. K. Lee, F. Kamalabadi, and J. J. Makela, "Three-dimensional tomography of ionospheric variability using a dense GPS receiver array," *Radio Science*, vol. 43, no. 3, 2008.

[12] D. Wen, Y. Yuan, J. Ou, K. Zhang, and K. Liu, "A hybrid reconstruction algorithm for three dimensional ionospheric tomography," *IEEE Transcations on Geoscience and Remote Sensing*, vol. 46, no. 6, pp. 1733–1739, 2008.

[13] X. F. Ma, T. Maruyama, G. Ma, and T. Takeda, "Three-dimensional ionospheric tomography using observation data of GPS ground receivers and ionosonde by neural network," *Journal of Geophysical Research: Space Physics*, vol. 110, no. A5, 2005. A05308.

[14] V. E. Kunitsyn and E. D. Tereshchenko, *Ionospheric Tomography*. Berlin Heidelberg: Springer-Verlag, 2003.

[15] G. S. Bust and C. N. Mitchell, "History, current state, and future directions of ionospheric imaging," *Reviews of Geophysics*, vol. 46, no. 1, 2008. RG1003.

[16] H. Tuna, O. Arikan, F. Arikan, T. L. Gulyaeva, and U. Sezen, "Online user-friendly slant total electron content computation from IRI-Plas: IRI-Plas-STEC," *Space Weather*, vol. 12, no. 1, pp. 64–75, 2014.

[17] F. Arikan, S. Shukurov, H. Tuna, O. Arikan, and T. Gulyaeva, “Performance of GPS slant total electron content and IRI-Plas-STEC for days with ionospheric disturbance,” *Geodesy and Geodynamics*, vol. 7, no. 1, pp. 1 – 10, 2016. Special Issue: GNSS Applications in Geodesy and Geodynamics.

[18] H. Tuna, O. Arikan, and F. Arikan, “Regional model-based computerized ionospheric tomography using GPS measurements: IONOLAB-CIT,” *Radio Science*, vol. 50, no. 10, pp. 1062–1075, 2015. 2015RS005744.

[19] K. Davies, *Ionospheric Radio*. Electromagnetics and Radar Series, Peregrinus, 1990.

[20] K. Rawer, *Wave Propagation in the Ionosphere*. Developments in Electromagnetic Theory and Applications, Springer Netherlands, 1993.

[21] M. Kelley, *The Earth's Ionosphere: Plasma Physics & Electrodynamics*. International Geophysics, Elsevier Science, 2009.

[22] C. M. Ho, B. D. Wilson, A. J. Mannucci, U. J. Lindqwister, and D. N. Yuan, “A comparative study of ionospheric total electron content measurements using global ionospheric maps of GPS, TOPEX radar, and the Bents model,” *Radio Science*, vol. 32, no. 4, pp. 1499–1512, 1997.

[23] L. Kersley, D. Malan, S. E. Pryse, L. R. Cander, R. A. Bamford, A. Belehaki, R. Leitinger, S. M. Radicella, C. N. Mitchell, and P. S. J. Spencer, “Total electron content - A key parameter in propagation: measurement and use in ionospheric imaging,” *Annals of Geophysics*, vol. 47, no. 2-3, pp. 1067–1091, 2004.

[24] T. Garner, T. G. II, B. Tolman, R. Harris, R. Calfas, and H. Gallagher, “Total electron content measurements in ionospheric physics,” *Advances in Space Research*, vol. 42, no. 4, pp. 720–726, 2008.

[25] B. Hofmann-Wellenhof, H. Lichtenegger, and J. Collins, *Global Positioning System: Theory and Practice*. Springer Vienna, 2013.

[26] J. A. Klobuchar, “Effects of the equatorial ionosphere on GPS,” *GPS World*, vol. 2, no. 4, pp. 48–51, 1991.

[27] L. Wanninger, “Effects of the equatorial ionosphere on GPS,” *GPS World*, vol. 4, no. 7, pp. 48–53, 1993.

[28] N. Crocetto, F. Pingue, S. Ponte, G. Pugliano, and V. Sepe, “Ionospheric error analysis in GPS measurements,” *Annals of Geophysics*, vol. 51, no. 4, 2008.

[29] A. J. Coster, E. M. Gaposchkin, and L. E. Thornton, “Real-time ionospheric monitoring system using GPS,” *Navigation*, vol. 39, no. 2, pp. 191–204, 1992.

[30] A. Leick, *GPS Satellite Surveying*. New Jersey: John Wiley and Sons Inc., 2004.

[31] A. Komjathy, *Global Ionospheric Total Electron Content Mapping Using the Global Positioning System*. PhD thesis, Department of Geodesy and Geomatics Engineering Technical Report No.188, University of New Brunswick, Fredericton, New Brunswick, Canada, 1997.

[32] S. Schaer, *Mapping and predicting the Earths ionosphere using the global positioning system*. PhD thesis, University of Bern, Bern, Switzerland, 1999.

[33] K. Davies and G. K. Hartmann, “Studying the ionosphere with the Global Positioning System,” *Radio Science*, vol. 32, no. 4, pp. 1695–1703, 1997.

[34] F. Arikan, C. B. Erol, and O. Arikan, “Regularized estimation of vertical total electron content from Global Positioning System data,” *Journal of Geophysical Research: Space Physics*, vol. 108, no. A12, 2003. 1469.

[35] P. Sibanda, *Challenges in Topside Ionospheric Modelling over South Africa*. PhD thesis, Rhodes University, South Africa, 2010.

[36] S. Jin and R. Jin, “GPS ionospheric mapping and tomography: A case of study in a geomagnetic storm,” in *Geoscience and Remote Sensing Symposium (IGARSS), 2011 IEEE International*, pp. 1127–1130, July 2011.

[37] S. Hirooka, K. Hattori, M. Nishihashi, S. Kon, and T. Takeda, “Development of ionospheric tomography using neural network and its application to the 2007 Southern Sumatra earthquake,” *Electrical Engineering in Japan*, vol. 181, no. 4, pp. 9–18, 2012.

[38] F. Arikan, H. Nayir, U. Sezen, and O. Arikan, "Estimation of single station interfrequency receiver bias using GPS-TEC," *Radio Science*, vol. 43, no. 4, 2008. RS4004.

[39] H. Nayir, F. Arikan, O. Arikan, and C. B. Erol, "Total electron content estimation with Reg-Est," *Journal of Geophysical Research: Space Physics*, vol. 112, no. A11, 2007. A11313.

[40] "IONOLAB."
$http://www.ionolab.org$.

[41] U. Sezen, F. Arikan, O. Arikan, O. Ugurlu, and A. Sadeghimorad, "Online, automatic, near-real time estimation of GPS-TEC: IONOLAB-TEC," *Space Weather*, vol. 11, no. 5, pp. 297–305, 2013. RS6018.

[42] D. Bilitza, D. Altadill, Y. Zhang, C. Mertens, V. Truhlik, P. Richards, L.-A. McKinnell, and B. Reinisch, "The International Reference Ionosphere 2012 - a model of international collaboration," *J. Space Weather Space Clim.*, vol. 4, p. A07, 2014.

[43] T. L. Gulyaeva and D. Bilitza, "Towards ISO standard Earth Ionosphere and Plasmasphere model," in *New Developments in the Standard Model* (R. J. Larsen, ed.), pp. 1–48, NOVA Science Publishers, Inc, Hauppauge, New York, 2012.

[44] T. Gulyaeva, F. Arikan, and I. Stanislawska, "Inter-hemispheric imaging of the ionosphere with the upgraded IRI-Plas model during the space weather storms," *Earth, Planets and Space*, vol. 63, no. 8, pp. 929–939, 2011.

[45] T. Gulyaeva, "Storm time behavior of topside scale height inferred from the ionosphere-plasmasphere model driven by the F2 layer peak and GPS-TEC observations," *Advances in Space Research*, vol. 47, no. 6, pp. 913–920, 2011.

[46] O. A. Maltseva, G. A. Zhbankov, and N. S. Mozhaeva, "Advantages of the new model of IRI (IRI-Plas) to simulate the ionospheric electron density: case of the European area," *Advances in Radio Science*, vol. 11, pp. 307–311, July 2013.

[47] T. Gulyaeva, F. Arikan, M. Hernandez-Pajares, and I. Stanislawska, "GIM-TEC adaptive ionospheric weather assessment and forecast system," *Journal of Atmospheric and Solar-Terrestrial Physics*, vol. 102, pp. 329–340, 2013.

[48] G. E. Lanyi and T. Roth, "A comparison of mapped and measured total ionospheric electron content using global positioning system and beacon satellite observations," *Radio Science*, vol. 23, no. 4, pp. 483–492, 1988.

[49] A. J. Mannucci, B. D. Wilson, D. N. Yuan, C. H. Ho, U. J. Lindqwister, and T. F. Runge, "A global mapping technique for GPS-derived ionospheric total electron content measurements," *Radio Science*, vol. 33, no. 3, pp. 565–582, 1998.

[50] S. C. Mushini, P. Jayachandran, R. Langley, and J. MacDougall, "Use of varying shell heights derived from ionosonde data in calculating vertical total electron content (TEC) using GPS new method," *Advances in Space Research*, vol. 44, no. 11, pp. 1309–1313, 2009.

[51] M. A. Cabrera, R. Ezquer, and S. Radicella, "Predicted and measured slant ionospheric electron content," *Journal of Atmospheric and Solar-Terrestrial Physics*, vol. 67, no. 16, pp. 1566–1572, 2005.

[52] B. Nava, P. Coïsson, and S. Radicella, "A new version of the NeQuick ionosphere electron density model," *Journal of Atmospheric and Solar-Terrestrial Physics*, vol. 70, no. 15, pp. 1856–1862, 2008.

[53] S. Radicella, "The NeQuick model genesis, uses and evolution," *Annals of Geophysics*, vol. 52, no. 3-4, 2009.

[54] P. Coïsson, S. Radicella, R. Leitinger, and B. Nava, "Topside electron density in IRI and NeQuick: Features and limitations," *Advances in Space Research*, vol. 37, no. 5, pp. 937–942, 2006.

[55] "International GNSS Service (IGS)."
http://igscb.jpl.nasa.gov/.

[56] "EUREF Permanent Network."
http://www.epncb.oma.be/_networkdata/stationmaps.php.

[57] F. Arikan, U. Sezen, T. Gulyaeva, and O. Cilibas, "Online, automatic, ionospheric maps: IRI-PLAS-MAP," *Advances in Space Research*, vol. 55, no. 8, pp. 2106–2113, 2015.

[58] S. Shukurov, T. Gulyaeva, F. Arikan, M. Necat Deviren, H. Tuna, and O. Arikan, "Comparison of IRI-Plas and IONOLAB Slant Total Electron Content for Disturbed Days of Ionosphere," in *40th COSPAR Scientific Assembly*, vol. 40 of *COSPAR Meeting*, p. 3059, 2014.

[59] E. J. Fremouw, J. A. Secan, and B. M. Howe, "Application of stochastic inverse theory to ionospheric tomography," *Radio Science*, vol. 27, no. 5, pp. 721–732, 1992.

[60] M. Materassi and C. Mitchell, "A simulation study into constructing of the sample space for ionospheric imaging," *Journal of Atmospheric and Solar-Terrestrial Physics*, vol. 67, no. 12, pp. 1085–1091, 2005.

[61] B. M. Howe, K. Runciman, and J. A. Secan, "Tomography of the ionosphere: Four-dimensional simulations," *Radio Science*, vol. 33, no. 1, pp. 109–128, 1998.

[62] C. G. Broyden, "The convergence of a class of double-rank minimization algorithms 1. general considerations," *IMA Journal of Applied Mathematics*, vol. 6, no. 1, pp. 76–90, 1970.

[63] R. Fletcher, "A new approach to variable metric algorithms," *The Computer Journal*, vol. 13, no. 3, pp. 317–322, 1970.

[64] D. Goldfarb, "A family of variable-metric methods derived by variational means," *Mathematics of Computation*, vol. 24, no. 109, pp. 23–26, 1970.

[65] D. F. Shanno, "Conditioning of quasi-newton methods for function minimization," *Mathematics of Computation*, vol. 24, no. 111, pp. 647–656, 1970.

[66] J. Kennedy and R. Eberhart, "Particle swarm optimization," *Proceedings of IEEE International Conference on Neural Networks*, pp. 1942–1948, 1995.

[67] H. Tuna, O. Arikan, F. Arikan, and T. Gulyaeva, "Estimation of 3D electron density in the ionosphere by using fusion of GPS satellite-receiver network measurements and IRI-Plas model," in *Proceedings of the 16th International Conference on Information Fusion FUSION 2013, Istanbul, Turkey, July 9-12, 2013*, pp. 1650–1657, 2013.

[68] H. Tuna, O. Arikan, and F. Arikan, "3D electron density estimation in the ionosphere," in *2014 22nd Signal Processing and Communications Applications Conference (SIU), Trabzon, Turkey, April 23-25, 2014*, pp. 529–532, 2014.

[69] Y. E. Gokdag, F. Arikan, C. Toker, and O. Arikan, "Parameter estimation for synthetic TEC surfaces by using Particle Swarm Optimization," in *2012 20th Signal Processing and Communications Applications Conference (SIU)*, pp. 1–4, April 2012.

[70] M. N. Deviren, F. Arikan, and O. Arikan, "Investigation of ionospheric trend over Turkey using Sliding Window Statistical Analysis method," in *2013 21st Signal Processing and Communications Applications Conference (SIU)*, pp. 1–4, April 2013.

[71] A. V. Mikhailov and D. Marin, "An interpretation of the foF2 and hmF2 long-term trends in the framework of the geomagnetic control concept," *Annales Geophysicae*, vol. 19, no. 57, pp. 733–748, 2001.

[72] S. S. Kouris, T. D. Xenos, K. V. Polimeris, and D. Stergiou, "TEC and foF2 variations: preliminary results," *Annals of Geophysics*, vol. 47, no. 4, pp. 1325–1332, 2004.

[73] U. Sezen, O. Sahin, F. Arikan, and O. Arikan, "Estimation of hmF2 and foF2 Communication Parameters of Ionosphere F2 -Layer Using GPS Data and IRI-Plas Model," *Antennas and Propagation, IEEE Transactions on*, vol. 61, no. 10, pp. 5264–5273, 2013.

[74] L. Armijo, "Minimization of functions having Lipschitz continuous first partial derivatives.," *Pacific J. Math.*, vol. 16, no. 1, pp. 1–3, 1966.

[75] X. Huang and B. Reinisch, "Vertical electron density profiles from the Digisonde network," *Advances in Space Research*, vol. 18, no. 6, pp. 121–129, 1996.

[76] J. E. Titheridge, *Ionogram Analysis with the Generalised Program POLAN*. Report UAG-93, World Data Center A for Solar-Terrestrial Physics, 1985.

[77] I. Sayin, F. Arikan, and K. E. Akdogan, "Optimum temporal update periods for regional ionosphere monitoring," *Radio Science*, vol. 45, no. 6, 2010. RS6018.

[78] A. Rius, G. Ruffini, and L. Cucurull, "Improving the vertical resolution of ionospheric tomography with GPS occultations," *Geophysical Research Letters*, vol. 24, no. 18, pp. 2291–2294, 1997.

[79] L. Scherliess, R. W. Schunk, J. J. Sojka, and D. C. Thompson, "Development of a physics-based reduced state Kalman filter for the ionosphere," *Radio Science*, vol. 39, no. 1, 2004. RS1S04.

[80] C. Wang, G. Hajj, X. Pi, I. G. Rosen, and B. Wilson, "Development of the Global Assimilative Ionospheric Model," *Radio Science*, vol. 39, no. 1, 2004. RS1S06.

[81] G. S. Bust, T. W. Garner, and T. L. Gaussiran, "Ionospheric data assimilation three-dimensional (IDA3D): A global, multisensor, electron density specification algorithm," *Journal of Geophysical Research: Space Physics*, vol. 109, no. A11, 2004. A11312.

[82] C. N. Mitchell and P. S. J. Spencer, "A three-dimensional time-dependent algorithm for ionospheric imaging using GPS," *Annals of Geophysics*, vol. 46, no. 4, pp. 687–696, 2003.

[83] J. M. Juan, A. Rius, M. Hernandez-Pajares, and J. Sanz, "A two-layer model of the ionosphere using global positioning system data," *Geophysical Research Letters*, vol. 24, no. 4, pp. 393–396, 1997.

[84] R. E. Kalman, "A new approach to linear filtering and prediction problems," *Journal of Basic Engineering*, no. 82 (Series D), pp. 35–45, 1960.

[85] H. E. Rauch, C. T. Striebel, and F. Tung, "Maximum likelihood estimates of linear dynamic systems," *AIAA Journal*, vol. 3, no. 8, pp. 1445–1450, 1965.

Appendix A

Storm Indices

Table A.1: Planetary Wp Indices obtained from `http://www.izmiran.ru/ionosphere/weather/storm/` for the days used in the experiments.

	UT																								
Date	0	1	2	3	4	5	6	7	8	9	10	11	12	13	14	15	16	17	18	19	20	21	22	23	Mean
2009.04.22	2.6	2.6	2.3	2.1	2.0	1.9	2.1	2.2	2.2	2.5	2.6	2.3	2.2	2.4	2.4	2.4	2.9	2.9	2.7	2.2	2.2	2.2	2.7	2.8	2.4
2010.03.12	2.4	2.5	2.5	2.7	2.7	2.3	2.3	2.0	2.1	2.2	2.7	2.7	3.1	4.2	4.3	3.8	3.8	3.3	3.3	3.0	2.9	2.9	3.0	3.0	2.9
2011.02.05	6.1	5.9	5.4	4.7	4.5	4.3	4.4	4.2	4.1	4.2	4.3	4.4	4.1	3.6	3.4	3.7	3.8	3.7	3.6	3.4	3.6	3.9	4.0	3.9	4.2
2011.03.10	2.2	2.1	2.1	2.3	2.4	2.4	2.3	2.2	2.4	2.8	3.7	4.2	3.8	3.6	2.9	2.5	2.7	2.6	2.2	2.2	2.5	3.3	4.0	3.7	2.8
2011.03.21	2.5	2.5	2.5	2.6	2.5	2.4	2.3	2.4	2.4	2.6	2.7	3.0	3.1	2.7	2.6	2.4	2.3	2.3	2.3	2.2	2.8	2.8	2.8	3.5	2.6
2011.05.28	2.9	3.0	3.3	3.4	3.8	3.8	3.8	3.7	4.2	4.9	5.4	5.7	5.8	5.7	5.4	5.3	4.9	4.6	4.4	4.2	4.2	3.6	3.2	3.4	4.3
2011.06.12	2.2	2.3	2.4	2.3	2.2	2.3	2.6	2.7	2.8	2.5	2.5	2.4	2.2	1.9	2.3	2.3	2.4	2.4	2.5	2.4	2.2	2.5	2.8	2.4	2.4
2011.08.06	6.8	6.4	5.6	5.1	5.0	5.2	5.4	5.5	5.3	4.7	4.4	4.2	4.0	3.6	3.4	3.8	3.9	4.1	4.4	4.3	4.4	4.3	4.3	4.2	4.7
2011.09.01	2.3	2.0	2.0	2.0	2.1	2.3	2.3	2.2	2.3	2.1	2.3	2.0	2.5	2.6	2.9	3.1	3.1	3.0	2.7	2.9	2.7	2.5	2.3	2.3	2.4
2011.09.21	2.6	2.7	2.5	2.5	2.4	2.7	2.4	2.3	2.4	2.1	2.0	2.1	2.4	2.5	2.7	2.6	2.2	2.2	2.4	2.2	2.0	2.0	2.1	2.1	2.3
2011.11.01	4.4	5.0	4.7	4.4	4.2	3.9	3.8	3.6	3.7	3.8	4.2	4.8	5.4	5.7	5.8	6.0	5.8	5.5	5.1	4.7	4.5	4.3	3.8	3.8	4.6
2011.12.25	2.2	2.3	2.2	2.0	2.0	2.2	2.5	1.9	1.9	2.0	1.9	2.0	2.2	2.1	2.1	2.3	2.2	2.3	2.5	2.3	2.2	2.3	2.4	2.4	2.2
2012.02.15	2.7	3.1	3.6	3.4	3.7	4.6	5.0	4.9	4.6	5.1	5.2	5.4	5.4	5.4	5.1	5.1	5.2	5.1	4.8	4.0	4.0	4.4	4.5	5.2	4.6
2012.04.13	3.4	3.6	3.8	3.9	4.1	4.6	4.8	4.9	5.1	4.8	4.5	4.3	4.1	4.0	3.6	3.5	3.7	4.1	4.2	3.7	3.5	3.1	3.2	3.1	4.0
2012.06.30	2.5	2.8	2.7	2.6	2.8	2.8	2.9	3.3	3.4	3.8	3.7	3.7	3.8	3.9	3.8	3.9	3.8	3.7	3.2	3.0	2.9	3.0	3.5	3.3	3.3
2012.08.15	2.7	2.6	2.7	2.4	2.6	2.8	3.1	3.0	2.4	2.5	2.5	2.5	2.6	2.6	2.7	3.0	2.9	2.8	2.7	2.7	2.7	2.5	2.8	2.9	2.7

Table A.2: Dst Indices obtained from `http://wdc.kugi.kyoto-u.ac.jp/dstdir/` for the days used in the experiments.

Date	UT																						
	1	2	3	4	5	6	7	8	9	10	11	12	13	14	15	16	17	18	19	20	21	22	23	24
2009.04.22	-2	-5	-5	-2	1	0	0	0	-2	-3	-1	-3	-7	-6	-4	-2	0	2	3	2	-1	-3	-5	-2
2010.03.12	-12	-13	-15	-12	-14	-18	-19	-15	-13	-11	-15	-17	-17	-15	-14	-14	-13	-14	-16	-19	-19	-17	-16	-17
2011.02.05	-50	-50	-47	-39	-46	-48	-52	-50	-54	-54	-49	-42	-37	-35	-34	-34	-33	-31	-28	-31	-31	-34	-36	-36
2011.03.10	-11	-11	-13	-15	-17	-20	-19	-25	-36	-36	-38	-35	-39	-42	-37	-33	-36	-38	-37	-41	-55	-62	-55	-50
2011.03.21	-10	-12	-13	-11	-7	-8	-8	-6	-5	-3	-4	-4	-3	-1	1	1	-2	-1	1	2	1	1	-6	-16
2011.05.28	-31	-32	-33	-31	-27	-25	-21	-32	-41	-47	-74	-80	-71	-75	-80	-77	-74	-69	-64	-59	-54	-45	-54	-56
2011.06.12	-20	-18	-16	-16	-16	-16	-15	-12	-15	-12	-12	-16	-15	-11	-10	-14	-13	-16	-16	-14	-10	-8	-7	-10
2011.08.06	-78	-90	-104	-115	-99	-84	-77	-75	-65	-60	-60	-66	-74	-71	-70	-71	-70	-65	-64	-60	-54	-56	-53	-47
2011.09.01	-1	-3	-4	-4	-6	-6	-7	-7	-6	-5	-4	-6	2	1	-1	-1	1	4	1	-2	-4	-5	-6	-7
2011.09.21	-18	-18	-16	-14	-9	-5	-6	-8	-8	-8	-5	-8	-13	-16	-19	-17	-13	-16	-16	-13	-11	-10	-11	-14
2011.11.01	-39	-44	-43	-44	-45	-46	-48	-45	-41	-37	-43	-47	-57	-62	-65	-66	-56	-50	-46	-45	-41	-43	-42	-46
2011.12.25	-1	0	-2	-5	-7	-5	-4	-4	-1	1	-1	0	1	1	3	4	3	3	2	-1	-2	-1	-2	-2
2012.02.15	-21	-24	-29	-37	-42	-46	-52	-46	-43	-49	-51	-54	-55	-52	-53	-53	-58	-57	-54	-51	-45	-43	-49	-46
2012.04.13	-36	-29	-28	-44	-49	-49	-43	-33	-28	-27	-27	-24	-23	-19	-16	-15	-14	-12	-11	-14	-15	-17	-19	-14
2012.06.30	34	28	25	14	18	17	9	3	7	4	-1	2	3	6	1	1	0	-10	-7	-15	-19	-15	-12	-13
2012.08.15	0	-1	1	2	0	-1	0	-2	-1	-5	-4	-4	0	-2	-1	1	-5	-4	0	3	0	-3	1	3

Table A.3: Kp and Ap Indices obtained from `http://wdc.kugi.kyoto-u.ac.jp/kp/` for the days used in the experiments.

Date	Kp									Ap								
	UT								Sum	UT								Avg
	3	6	9	12	15	18	21	24		3	6	9	12	15	18	21	24	
2009.04.22	2-	2-	0+	1+	1	0+	0+	1+	8	6	6	2	5	4	2	2	5	4
2010.03.12	3-	3+	2+	2-	2	2	2-	1+	17	12	18	9	6	7	7	6	5	9
2011.02.05	5	4-	3-	2+	1+	2+	3	3-	23	48	22	12	9	5	9	15	12	16
2011.03.10	2	2+	4+	4-	3-	2	4	5-	26-	7	9	32	22	12	7	27	39	19
2011.03.21	2+	1-	1	0+	0	1-	1	3	9	9	3	4	2	0	3	4	15	5
2011.05.28	5-	3-	6+	6	6+	2	1+	4	33+	39	12	94	80	94	7	5	27	45
2011.06.12	1	1	1+	3-	3-	2+	2-	1-	13+	4	4	5	12	12	9	6	3	7
2011.08.06	6+	5	4-	4	4-	3+	1+	3	30+	94	48	22	27	22	18	5	15	31
2011.09.01	1+	1	0	0+	0+	0+	0+	1-	4+	5	4	0	2	2	2	2	3	2
2011.09.21	0	0	1	1+	2	2-	0+	2	8+	0	0	4	5	7	6	2	7	4
2011.11.01	4-	2+	3	5-	4-	4	2+	3-	26+	22	9	15	39	22	27	9	12	19
2011.12.25	1+	2-	1	0+	0+	0	1-	0	5+	5	6	4	2	2	0	3	0	3
2012.02.15	2+	5+	4-	3+	3-	3	3+	4-	27+	9	56	22	18	12	15	18	22	22
2012.04.13	5-	5	4-	3	2-	3-	2	3-	25+	39	48	22	15	6	12	7	12	20
2012.06.30	2+	3	4-	4+	5-	4	4-	4+	30	9	15	22	32	39	27	22	32	25
2012.08.15	1+	0	1	1+	1+	1+	2-	2+	10+	5	0	4	5	5	5	6	9	5

Table A.4: AE Indices obtained from `http://wdc.kugi.kyoto-u.ac.jp/aedir/` for the days used in the experiments.

	UT																							
Date	0	1	2	3	4	5	6	7	8	9	10	11	12	13	14	15	16	17	18	19	20	21	22	23
2009.04.22	33	26	33	37	24	32	31	20	34	36	39	157	154	38	27	31	20	20	24	31	34	56	65	28
2010.03.12	177	233	79	50	138	314	201	77	100	202	182	195	282	397	185	288	109	52	117	135	199	183	129	158
2011.02.05	463	425	246	244	205	250	263	389	293	289	127	93	102	66	167	189	218	77	165	456	331	368	186	91
2011.03.10	169	158	216	201	231	230	252	472	645	931	586	373	322	359	384	185	311	547	520	1076	990	1052	570	380
2011.03.21	194	99	85	50	29	25	21	31	95	61	53	70	75	69	90	111	89	145	71	104	60	62	282	423
2011.05.28	651	662	697	432	215	296	459	707	1328	1097	770	1002	1112	919	377	222	138	85	88	63	39	119	409	391
2011.06.12	175	127	99	78	169	157	119	185	171	148	177	529	281	86	156	149	197	216	132	163	68	52	110	136
2011.08.06	399	876	1108	740	230	675	594	658	278	167	278	393	356	127	87	323	313	70	59	60	67	37	45	235
2011.09.01	38	29	32	40	110	119	57	33	43	47	54	52	47	44	47	60	67	43	39	30	28	34	67	49
2011.09.21	19	19	22	24	18	23	88	61	38	47	75	184	389	417	323	110	149	109	38	26	34	24	60	55
2011.11.01	358	415	270	242	176	230	217	593	441	501	655	978	815	785	679	661	643	423	222	100	95	158	179	369
2011.12.25	50	37	53	85	96	138	123	110	46	75	41	36	21	16	16	22	24	22	20	15	19	18	19	17
2012.02.15	250	281	410	790	791	579	386	561	525	575	526	631	583	485	704	679	732	702	684	545	251	701	782	460
2012.04.13	453	560	401	493	647	364	213	255	371	425	281	243	216	126	196	382	364	159	139	305	302	256	385	404
2012.06.30	258	347	368	307	128	494	828	681	617	618	746	535	454	426	679	467	234	145	260	553	689	744	699	406
2012.08.15	134	236	75	27	39	52	60	160	227	302	215	123	124	94	33	59	212	126	60	70	141	161	187	116

Appendix B

IGS and Data Exchange Formats for Experimental Data and Products

B.1 IGS

The International GNSS Service (IGS) is an organization of more than 200 worldwide agencies that provides GNSS receiver station data to generate precise GNSS products, in support of Earth science research, multidisciplinary applications, and education. IGS products include GNSS satellite ephemerides, Earth rotation parameters, receiver station coordinates and velocities, GNSS satellite and receiver station clock information, zenith tropospheric path delay estimates, and global ionosphere maps. These products support Earth science analyses and other efforts, such as monitoring the deformation of solid Earth and Earth rotation, investigation of the troposphere and the ionosphere, and determining orbits of scientific satellites. Currently, IGS supports the GPS and the GLONASS. Detailed information about the IGS can be found at `http://www.igs.org/`. The detailed information about the products that can be obtained from IGS network is given in `http://www.igs.org/products`. Figure B.1 shows the locations of

Figure B.1: Locations of the IGS Network Receiver Stations.

IGS network receiver stations.

B.1.1 IGS Ephemeris Data

IGS ephemeris data provides precise location information for GPS and GLONASS satellites (`http://www.igs.org/products`). This information can be downloaded from public ftp servers, like `ftp://garner.ucsd.edu/pub/products/`, `ftp://cddis.gsfc.nasa.gov/pub/gps/products/`, or `ftp://igscb.jpl.nasa.gov/pub/product/`. IGS ephemeris data is provided in ECEF coordinate system. Four types of GPS ephemeris are provided by IGS:

- Broadcast: Available in real-time, and provides daily satellite orbits with ~100 cm accuracy.
- UltraRapid: Released four times each day (at 03:00, 09:00, 15:00, and 21:00 GMT) and contains 48 hours worth of orbits; the first half is computed

from observations and the second half is the predicted orbit. It can provide satellite orbits with ~3 - 5 cm accuracy.

- Rapid: Available with approximately 17 - 41 hours latency, provides post-processed data with 15 minute sample interval. It can provide satellite orbits with ~2.5 cm accuracy.

- Final: Available with approximately 12 - 18 days latency, and provides the most accurate results with 15 minute sample interval. It can provide satellite orbits with ~2.5 cm accuracy.

Since the IGS ephemeris data provide locations of satellites with 15 minute sample interval, interpolation techniques are used for generating satellite positions with better resolution.

B.2 RINEX

Receiver INdependent EXchange Format (RINEX) is a data file format for exchanging raw measurement data obtained from GNSS receivers. Receiver stations use the measurements for obtaining precise location information in real-time, however, raw measurements and the intermediate calculations can be stored for later use which can provide interesting opportunities for a wide range of scientific and engineering applications. Users can process this data to obtain more accurate results, or use them to extract various types of information from the measurements other than the position information. There are three important GNSS observables obtained for each satellite in a RINEX file, which are pseudo-range, phase delay, and doppler data. By using the pseudo-range and phase delay information, TEC between the receiver and the satellite can be estimated. The latest RINEX format is version 3.03, which can be found at `http://igscb.jpl.nasa.gov/igscb/data/format/rinex303.pdf`.

B.3 IONEX

The IONosphere Map EXchange (IONEX) is a widely used standard format in ionospheric community for exchange of TEC maps. The IONEX file format supports the exchange of both 2D and 3D TEC maps given in a geographic grid. IONEX header contain differential (P1-P2) code biases (DCBs) for active GPS/GLONASS satellites. DCBs obtained from IONEX files are used by the IONOLAB-BIAS method in the computation of receiver inter-frequency bias, which is used by the IONOLAB-STEC method for providing more reliable STEC measurements. Detailed information about the IONEX format and sample files can be found at `https://igscb.jpl.nasa.gov/igscb/data/format/ionex1.pdf`.